A Qualification Methodology for Additively Manufactured Parts

University of Maryland, Baltimore County

João Carlos do Carmo Santos

Dissertação de Mestrado

Orientador na UMBC: Dr. Marc Zupan

Orientador na FEUP: Dr. Abel Dias dos Santos

U.PORTO
FEUP FACULDADE DE ENGENHARIA
UNIVERSIDADE DO PORTO

Mestrado Integrado em Engenharia Mecânica

Junho de 2016

Resumo

A tecnologia de Fabrico Aditivo tem o potencial de revolucionar a forma como as empresas produzem quase tudo. Este processo de fabrico inovador foi recentemente implementado pela Marinha dos Estados Unidos na forma de projetar, fabricar, armazenar e entregar componentes. O processo de sinterização direta por laser de metais (DMLS do inglês Direct Metal Laser Sintering) é um novo sistema capaz de produzir componentes de grande porte ou estruturas complexas próximas da forma final através da tecnologia de fabrico aditivo de forma totalmente automática, sem necessidade de ferramentas e diretamente baseado num modelo CAD. As ligas de titânio são particularmente utilizadas na produção de componentes em motores aeronáuticos, conjugando boas caraterísticas mecânicas específicas e uma excelente resistência à corrosão a altas temperaturas.

Neste trabalho de investigação foi apresentado um novo método para caracterizar peças produzidas por fabrico aditivo. Uma chapa com 1mm de espessura produzida por DMLS na liga de titânio Ti6Al4V (ou Ti64) foi submetida à técnica de teste com microprovetes, técnica esta capaz de fornecer informações que de outra forma seriam escondidas ou até mesmo impossíveis de obter à macro escala. Esta metodologia abrange a determinação da tensão limite de elasticidade, resistência à tração máxima, alongamento e módulo de Young, assim como a microestrutura e superfícies de fratura são também analisadas.

O comportamento mecânico local foi analisado em duas direções. Os resultados corroboram o cenário de uma terceira revolução industrial, sendo que foi observado um aumento na resistência em relação aos processos de fabrico tradicionais. Além disso, verificou-se que as propriedades dependiam da orientação dos provetes, o que comprovou a anisotropia característica de componentes produzidos por fabrico aditivo e, assim, atestou a capacidade da metodologia proposta de fornecer dados fiáveis para modelos globais de desempenho de componentes estruturais.

Abstract

Additive Manufacturing (AM) has the potential to revolutionize the way companies produce almost everything. As an exciting new technology, AM has recently come on the scene on how Navy designs, manufactures, stores, and delivers parts to the warfighter. Direct Metal Laser Sintering (DMLS) is an innovative system that explores the near-net shaping of large components and net shaping of small complex structures by means of AM - fully automatically, without tools and based directly on three-dimensional CAD design data. Titanium alloys provide high strength-to-weight ratio and good creep resistance at high temperatures, which makes them a natural fit to produce components in aero-engines.

This research discusses a new technique to qualify additively manufactured parts. A DMLS produced plate of 1 mm thick in Ti6Al4V (or Ti64) was subjected to microsample mechanical testing technique, which provides information that would otherwise be averaged or masked on the macroscale. It encompasses the determination of yield strength, ultimate tensile strength, elongation, and young's modulus. The microstructure and fracture surfaces were characterized as well.

The local mechanical behavior was described in two different directions. The results have corroborated the scenario of a third industrial revolution, where an increase in strength over traditionally manufactured components was observed. Additionally, the orientation-dependent properties proved anisotropic behavior for AM parts and thus attested the aptitude of microscale testing to provide verifiable property data as inputs to global part performance and failure models.

Acknowledgements

I would like to first thank Dr. Marc Zupan for giving me the opportunity to work under his advisement in the Micro Materials Characterization Lab and allowing me to work on par with his other graduate students. He has also played a very important part in helping me set up when I arrived to UMBC, along with my colleagues from the Global Engineering course. Without them I would not have enjoyed this experience as much as I did. This exchange would also not have been possible without the help of Dr. Abel Santos, to whom I am grateful for lending his assistance throughout the entire process.

I want to thank my two friends and lab mates Michael Duffy and Salahudin Nimer for their tuition, good conversations, and suggestions. It was a pleasure going through this entire process of thesis writing with them and I could not be more thankful to for their help. Without their know-how and advice I could not have finish this thesis workout. I would also like to thank my friends and colleagues from FEUP who accompanied me during these last five years in this pursue of the Master's degree in Mechanical Engineering, and it was a pleasure going through it with them.

This work was funded through the Office of Naval Research. This thesis was a collaborative effort with the Naval Air Station Patuxent River and I want to thank the organization for providing the material.

I would like to finally and most importantly thank my parents Joaquim Santos and Laura Carmo for their support and advice throughout my academic career. They taught me the most valuable lessons in life in that hard work and persistence lead to success.

Thank you all.

Table of Contents

List of Acronyms

3D – Three-Dimensional

3DP – Three-Dimensional Printing

AM – Additive Manufacturing

ASTM – American Society for Testing and Materials

bcc – body-centered cubic

CAD – Computer Aided Design

CNC – Computer Numeric Control

DED – Direct Energy Deposition

DIC – Digital Image Correlation

DMD – Direct Metal Deposition

DMLM – Direct Metal Laser Melting

DMLS – Direct Metal Laser Sintering

EBAM – Electron Beam Additive Manufacturing

EBM – Electron Beam Melting

EDS – Electron Dispersive Spectroscopy

FDM – Fused Metal Deposition

GA – Gas Atomization

hcp – hexagonal closed-packed

HC – Hexagonal Crystal

HCF – High Cycle Fatigue

HIP – Hot Isostatic Pressing

LMD/LENS – Laser Metal Deposition

LOM – Laminated Object Manufacturing

MJM – Material Jetting Modeling

OM – Optical Metallographic

PA – Plasma Atomization

PREP – Plasma Rotating Electrode Process

RA – Rotary Atomization

RX – Recrystallization

SEM – Scanning Electron Microscopy

SLA – Stereolithography

SLM – Selective Laser Melting

SLS – Selective Laser Sintering

S.O. – Specimen Orientation

ST – Solution Treat

STL – Standard Tessellation Language

UTS – Ultimate Tensile Strength

List of Figures

List of Tables

1 Introduction

1.1 Introduction

The present dissertation was developed and submitted to the Faculdade de Engenharia da Universidade do Porto (FEUP) in partial fulfillment of the requirements for the degree of Master of Science in Mechanical Engineering. The research project was developed in the University of Maryland Baltimore County (UMBC) in collaboration with the Naval Air Station Patuxent River (NAS Pax River). In this collaboration, UMBC conducted all micro-scale mechanical testing and NAS Pax River selected and procured all AM parts and performed all macro-scale mechanical testing. This collaboration links emerging AM efforts at NAS Pax River with the unique microtensile material characterization capabilities of UMBC.

1.2 Motivation

Additive manufacturing (AM) has the potential to revolutionize the way the Navy designs, manufactures, stores, and delivers parts to the warfighter. However, to realize this potential, each of these AM parts must demonstrate a set of minimum performance characteristics. These characteristics are generally assured by qualifying manufacturing processes and certifying said processes were followed by competent operators.

AM is a disruptive technology in that the Navy's normal qualifying methodologies do not appear to readily adapt or apply. Alternatively, many groups are developing sophisticated computer models to predict mechanical performance from synthetic microstructures calculated from various AM processing parameters. While this is an elegant approach, which would represent a triumph for basic materials research, the time and cost to develop the computational infrastructure is likely long and large, and these models will require some form of validation.

1.3 Aims and Scope

The aim of the present work is to understand the reliability of the results provided by an alternative approach to evaluate AM produced structural components on Ti6Al4V. The proposed methodology, outlined in Figure 1, uses local mechanical properties derived from UMBC MicroTensile testing. The micro-tensile measurements will include the effects of microstructure and the measured local mechanical properties will substitute the outputs of intermediate microstructural models, thus providing verifiable property data as inputs to global

part performance and failure models. This is a challenging objective because, although there is a lot of published data on the mechanical properties of additively manufactured metallic materials, especially on Ti6Al4V, there is no reported work performed in a microscale.

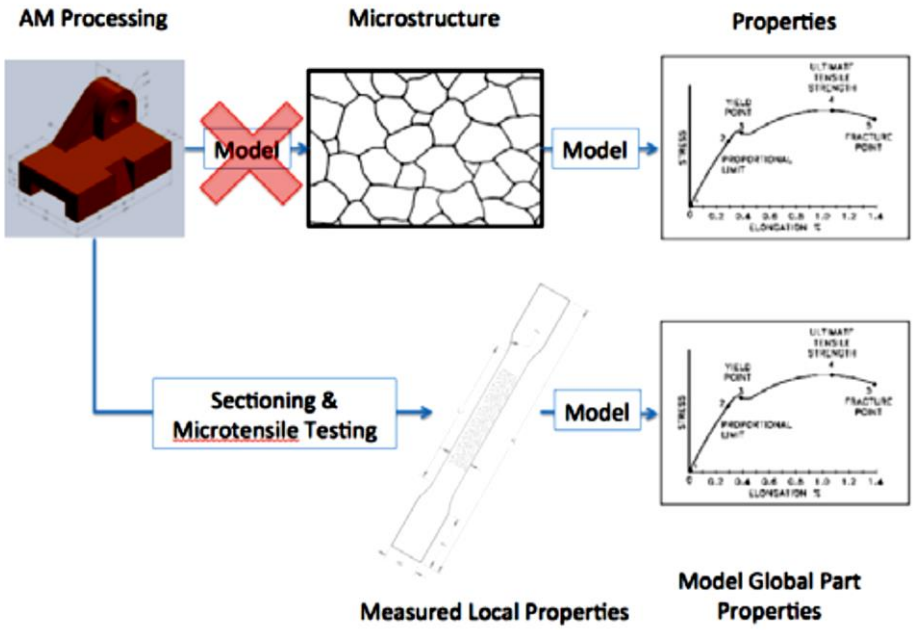

Figure 1 – Overall view of the proposed qualification methodology for additively manufactured parts.

The scope of this research drive is to report the material performance of additively manufactured Ti6Al4V. Microstructure and mechanical properties will be obtained using UMBC MicroTensile testing technique and a comparison with the macro-scale mechanical testing results performed by NAS Pax River and published values currently available will be made. This work represents the first step in the development of a new qualification methodology for additively manufactured parts which, in the future, will be used to generate a library of basis processes-microstructures-mechanical properties for future modelers to test and verify computational models.

1.4 Thesis Overview

Chapter 2 consists in a detailed review of relevant studies important to frame this work. In the review, a brief introduction to the Additive Manufacturing (AM) process will be made, including working principle, techniques, materials, and applications. Afterwards, a more detailed review on Metal Additive Manufacturing will be made, in which the different systems will be mentioned, along with material processing issues associated with them and post-processing operations. To better contextualize this work, the published data on Additive

Manufacturing of Ti6Al4V will be presented; it will also be made a brief introduction to Ti6Al4V talking about its main properties and microstructural features.

Chapter 3 discusses the methods used for the experimental procedures and scope. It describes the AM process parameters, mechanical testing microsample preparation, system and methods used for data analysis.

Chapter 4 describes the results obtained from microsample mechanical testing. The Young's modulus, yield strength, ultimate tensile strength, elongation to failure are presented. The local mechanical property measurements will be associated with the local microstructure, along with fractography analysis. The microsample mechanical testing results will be compared with the published data from literature.

Finally, chapter 5 discusses the conclusions that can be drawn and the future work to continue the research forward.

2 Literature review

2.1 Additive Manufacturing (AM)

2.1.1 Introduction

ASTM has defined Additive Manufacturing (AM) as the "process of joining materials to make objects from three-dimensional (3D) model data, usually layer by layer, as opposed to subtractive manufacturing methodologies" [1]. It is also called additive fabrication, additive processes, direct digital manufacturing, rapid prototyping, rapid manufacturing, layer manufacturing, solid freeform fabrication and 3D printing [2].

Originally called rapid prototyping, AM was developed has a cost-effective and time-efficient way to produce a prototype for design, form and fit inspection. However, due to the driving force from industry to seek for innovation in materials and processes, AM has changed from prototype production to rapid manufacturing. Since its inception in the mid-1980s, AM has evolved and blossomed into a whole range of processes (Table 1), bringing a paradigm shift from design for manufacturing to manufacturing for design [3].

As an alternative from traditional manufacturing processes such as machining, casting or forming. AM has many advantages; being a computer-automated process that fabricates physical 3D objects from computer-aided design (CAD) models, AM allows on-demand production of customized parts with no need of special tools. The ability of building a product layer-by-layer allows more complex geometries and heterogeneous compositions without any restraints, with material waste, time and cost of manufacturing greatly reduced for small parts and small batches [2-5].

2.1.2 Working Principle of Additive Manufacturing

The generalized steps of AM technologies are shown in Figure 2. The AM process starts with a 3D model of the object usually created by CAD software. This CAD file is then translated into a language (or file type) that AM machines can understand [6]. Standard Tessellation Language (STL) is the most commonly used, where the surfaces of the model are described with triangles [7]. Specialized software then slices the model into cross-sectional layers from the STL file, creating a computer file that is sent to the AM machine – the SLI file. The AM system then produces the part by forming each layer via the selective placement of material [8]. The part is then extracted from the machine and finishing operations are applied [4].

Figure 2 – Generalized AM process [9].

2.1.3 Additive Manufacturing Processes

Various AM processes have been introduced to the market by several industrial companies, including Electro Optical Systems (EOS) in Germany, MTT Technologies Group in England, Arcam in Sweden and Optomec, Stratasys, 3D Systems and Z Corp in the United States, among others [10].

The ASTM F42 committee classifies the AM processes into seven categories [1] – see Table 1. These processes vary in terms of the technique used to deposit layers and the way in which these layers are bonded together. Table 1 provides information about the process variations, materials used in each process and commercial manufacturers. For each technology, a single manufacturer may have different machines that differ from each other in terms of the process parameters, such as build envelope, manufacturing speed, layer thickness and cost [3]. There are other systems to classify AM process, e. g, into four broad categories based on the state of starting material: liquid, filament/paste, powder and solid sheet [2, 11]. Another way to categorize AM process may be based on the types of part materials, such as polymers, metals, ceramics, composites and biological materials [3].

Table 1 – AM processes and equipments manufacturers [3].

Process Category	Process/technology[(a)]	Material	Manufacturer(s)
Vat photopolymerization	SLA (Stereolithography)	UV curable resins	Asiga 3D Systems EnvisionTEC Rapidshape
		Waxes	DWS
		Ceramics	Lithoz
Material jetting	MJM (Multi-Jet Modeling)	UV curable resins	3D Systems Stratasys
		Waxes	Solidscape
Binder jetting	3DP (3D printing)	Composites Polymers, ceramics	3D Systems Voxeljet
		Metals	ExOne
Material Extrusion	FDM (Fused Deposition Modeling)	Thermoplastics	Stratasys MakerBot RepRap Bits from Bytes Fabbster Delta Micro Factory Corporation Beijing Tiertime
		Waxes	ChocEdge Essential Dynamics Fab@Home
Powder bed fusion	SLS (Selective Laser Sintering)	Thermoplastics	EOS Blueprinter 3D Systems
		Metals	3Geometry Matsuura 3D Systems
	SLM (Selective Laser Melting)	Metals	EOS SLM Solutions Concept Laser 3D Systems Realizer Renishaw
	EBM (Electron Beam Melting)	Metals	Arcam Sciaky
Sheet lamination	LOM (Laminated Object Manufacturing)	Paper Metals Thermoplastics	Mcor Technologies Fabrisonic Solido
Direct energy deposition	LMD/LENS (Laser Metal Deposition)	Metals	Optomec DM3D Irepa Laser
	EBAM (Electron Beam AM)	Metals	Sciaky

[(a)]Grouping shown in this column includes trademarked terms

2.1.4 Materials

In the early stages of its development, AM was only applied to produce plastic prototypes. After intense development and research, AM technology has enhanced its ability to produce near-net shaped parts with complex geometries and features that can be directly used as functional parts, including ceramics, composites and metals. Table 2 lists the type of materials processed by each AM process [2].

Table 2 – Materials and corresponding AM processes [2].

Material type		AM process(es)	Material(s)
Polymers[a]	Thermo-setting	SLA, MJM	Photo-curable polymers
	Thermo-plastic	MJM	Wax
		SLS	Polyamide 12, GF polyamide, polystyrene
		FDM	ABS, PC-ABS, PC, ULTEM
		3DP	Acrylic plastics, wax
Metals[a]		SLM	Stainless steel GP1, PH1 and 17-4; cobalt chrome MP1; titanium Ti6Al4V, Ti6Al4V ELI and TiCP; IN718; maraging steel MS1; AlSi20Mg
		LDM/LENS	Steel H13, 17-4 PH, PH 13-8 Mo, 304, 316 and 420; aluminum 4047; titanium TiCP, Ti-6-4, Ti-6-2-4-2 and Ti 6-2-4-6; IN625; Cu-Ni alloy; cobalt satellite 21
		EBM	Ti6Al4V, Ti6Al4V ELI, cobalt chrome
Ceramics[b]		SLA	Suspension of zirconia, silica, alumina, or other ceramic particles in liquid resin
		FDM	Alumina, PZT, Si_3N_4, zirconia, silica, bioceramic
		SLS	Alumina, silica, zirconia, ZrB_2, bioceramic, graphite, bioglass, and various sands
		3DP	Zirconia, silica, alumina, Ti3SiC2, bioceramic, and various sands
Composites[b]	Uniform composites	FDM	Polymer-metal, polymer-ceramic, short fiber-reinforced composites
		3DP	Polymer-matrix, metal-ceramic, ceramic-ceramic short fiber-reinforced composites
		LOM	Polymer-matrix, ceramic-matrix, fiber and particulate-reinforced composites
		SLS, SLM	Metal-metal, metal-ceramic, ceramic-ceramic, polymer-matrix, short fiber-reinforced composites
	FGM (Functionally graded materials)	LMD, LENS	CoCrMo/Ti6Al4V,TiC/Ti, Ti/TiO_2, Ti6Al4V/IN718
		FDM	PZT

Notes: [a] Commercially available materials for AM processes; [b] materials under research and development

2.1.5 Applications

Over the last 20 years, the research community has developed innovative, advanced AM techniques and applied them in aerospace, automotive, biomedical, energy, consumer goods, among others fields – see Figure 3 [12]. After intensive research and development in the areas of materials, processes, software and equipment, AM techniques have changed from prototype fabrication to rapid tooling and rapid manufacturing [13, 14].

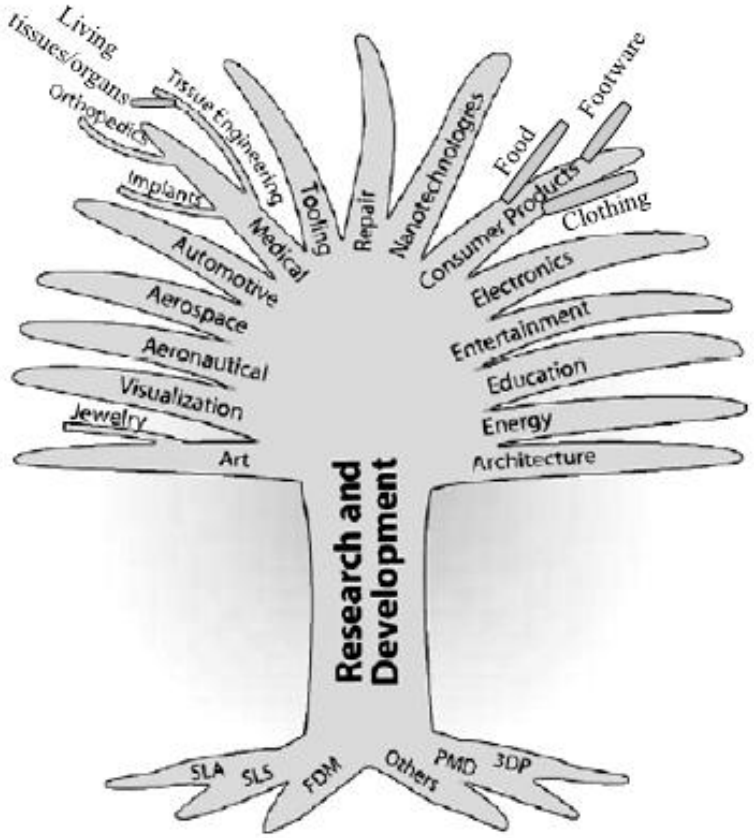

Figure 3 – Schematic visualization of AM field and research and development opportunities [12].

Compared to subtractive manufacturing, AM is particularly suitable for applications with low production volume, especially for parts with complex geometries and expensive materials [15]. AM processes also offer great potential for custom-designed components, such as hip or knee implants [16]. The following review AM applications in aerospace, automotive and biomedical industries.

2.1.5.1 Aerospace

Aerospace components frequently have complex geometries made of advanced materials, including titanium alloys, nickel superalloys, special steels or ultra-high temperature ceramics, which are difficult, costly, and time-consuming to produce using traditional processes. Moreover, aerospace production runs are often small, limited to a maximum of several thousand

parts. Therefore, AM technology is highly suitable for aerospace applications [2, 3, 12]. It can build parts with designs such as internal cavities and lattice structures that help reduce weight without compromising their mechanical performance. Current applications in the aerospace industry range from manufacturing simple objects such as armrests to complex parts like engine components (Figure 4(a)) [17]. In addition, AM technologies are also used for rapid tooling, such as mold and cores for casting (Figure 4(b)), or to repair aircraft engines in order to extend their lifetimes (Figure 4(c)) [2].

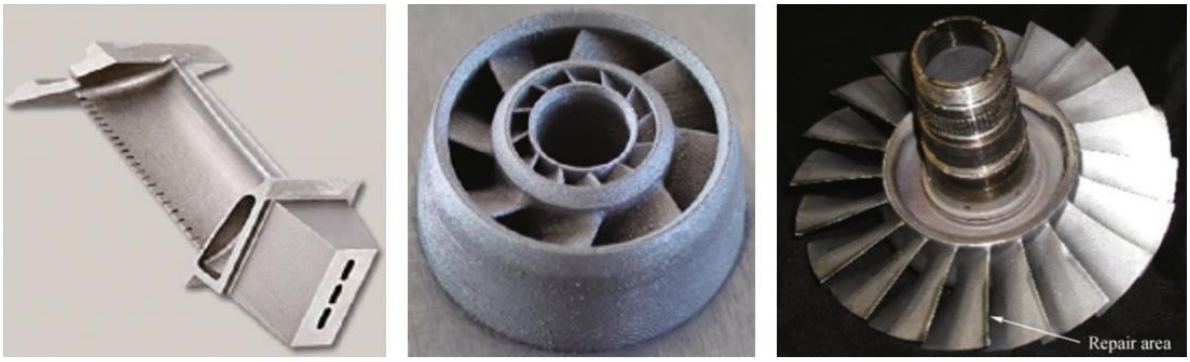

Figure 4 – (a) Turbine blade with internal cooling channels produced by SLM (Source: Concept Laser [18]); (b) Hollow static blade casting using the mold and cores fabricated by 3DP (Source: ExOne [19]); (c) Damaged blisk repaired using LENS (Source: Optomec [20]).

2.1.5.2 Automotive

Development of new products is critical in the automotive industry, but usually in a costly, time-consuming process. The automotive industry has been using AM technologies as an important tool in the design and manufacturing of components because it can shorten the development cycle and reduce manufacturing and product costs. Additionally, AM technologies have been used to produce small batches of structural and functional parts, such as engine exhausts, drive shafts, gear box components and breaking systems (Figure 5) for motorsport and racing vehicles that usually use lightweight alloys and have highly complex geometries and low production volumes [2, 3, 12, 21].

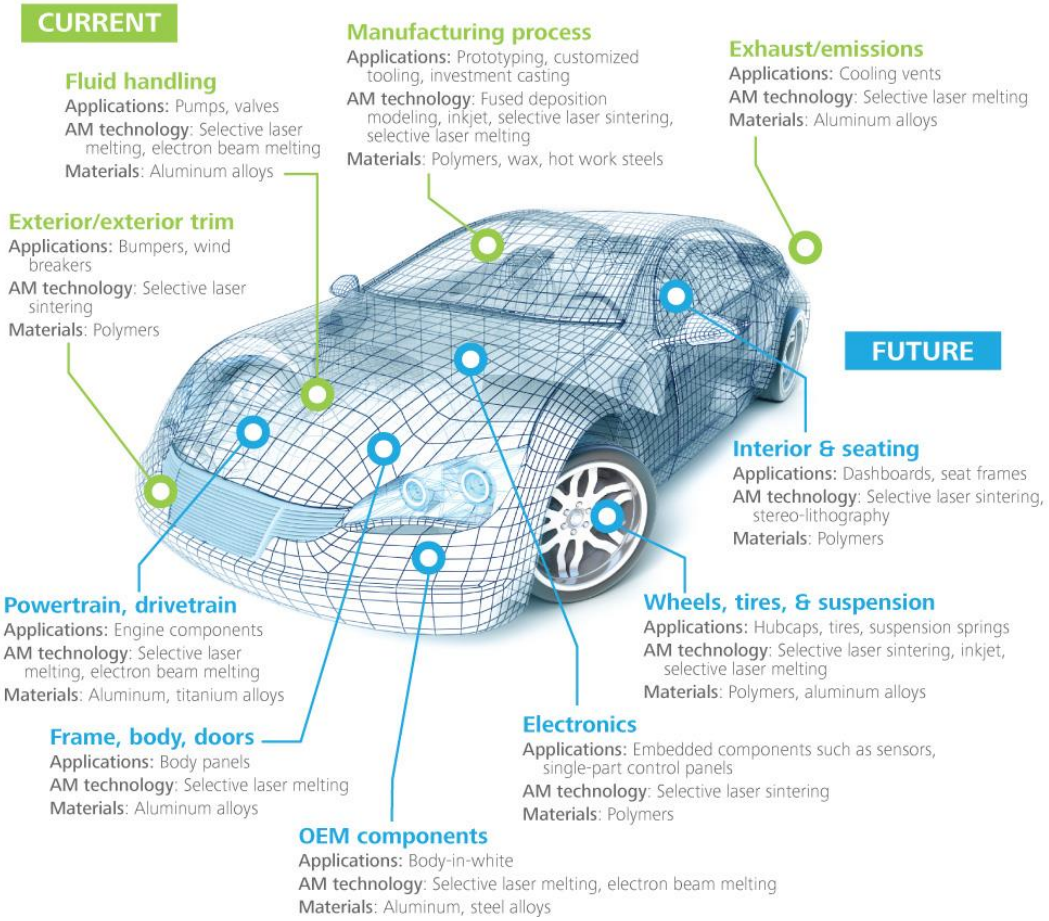

Figure 5 – Illustrative applications of AM in a motorsport vehicle [21].

2.1.5.3 Biomedical

Recent developments in AM, as well as in biomaterials and biological sciences, have extended the applications of AM techniques in the biomedical industry for the fabrication of custom-shaped orthopedic prostheses and implants, medical devices, biological chips, tissue scaffold, artificial organs, medical devices and micro-vasculature networks [2, 3]. The year 2013 marked the 15th year of cell printing, an ambitious vision to create a developmental biology-enabled, scaffold-less technique to fabricate living tissues and organs by printing living cells [22, 23].

2.2 Metal Additive Manufacturing

2.2.1 Introduction

Used for more than 30 years, AM techniques are no longer confined to rapid prototyping applications, being mostly used in niche markets (aerospace, automobile, biomedical…) to manufacture metallic parts.

AM has grown and changed tremendously since researchers in Austin, TX, developed of what is arguably the first machine in the lineage of metal AM: a laser used to selectively melt layers of polymer and, later, metal. Even though AM has been around as a means of processing materials for at least three decades and the development of metal AM processes has made a huge progress, there is still development issues in terms of processing and materials. Understanding the various AM systems to produce metal parts, as well as the issues associated with them, is critical to improving the capabilities of the hardware and the materials that are produced. Moreover, they should provide improvements in terms of time-to-market, ecological impact and design compared to traditional industrial processes [24-26].

2.2.2 Metal Additive Manufacturing Systems

As described in section 2.1.3, there are several systems to classify AM processes, such as in terms of material feed stock, energy source or build volume. Table 3 presents a list of equipment manufacturers and their equipment for metal AM techniques. In this table, the AM processes are divided into three broad categories: Powder Bed Fusion Systems, Powder Feed Systems, and Wire Feed Systems. The last two can be merged into one big category named Direct Energy Deposition (DED) systems. The build volume and energy source are also provided [27].

In this review, each category for metal AM is briefly explored, mentioning its working principle, energy source and advantages; however, more focus is given to powder bed systems as it is directly related to the scope of the research being presented. Additionally, it should be noted that this review will only include AM technologies that directly form metallic parts or deposit metals. “Indirect” processes, where a casting insert is produced for a mold then formed into a part, or a “green” body where extensive post processing is required are not included [26]. Furthermore, the focus will be on the build stage of the AM process, since the post processing operations will be discussed in section 2.2.5.

Table 3 – Metal AM equipment sources and specifications. Adapted from [27].

System	Process	Build volume (mm)	Energy source
Powder bed			
ARCAM (A2X) [a]	EBM	200 x 200 x 380	7 kW electron beam
EOS (M280) [b]	DMLS	250 x 250 x 325	200-400 W Yb-fiber laser
Concept laser cusing (M3) [b]	SLM	300 x 350 x 300	200 W fiber laser
MTT (SLM 250) [b]	SLM	250 x 250 x 300	200-400 W Yb-fiber laser
Phenix system group (PXL) [c]	SLS	250 x 250 x 300	500 W fiber laser
Renishaw (AM 250) [d]	SLM	245 x 245 x 360	200 or 400 W laser
Realizer (SLM 250) [b]	SLM	250 x 250 x 220	100, 200, or 400 W laser
Matsuura (Lumex Avance-25) [e]	SLS	250 x 250 diameter	400 W Yb fiber laser; hybrid additive/subtractive system
Powder feed			
Optomec (LENS 850-R) [f]	LENS	900 x 1500 x 900	1 or 2 kW IPG fiber laser
POM DM3D (66R) [f]	DMD	3200° x 3670° x 360°	1-5 kW fiber diode or disk laser
Accufusion laser consolidation [g]	LC	1000 x 1000 x 1000	Nd:YAG laser
Irepa laser (LF 6000) [c]	LD		Laser cladding
Trumpf [b]	LD	600 x 1000 long	
Huffman (HC-205) [f]	LD		CO_2 laser cladding
Wire feed			
Sciaky (NG1) EBFFF [f]	EBDM	762 x 483 x 508	>40 kW @ 60 kV welder
MER plasma transferred arc selected FFF [f]	PTAS FFF	610 x 610 x 5182	Plasma transferred arc using two 350A DC power supplies
Honeywell ion fusion formation [f]	IFF		Plasma arc-based welding

Country of Manufacturer: (a) Sweden; (b) Germany; (c) France; (d) UK; (e) Japan; (f) USA; (g) Canada

2.2.2.1 Powder Bed Fusion Systems

Most current metal AM systems are of the powder bed fusion type [28]. Powder bed fusion is "an additive manufacturing process in which thermal energy selectively fuses regions of a powder bed" [29]. In this type of metal AM processes thin layers of powder are applied to a build plate and an energy source (laser or electron beam) is used to fuse the powder contained in a bed. The powder bed fusion process is also known as selective laser melting (SLM), selective laser sintering (SLS), direct metal laser sintering (DMLS), direct metal laser melting (DMLM), and electron beam melting (EBM). Current powder bed fusion systems tend to use

melting instead of sintering, as it provides more dense parts: re-melting previous layers during the melting of the current layer allows a better adherence [24, 30].

Metal powder bed fusion AM systems have designs similar to that presented in Figure 6. They are composed of a powder delivery and energy delivery systems and use two beds of powder: one where the part is built (fabrication powder bed) and one holding the reserve powder. The powder delivery system comprises a feeding system (e.g. a piston) that delivers the powder from the reservoir bed, a spreader (or a rake in case of EBM) to create the powder layer on the build area, and a piston that holds the part being produced. The energy delivery systems is made up of a laser or an electron beam, and a scanner system with optics that enables the delivery of a focused spot to all points of the build platform [15, 24, 27, 30].

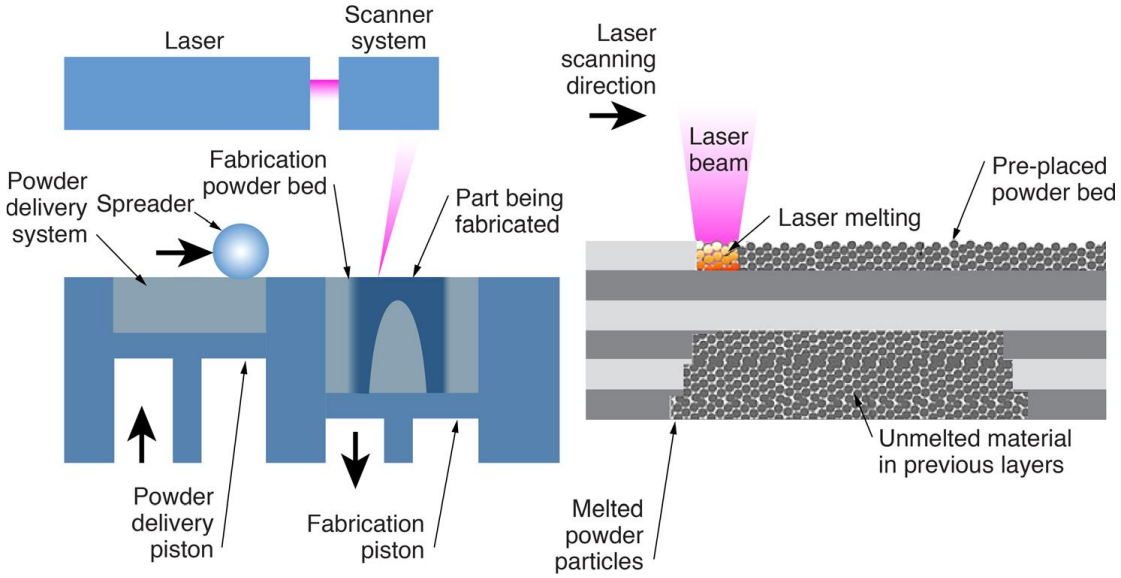

Figure 6 – Schematic overview of the SLM process [31].

In powder bed AM systems, the build envelope is an enclosed chamber that can be operated in vacuum or filled with an inert gas (usually nitrogen or argon) with the intention to (a) prevent oxidation of reactive metal powders like titanium and aluminum and (b) to clear any "spatter" and metal fumes that are created from the laser path [26, 30]. The chamber is then pre-heated to a pre-determined temperature depending on the process (around 100°C for laser based and 700°C for electron beam) [26]. The energy source is then programmed to deliver energy to the surface in the pattern of the part, building up a single layer, usually between 20 and 200 µm thick [26]. To create more layers, the build area and the reservoir bed move downward and upward respectively, the leveling system provides a fresh powder layer on the top, and the process is repeated until the 3D component is made.

Powder bed fusion processes require certain steps: machine set-up, operation, powder recovery, and substrate removal [24].

A powder bed fusion machine requires a build substrate, or “start plate”, to provide mechanical and thermal support to the build material. When sequential layers of powder are distributed (rolled or raked out), existing layers of the build must not move; the substrate gives a mechanical support. Moreover, the substrate also provides a thermal path to dissipate heat, which is especially important to building overhangs on top of loose powder (prone to swelling and other process defects cause by local temperature fluctuations) [24].

During production, the machine is governed by the details of scanning (or exposure) strategy and processing parameters, which will be discussed in section 2.2.4. The scanning strategies, characterized by the length, direction, and separation of neighboring scan vectors, can affect the properties of the part including density, mechanical behavior and residual stresses. Residual stress is one of the critical material responses, as it can put the part out of tolerance when removed from the build plate [24, 30].

After the part is build, excess powder must be removed from the build chamber and the build substrate need to be removed. Depending on the process material, the substrate can adhere to the part and it must be cut off, with abrasive saws and wire EDM being common methods [24]. Post-processing operations like hot isostatic pressing (HIP) and surface finishing are then applied.

Powder bed systems have the ability to produce high resolution features and internal passages as the powder can be used to support the part. It also provides a good dimensional control and small layer thickness. However, the envelope size is a limitation when compared to other metal AM systems [15, 27].

2.2.2.2 Powder Feed Systems

Another approach to metal AM uses powder injection to provide the material to be deposited. Instead of a bed of powder that is reacted with an energy source, powders is injected through a nozzle that then is melted with a laser into the shape desired. The powder may be injected through an inert carrier gas or by gravity feed. Also, a separate supply of shielding gas is used to protect the molten weld pool from oxidation [26].

Figure 7 shows a generic illustration of powder feed systems. As mentioned, the powder is conveyed onto the build surface and a laser is used to melt a monolayer or more of the powder into the shape desired. This processes is repeated until the solid 3D component is made [27].

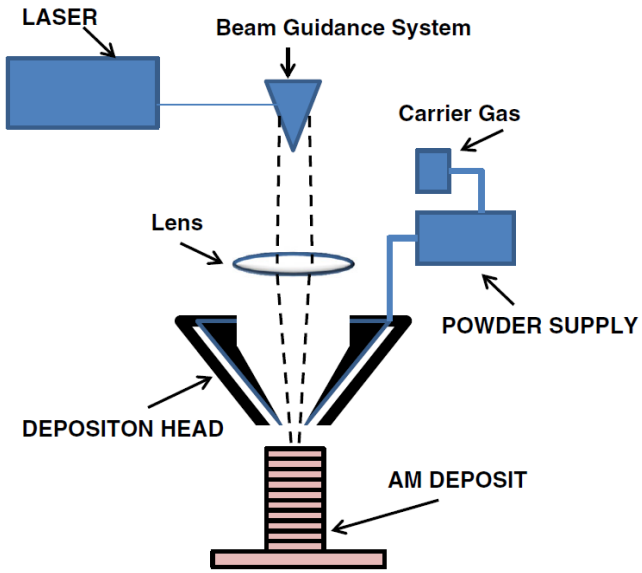

Figure 7 – Generic illustration of an AM powder feed system [27].

There are two dominate types of systems in the market: (1) the work piece is stationary and the deposition head moves, and (2) the deposition head is stationary and the work piece is moved [27].

The powder feed approach is valuable because of its larger build volume and ability to be used to refurbish worn or damaged components. On the other hand, these systems are not able to deposit the same volume of material as the powder bed systems [26, 27].

2.2.2.3 Wire Feed Systems

Figure 8 shows a schematic overview of a wire feed system. In these systems, the feed stock is a wire and the energy source for these unites include electron beam, laser beam, and plasma arc. At first, a single bead of material is deposited and upon succeeding passes is built upon to produce a 3D structure. [27]

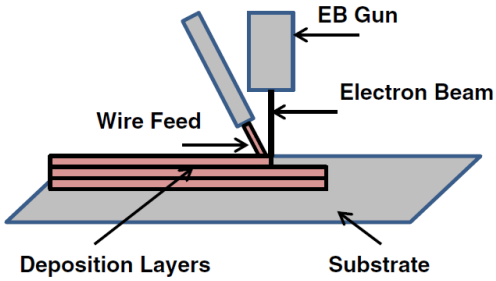

Figure 8 – Schematic view of an AM wire feed system [27].

In general, wire feed systems are well suited for high deposition rate processing and have larger build volumes than the two powder-based approaches; however, the fabricated parts have lower dimension accuracy and therefore need more extensive machining [26, 27].

2.2.3 Evaluation of the Metal Additive Manufacturing Processes

A lot of studies have been made with the purpose of designing test parts and evaluating metal AM process [32-35]. Frederico Gomes [35] has compared the EBM, SLM and DMLS processes where he found that due to the wide range of processes, these studies prove difficult use and show partial results.

The main criteria used to evaluate a process come from the time-cost-quality triangle, with the addition of the environmental impact. Table 4 presents a comparison of the most used metal AM processes regarding the quality and time criteria.

Table 4 – Specifications of metal AM processes. Adapted from [25].

Process	Rugosity (µm)	Accuracy (mm)	Post-processing	Building speed (cm^3/h)	Layer thickness (µm)
SLS	Ra 2	0.2	Cleaning Infiltration	10-100	20-150
DMLS	Ra 11	0.1-0.2	Cleaning Infiltration [(a)]	7-70	20-100
SLM	Ra 11	0.2	Cleaning	5-20	20-100
EBM	Ra 25-35	0.4	Cleaning	55-80	50-200
DMD	Ra 10-25	0.3	Cleaning	10-70	NA

Notes: (a) not mandatory, but recommended as it provides better quality; all process required finishing operations if better surface or dimensional quality is needed.

2.2.3.1 Quality

The quality of parts manufactured with this kind of processes can be evaluated according to 2 sub-criteria: (a) surface and dimensional quality, and (b) materials and mechanical properties.

2.2.3.1.1 Surface and dimensional quality

Components produced with metal AM systems usually present a granular aspect due to the binding of unmolten particles on the exterior surfaces. The surfaces build with SLS and DMLS, both with infiltration, have a better quality than the ones made through SLM and unfiltered DMLS, due to the infiltration, which smoothens the surfaces [32]. On the other hand, the dimensional precision is also a very important aspect in choosing the most suitable method for a given component. SLM, DMLS and SLS processes produces parts with better accuracy than EBM and DMD, as it can be seen in Table 4. It should be noted that these values are only an estimate and better surface and dimensional quality could be provided with smaller AM

machines. In conclusion, when better surface or dimensional quality is needed, finishing operations are necessary [25].

2.2.3.1.2 Materials and mechanical properties

Due to its development, metal AM processes has been widening the range of materials that can be processed. The increase in power of the laser sources in SLS, DMLS and SLM allow the use of high melting point metallic alloys, including steels, cobalt-chrome, aluminum, bronze, and titanium. EBM systems can also use inconel, copper, beryllium and niobium, due to a higher energy source [25].

Regarding mechanical properties, a lot of studies have been and are being conducted in order to proper evaluate and compare metal AM processes. L.E. Murr et al. [16] recently intimated that both EBM and SLM "have demonstrated the ability to build simple geometries having a microstructure which gives rise to a mechanical behavior similar to and superior to wrought or cast Ti–6Al–4V products". However, future research addressing all the possible variations of process parameters is needed in order to fully understand the quality of metal AM parts.

2.2.3.2 Time

Few papers focus on the manufacturing speed of metal AM processes since it is difficult to build part under the same circumstances. The data presented in Table 4 are given by manufacturers for "medium sized" build volumes (of at least 200 x 200 x 200 mm^3).

The manufacturing speed is a combination of a lot of factors, such as building speed, layer thickness, density of built parts, and post-processing operations. AM process based on sintering, SLS and DMLS, are fairly faster than SLM. DMD and EBM are able to produce non-porous parts, as SLM does, with higher building speed. This data is usually measured for maximum layer thickness. However, when building a part, a lower layer thickness should be chosen in order to achieve better resolutions, hence limiting finishing operations [25].

Despite SLS and DMLS have similar building speed than EBM and DMD processes, they require an infiltration to obtain a nearly fully dense part [36]. Therefore, EBM and DMD are the fastest processes to produce parts without specific finishing operations.

2.2.3.3 Cost

Metal AM processes are adequate for small to medium batches. Atzeni and Salmi [37] described that AM is penalized by the high costs of materials, and as soon as AM technologies

diffuse as a common manufacturing process, it is expected for AM systems cost to decrease and consequently to move towards larger production volumes.

Manufacturing cost depends on machine operating cost, raw material and consumables costs, manufacturing time, among others. On a general level, for a medium building chamber volume, SLS and DMLS are less expensive than EBM and DMD. The high price for these systems is balanced by the very short pre-production phase for small series. The cost of powders is influenced by the atomization process which reduces the cost between different alloys [25].

2.2.3.4 Environmental Impact

Al the powder-based systems have a recovery system to recycle the unused powder. According to Arcam [38], 95% of the unused powder can be filtered and used again right away. Moreover, the ability to build less massive parts and closer to the final shape interest greatly to eco-designers [39]. Kellens et al. [40] quantified the environmental impact of SLS and SLM machines and concluded fabrication impact can't be disregarded compared to extraction and creation phases. An interesting approach would be to compare these performances to those of traditional mechanical processes, since newly-built parts only need the cleaning of the remaining powder which contributes to the limitation of waste generation [25].

2.2.4 Material Processing Issues

Despite the differences between the several metal AM systems, they share the same materials processing issues. In this review these issues will be explored, mentioning differences between AM processes where appropriate.

Like traditional manufacturing processes, porosity is a concern in metal AM. Other defects, such as residual stresses and cracking, are exclusive to welding and metal AM. The scanning strategy, process temperature, feedstock quality, building chamber atmosphere and many other inputs determine the occurrence and quantity of defects. Therefore, understanding the complex relationship between process inputs, defects, and the product of an AM process, can help operators improve process reliability and the quality of the parts produced [24].

Figure 9 illustrates a general process flow chart. The process inputs, in blue, are AM hardware and software, part geometry, scan strategy, feedstock quality and build chamber atmosphere. The process outputs, in red, are mechanical properties (static and dynamic), minimization of failed builds and geometry conformity (feature size and geometry scaling). The green box encloses the thermal interactions due to applied energy, beam interactions, heat transfer and process temperature. If properly modelled, these interactions can describe dynamic

process temperature, which is probably the most defining quantity of metal AM processing. In the following sections, the above issues will be briefly discussed.

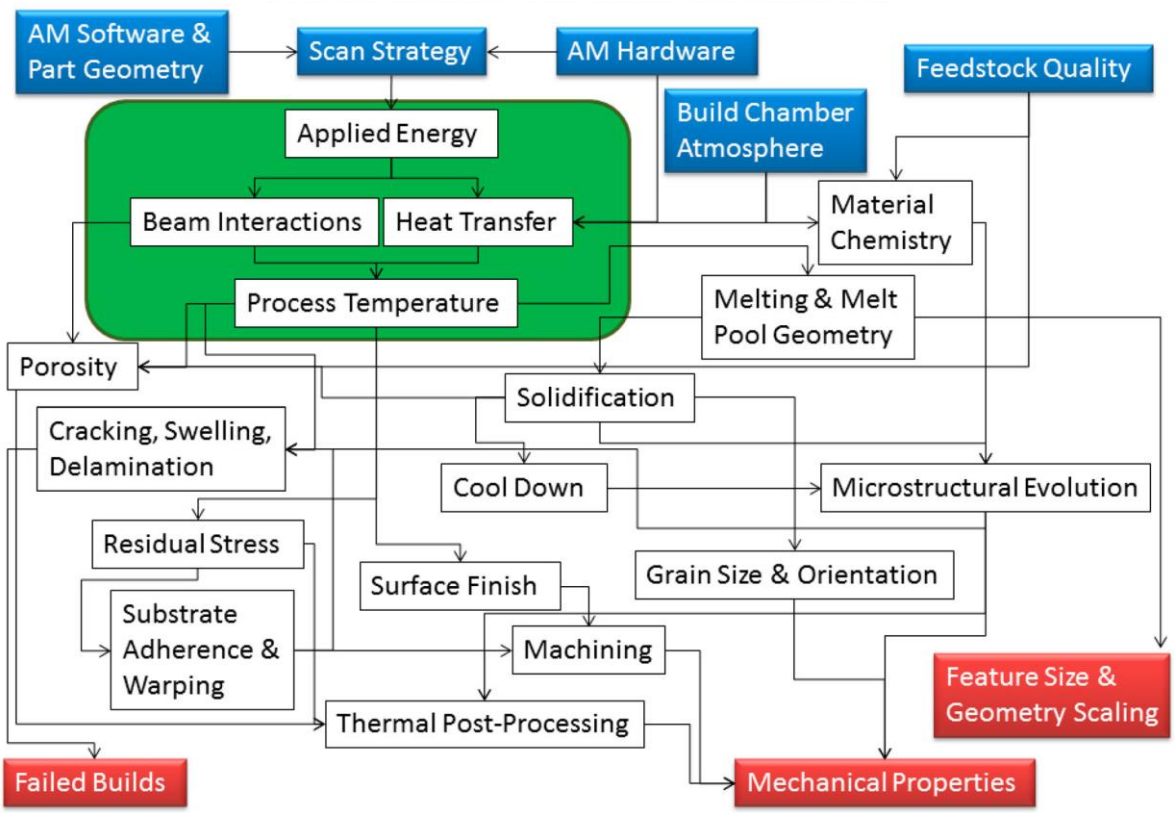

Figure 9 – Overview of relationship between input parameters and underlying physics to meet to expected outcome of metal AM [24].

2.2.4.1 Feature Size, Surface Finish and Geometry Scaling

When printing metal parts, the minimum feature size, surface roughness and geometrical accuracy are typical concerns for operators, but overemphasis of these properties is not useful for most applications since the part surface will be machined after thermal-post processing [24].

The minimum feature size is determined by the minimum diameter of the heat source and the size of the feedstock. As it can be seen in Table 5, powder-based processes have better resolution due to the use of finer feedstock (powder vs. wire), with the resolution of powder bed systems better than powder feed systems. Due to small feature size, powder bed systems are more suitable for complex geometries, such as metal mesh or foam structures. On the other hand, wire feed technology is limited to near-net shapes and the final geometry and details or obtained by machining [24].

Table 5 – Typical layer thicknesses and minimum feature sizes of metal AM processes. Adapted from [24].

System	Typical layer thickness (µm)	Minimum feature size or beam diameter (µm)
Powder bed		
SLM	10-50	75-100
EBM	50	100-200
Powder feed - DMD	250	380
Wire feed	3000	16000

Regarding surface roughness, there are two separate contributors: (1) non-flat layer edges or layer roughness and (2) the actual roughness of the metal surface. The layering effect (Figure 10) can be reduced by using smaller layer thickness values, which means longer build times, since the layer thickness determines the division of a part into a number of layers. The actual roughness of the metal surface depends upon the details of the machine. Powder bed systems typically have finer resolution and layer thickness, but are prone in satellite formation due to sintering of powder at part edges [41]. Consequently, SLM results in a better resolution than EBM, since finer powder means smaller satellites and less surface roughness [24].

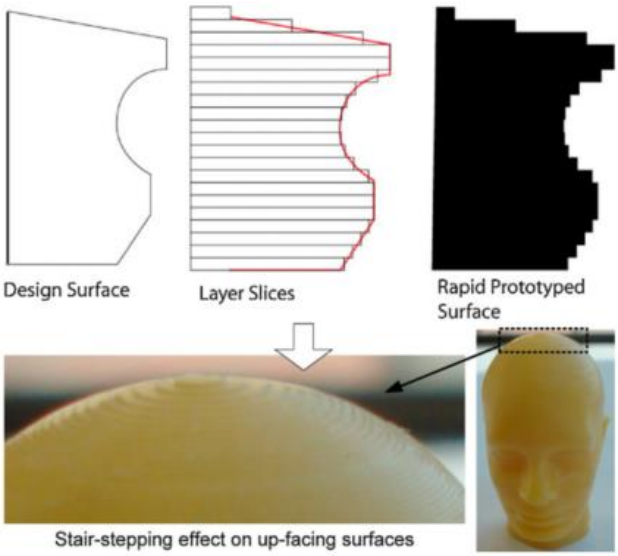

Figure 10 – Illustration of the layering effect, also known as stair-stepping effect, of a layer-based AM process [42].

Geometrical accuracy can be measured by 3D scanning the product and calculating the deviation relative to the original model. Typical corrections are empirical modifications to scale the part in a Cartesian system, which is accounted for during machine calibration. Nevertheless, since post-process machining is usually applied to metal AM parts, the minimum feature size,

part tolerance and surface finish are dictated by the machining step. Hence, work to refine surface finish using smaller powder and layer thicknesses may just increase process time and cost without improving the quality of the final part [24].

2.2.4.2 Build Chamber Atmosphere

The atmosphere under the metals are processed strongly affects chemistry, processability and heat transfer. Usually inert gas and/or vacuum systems are used, and each leads to unique processing issues. Because most of the metal powders have a tendency to oxidize and adsorb moisture when exposed to air, especially at high temperatures, AM processes need to use inert shield gases. DMD typically operate with a shield gas flowing over the melt surface and may operate under an inert atmosphere [24].

For SLM processes the machine runs in an inert atmosphere of argon or nitrogen filling or flowing over the build surface. Ferrar et al. [43] proved that flow of the fill gas and pathway affects in porosity reduction in SLM Ti6Al4V. Small features may lead to heat concentration in SLM, which can cause localized oxidation [24].

EBM systems use a heat filament to generate electrons, which requires a vacuum-capable build chamber. During beam operation, a small quantity of helium is injected to reduce electrical charging of the build volume, raising the pressure of the build chamber. Operating in such conditions leads to increase melt vaporization and exceptional heat transfers consequences [24].

2.2.4.3 Feedstock quality

The quality of the final part is highly affected by the quality of the feedstock that is used. The quality of the powder is determined by size, shape, surface morphology, composition and internal porosity. Due to the variety of atomization techniques to produce metal powders, there are distinct variations in powder quality. Likewise, there are several unique quality issues related to wire feedstock. By understanding feedstock quality, the operator can select the optimal material for a given system. For more information on the standards associated with quantifying powder characteristics and the details of powder science consult Ref. [44].

As mentioned, the quality of the powder is directly related to the production technique. A large variety of techniques to produce metal powders, including gas atomization (GA), rotary atomization (RA), plasma rotating electrode process (PREP), and plasma atomization (PA). Some techniques yield irregular shapes (like RA), other have a large amount of satellites (like GA), and some are highly spherical and smooth (like PREP and PA). Figure 11 shows the surface morphology and shape, as well as the cross-sections for internal porosity analysis.

Porosity in powder feedstock is common in some techniques, like GA, that entrap inert gas during production. This entrapped gas in the then transferred to the part due to rapid solidification, resulting in powder-induced porosity. Higher quality powder, like the ones produced via PREP, do not contain such pores and have been used to eliminate the powder-induced porosity [45].

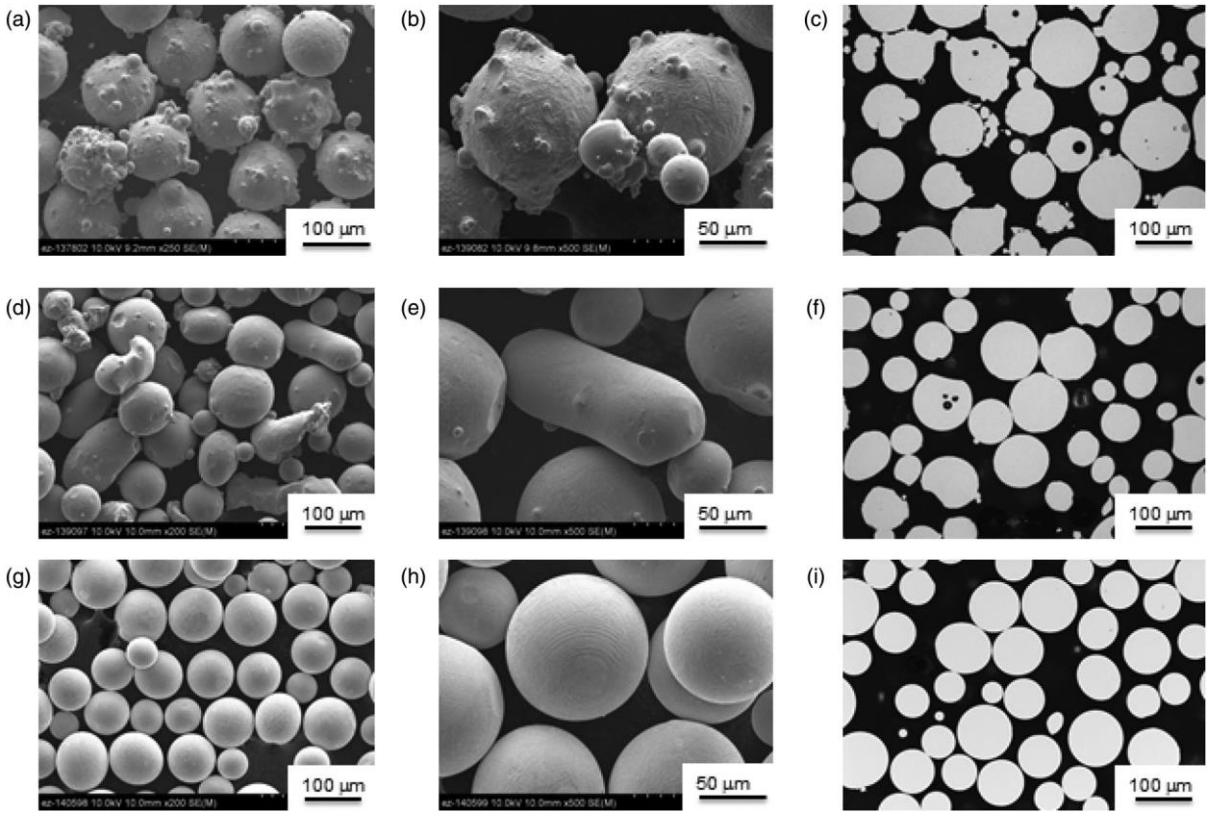

Figure 11 - Comparison of powder quality: (a) SEM 250× of GA, (b) SEM 500× of GA, (c) LOM of GA, (d) SEM 200× of RA, (e) SEM 500×of RA, (f) LOM of RA, (g) SEM 200× of PREP, (h) SEM 500× of PREP, (i) LOM of PREP [45].

The nominal particle size distribution of powder used in metal AM processes is presented in Table 6. SLM uses a finer particle distribution of powder to improve surface finish by enabling smaller layer thicknesses and reducing satellite formation [24]. EBM uses a slightly larger size distribution, but can use smaller sizes without compromising chemistry, material properties or microstructure [46].

Flowability (how well a powder flows) and apparent density (how well a powder packs) are important quantitative powder characteristics that are directly related to qualitative characteristics [47, 48]. Spherical particles improve flowability and apparent density. Smooth particle surfaces are better than surfaces with satellites or other defects. Fine particles typically improve apparent density by filling interstitial space between larger particles, but flowability

may be reduced. The effect of flowability on processability using different hardware is not well published; tough it is known its importance for industrial producers of AM parts [24].

Table 6 – Typical feedstock dimensions for metal AM processes. Data from [49-51].

System	Particle size distribution of powder or wire diameter (μm)
Powder bed	
SLM	10-45
EBM	45-106
Powder feed - DMD	20-200
Wire feed	2400

Moreover, the chemical composition of the powders must remain within alloy-specific specifications. The elemental composition of recycled powders must be measured to report evaporation losses, contamination from powder recovery, and reaction with oxygen, nitrogen or other gases. A recent study [52] suggested that reused powder showed no measurable undesired influence on the AM process of Ti6Al4V, despite changes in chemical composition. In fact, the flowability of the powder improved with more reuse cycles (due to absence of satellite particles and reduction in humidity) as well as the yield strength and ultimate tensile strength, whereas the elongation was unaffected.

Regarding wire feed systems, the wire feedstock shows minimal defects compared to powder since the technology is transferable from wire making for welding consumables supply chains. Better quality wire means less variation in wire diameter, which affects the amount of porosity in the weld deposit, along with adsorbed moisture [53]. For reactive metals like titanium, surface adsorption and reactions with atmosphere may also cause defects. More notably, cracks or scratches on the wire surface can translate directly to porosity formation. Unlike powders, gas porosity is not an issue for wire feedstock [24].

2.2.4.4 Beam-powder Interactions

The interactions between heat source and feedstock or melt pool impacts the utilization of energy and can lead to liquid metal ejection and porosity. There are four basic modes of particle ejection during beam melting processes: (a) convective transport of liquid or vaporized metal out of the melt pool (or spatter ejection), (b) electrostatic repulsion of powder particles in EBM, (c) kinetic recoil of powder in DMD, and (d) enhanced convection of powder in gas streams. E-beams incur backscatter losses of electrons, whereas laser incur intensity losses due

to reflection. E-beam systems must be designed to reduce electrical charge build up, while DMD systems must consider the effective feed rate of powder, as appropriate amounts of material must be deposited [24].

Spatter ejection is caused by the application of a high-energy beam creating localized boiling, where the energy of the ejected droplet must overcome surface tension forces [54]. These particles can be identified in metal AM by the high-temperature emission light, which is the reason that these ejected droplets are commonly referred as “fireworks”.

In laser-based techniques, spatter ejection can occur along with low energy absorption. Since a laser imparts energy to the powder bed via photons, the reflectivity of the metal powder is an issue, as some of the energy will not be absorbed [55]. Depending on the metal, this can be a big limitation. To overcome this barrier high-power lasers are used, which can lead to increased spatter ejection [56]. Pulse shaping has shown promise to increase energy absorption and decrease spatter ejection, as it can be used to more slowly heat a melt area causing a decrease in reflectivity with higher temperatures [41].

In the EBM process, electrons interact with the material to transfer not only energy but also electrical charge. If repulsive electrostatic forces are greater than the forces holding particles to the powder bed, the particles can be ejected, causing “smoking” (cloud of charged powder particles) if sintering is not properly achieved [57]. This effect can be reduced by using a rapidly scanned, diffused beam to slightly sinter the powder prior to melting. Helium gas is also injected during melting to dissipate charge from the melt surface.

Powder can also be removed by kinetic recoil and convection of powder in the fill or shield gas steam in DMD systems. As the powders are deposited into the melt pool, some particles will recoil and avoid deposition, which can lead to a significant loss of powder (if not recovered). Some of these powders may appear as dust in the fill gas of inert atmosphere; though particles lost in this are not significant compared to other loss mechanisms. Both kinetic recoil and convection do not remove particles from the melt pool and, therefore, do not have a high importance for control of porosity. On the other hand, electrostatic repulsion and spatter ejection may lead to process-induced porosity [24].

2.2.4.5 Porosity

Porosity is one the most common defects in metal AM and can decrease mechanical properties. Porosity can be powder induced, process-induced or an artefact from solidification. For most studies, porosity formation is dominated by processing technique and process parameters must be properly defined to avoid a range of mechanisms that can create pores.

Process-induced porosity is formed when the applied energy is not sufficient for complete melting or spatter ejection occurs. The pores formed are typically non-spherical and come in a variety of sizes. When the energy source power is not enough, lack of fusion can occur, which can be identified by regions of un-melted powder visible in or near the pore. If the applied power is too high, spatter ejection may occur in a process known as keyhole formation, which in case of SLM can produce a trail of voids [58]. Process-induced porosity has other contributors, such as the effect of powder consolidation from a loosely packed powder bed into a fully-dense part [59]. Powder is distributed onto the processing surface and particles larger than the layer thickness are intended to consolidate into a layer of correct height, resulting in a phenomenon called shrinkage porosity (or "hot tearing") [24].

2.2.4.6 Scan Strategy

Various scan strategies have been developed and are depicted in Figure 12. For feed-based systems strategies tend to be relatively simple, such unidirectional (Figure 12a) and bi-directional (Figure 12b). These strategies use rectilinear infill to melt a give part layer. For SLM and EBM, other strategies have been developed besides unidirectional and bi-directional. In SLM, island scanning (Figure 12c) has been used to reduce residual stress [60]. Island scanning is a checkerboard pattern of alternating unidirectional fills and reduces temperature gradients in the scan plane (x–y plane) by distributing the process heat. In EBM, spot melting (Figure 12d, e) is common practice to melt contours, which are boundaries between infill and the powder bed. SLM systems also used contours, though contour melting strategy is typically linear (Figure 12f). Contour passes are done after melting in SLM to refine surface finish [60], whereas in EBM are done prior melting [24].

The scan strategy for a give build can be adjusted by layer or by part, and has a direct impact on process parameters: heat source power and velocity must be optimized for a given scan strategy. The relationship between heat source power and heat source velocity is a key parameter for metal AM processes, as it is important for eliminating process-induced porosity and determining grain morphology [24].

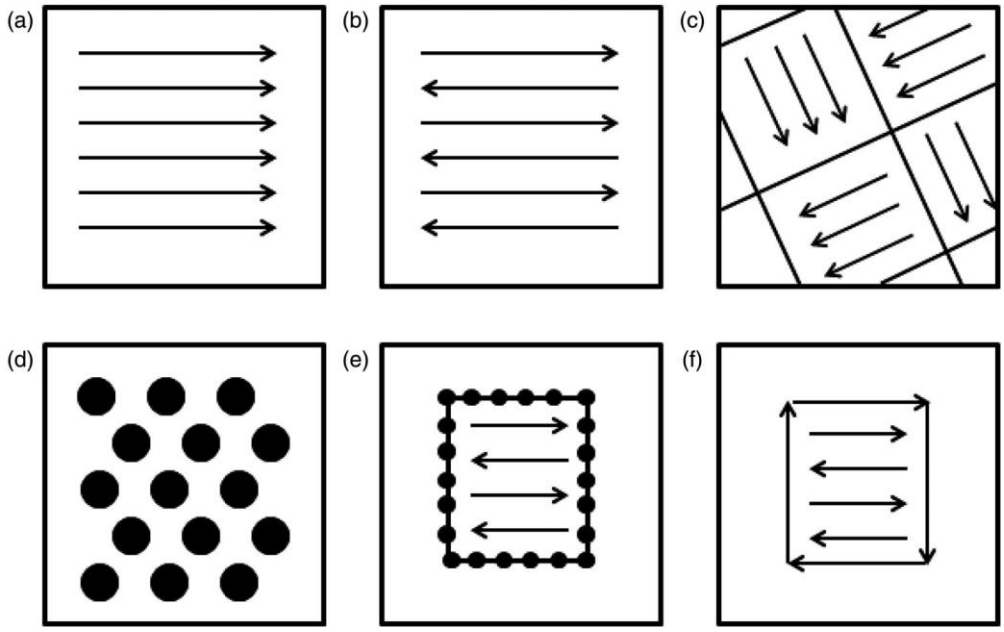

Figure 12 - Scan strategies used to determine heat source path in metal AM as seen in the X-Y plane (perpendicular to the build direction): (a) unidirectional or concurrent fill; (b) bi-directional, snaking, or countercurrent fill; (c) island scanning; (d) spot melting; (e) spot melting contours with snaking fill; and (f) line melting contours with snaking fill [24].

2.2.4.7 Deposition Strategy

The way in which feedstock is delivered to the melt surface controls deposition rate and can have a strong effect on material defect and properties. In wire feed systems, the vertical and horizontal angle of the wire feed are related to deposition efficiency, surface roughness, incomplete melting, rippling and other processing effects [61]. On the same say, the angle of powder spraying is important for powder feed systems, and in both of them the deposition rate is critically important. The deposition rate and the velocity of the heat source determine how much material is going to be deposited in a given pass. In these systems, the build-up of material must be considered in order to properly choose the layer thickness [24].

For power bed system, the layer thickness determines how much powder is "raked". A "rake" is a bar that sweeps out powder onto the build surface. The number of passes, mechanical type of rake and the amount of powder being retrieved by pass determine the efficiency of these systems [24].

2.2.4.8 Cracking, Delamination and Swelling

The formation of defects is basically dependent on process temperature. Cracking of the microstructure may occur in solidification or subsequent heating. Macroscopic cracks may relate to other defects like porosity. Delamination may lead to interlayer cracking. If the process temperature is too high, a combination of melt pool size and surface tension may lead to

swelling or melt balling. If processing conditions are properly controlled, most of these defects can be avoided [24].

Cracking of the microstructure is dependent on process temperature and material properties. There are different material-dependent mechanisms for which cracks form in AM [60], including: (a) solidification cracking, (b) grain boundary cracking. Solidification cracking occurs if too much energy is applied and arises from the stress induced between solidified areas of the melt pool and non-solidified areas. This type of cracking depends on the solidification nature of the material (dendritic, cellular or planar) and is usually due to insufficient flow of liquid to inadequate supply, flow obstruction by solidified grains or high strain on the melt pool. Grain boundary cracking is cracking that nucleates or occurs along grain boundaries of the material and is related to formation or dissolution of precipitate phases and the grain boundary morphology. [24, 62] Both of the phenomena are microstructure related. Generally, cracking refers to macroscopic cracks that usually occur due to other macroscopic defects such as delamination [63].

Delamination is the separation of adjacent layers within parts, as shown in Figure 13a. This may due to incomplete melting between of powder or insufficient re-melting of underlying solid. Despite lack-of-fusion defects are localized with the interior of the part and mitigated with post-processing, delamination defects are macroscopic and cannot be repaired by post-processing. Substrate heating can be a solution to decrease macroscopic cracking in SLM [24, 63].

Swelling or melt balling are both related to material overheating. This type of defects usually occur due to small features or overhangs in part geometry, typically made with support structures that help prevent deformation from gravity or growth stress (mechanical support) or proving a conductive path away from the melt surface (thermal support). Swelling is the rise of solid material above the plane of powder distribution and melting (Figure 13c). Melt ball formation is the solidification of melt material into spheres instead of solid layers, wetted onto the underlying part. Melt ball formation is an extreme condition typically only observed during material development and it occurs with higher temperatures or alongside delamination with lower temperatures. Both of these phenomena are due to surface tension effects related to the melt pool geometry [24, 45, 64].

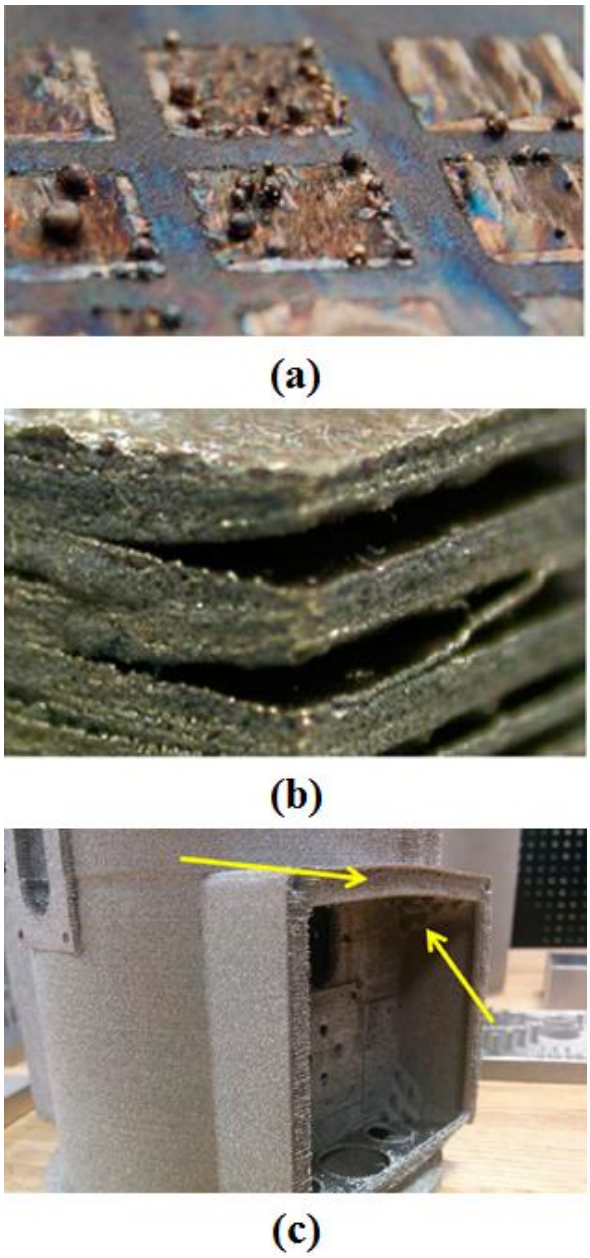

Figure 13 – Delamination (a) and melt ball formation (b) in EBM stainless steel [65]; Slightly deformed overhang in EBM Ti6Al4V [24].

2.2.4.9 Substrate Adherence and Warping

The use of substrate for the deposition of material is a standard practice in metal AM processes, but it adds post-processing work. Metal AM processes build on top of a metal substrate to achieve mechanical adherence of the first layers of the melted part [45]. Substrates may wrap during use as shown in Figure 14. Substrate warping is a form of stress relief that results in permanent plastic deformation. This can be due to the operating temperature of the metal AM process, the heat treatment of the substrate prior to use or due to differential coefficients of thermal expansion. The ultimate result of substrate warping is distortion of

geometry with the affected layers and possible lack-of-fusion or delamination at the transition region back to unaffected material [24].

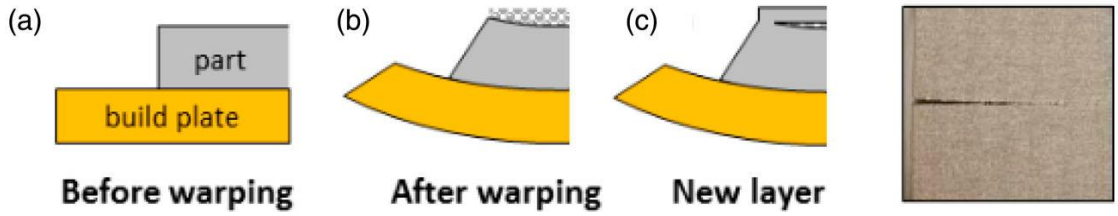

Figure 14 – Schematic of build plate warping effect during processing (a-c) and resultant damage [66].

2.2.4.10 Residual Stress

Residual stress is common in metal AM materials due to large thermal gradients during processing, and it can negatively affect mechanical properties and induce changes in grain structure. Residual stress is a stress within a material that persists after the applied stress is removed. Two situations can befall from this effect: (a) the stress exceeds local yield stress, resulting in warping or plastic deformation; or (b) the stress exceeds the local ultimate tensile strength, resulting in cracking or other defects. Macroscopic residual stresses can dramatically affect the AM part behavior, whereas microscopic residual stresses from precipitates or atomic dislocations are more localized. Macroscopic residual stress can be thermally induced in metal AM by (a) differential heating of the solid and (b) differential cooling during and after solidification [67]. Residual stress tends to be compressive in the center of parts, tensile at the edge, and more highly concentrated near the substrate interface [68-71]. Residual stress is a concern because it can negatively affect the mechanical properties of as-fabricated parts or lead to geometrical distortions. The magnitude of residual stress and the ways to reduce it are process dependent. A lot of studies have been developed to measure residual stress in metal AM parts and are discussed in related papers and reports [68-79].

2.2.5 Post-processing

In metal AM technology, parts are not ready for end-use applications directly out of a machine. There are many steps that are typically used to prepare an as-fabricated part into an end-use part, including excess powder removal, build substrate and support structures removal, thermal treatments to improve mechanical behavior, and surface finishing to achieve desired geometrical tolerance and surface finish [24].

2.2.5.1 Powder, Support and Substrate Removal

After a part is done, excess powder, support structures and substrate material must be removed. Powder bed systems require powder to either be vacuumed from the part if loose

(SLM) or blasted off using loose, similar powder if sintered (EBM). Other systems may require machine cleanup. Support structures are usually used in powder bed techniques are must be mechanically removed by application of force or cutting. The build substrate is typically adhered to the fabricated part and must be cut-off using a saw or wire EDM [24].

2.2.5.2 Thermal Post-processing

Once the supports and substrate are removed, thermal post-processing may be applied to relieve residual stresses, close pores and/or improve mechanical performance of the material. As-fabricated parts usually require heat treatment to achieve the desired microstructure and mechanical properties desired for service. Standard treatment options for Ti6Al4V and Inconel 718 are given in Table 7. The various treatment options can affect grain size, grain orientation, precipitate phases, porosity and mechanical properties. Heating AM metal in a furnace to produce changes in microstructure is the main goal of thermal post-processing. Thermal post-processing of metal affects grain through recovery, recrystallization and growth. Microstructure evolution is modified by dissolution, precipitation and growth [24].

Table 7 – Common post-processing procedures for Ti6Al4V and Inconel 718 [24].

Treatment	Ti6Al4V	Inconel 718
Stress relief	120 min @ 700-730°C	30 min @ 982°C 90 ± 15 min @ 1065 ± 15°C
Hot isostatic pressure (HIP)	120 min @ 900°C, 900 MPa 180 ± 60 min @ 895-955°C, >100 MPa	240 min @ 1120°C, 200 MPa
Solution treat (ST)	Not typical	60 min @ 980°C
Aging	Not typical	480 min @ 720°C; Cool to 620°C; Hold @ 620°C for 18 hours total

2.2.5.2.1 Stress Relief

Stress relief involves recovery. Atomic diffusion increases at elevated temperatures, and atoms in regions of high stress can move to regions of lower stress, which results in the relief of internal strain energy. SLM and DMD parts are usually annealed to remove residual stress, commonly prior to substrate removal. Stress relief treatments must be performed at high enough temperature to allow atomic mobility but remain short enough in time to suppress grain recrystallization (unless desired) and growth (associated with strength loss) [24].

2.2.5.2.2 Recrystallization

Recrystallization may be desirable in metal AM to promote the formation of equiaxed microstructure from columnar microstructure. Research on iron [75] and Ti6Al4V additively manufactured [80, 81] has noted recrystallization of as-fabricated parts during annealing (no HIP). In these studies, residual stress is proposed as a likely driving force for this recrystallization (RX). More information about recrystallization can be found in other related reports and papers [82-84].

2.2.5.2.3 Hot Isostatic Pressing (HIP)

HIP can be used to close internal pores and cracks in metal AM parts. Internal pores, or "closed" pores, are surrounded by material in the center of the sample. If these pores are formed at the surface they are called "open" pores. Open pores are a problem for post-processing operations, as they allow deeper infiltration into material from air during high heat cycles. Internal cracks may also be closed by HIP [60]. The use of HIP can significantly change the grain structure of AM parts. Recent studies proved that standard HIP cycles may yield vary large grains [85]. Additionally, Kim et al. [86] studied the influence of HIP conditions on microstructure and mechanical properties of Ti6Al4V alloy parts and found that the microstructure of the specimens was strongly dependent on the beta-transus temperatures. Therefore, the characterization of as-built microstructure is critical to applying the correct HIP post-processing of AM parts. On the other hand, the homogenization of AM alloys prior to HIP or other post-processing can lead to standard post-processing procedures that are independent of processing conditions. Most metal AM post-processing operations are performed this way [24].

2.2.5.2.4 Solution Treat and Aging

Solution treat (ST) can be used to dissolve unwanted phases for precipitate hardened materials and aging can be used to form and grow precipitate phases. Sometimes, these processes are performed sequentially and referred to as solution treated and aged (STA). The ST temperature should be above the solvus temperature at which all undesired phases will dissolve. Regarding time, this should be long enough to dissolve precipitates but short enough to limit grain growth. Once the material is solutionized to form a solid a solution the matrix is essentially "reset". The purpose of aging is to precipitate harden a material [24].

2.2.5.3 Surface Finishing

AM parts are usually machined to achieve a smooth surface finish. As-fabricated parts typically have high surface roughness, as discussed in topic 2.2.4.1. The most common way to machine AM parts is to use CNC mills associated with subtractive manufacturing. Simple rotary-tool polishing or grinding with a belt sander can also be used for some applications, but they do not meet the standards required for high-quality parts. Chemical polishing and electrochemical polishing have also been explored [24, 87].

Since most of the parts go underneath thermal post-processing, oxidation of surface can occur, as seen in Figure 15a. If open pores are present, oxidation can extend into the interior of the part, as seen in Figure 15b. This open pores can and must be avoided since they cannot get be removed by surface machining [24].

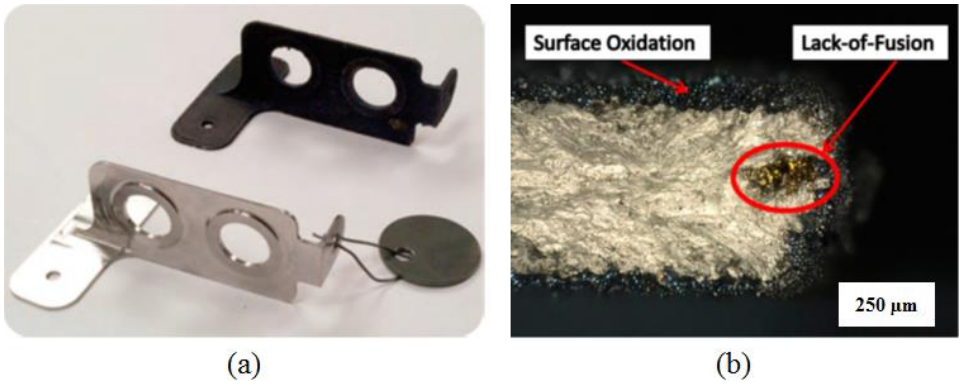

Figure 15 – Post-HIP effects on metal AM parts: (a) Ti6Al4V bracket before (top) and after (down) machining [88]; (b) Thin-wall EBM fracture surface of Inconel 718 from post-HIP sample with notable change in surface oxidation and oxidation of an open pore caused by lack-of-fusion near the edge [24].

2.3 Additive Manufacturing of Ti6Al4V

2.3.1 Introduction

The urge in aerospace industry to reduce cost and time of manufacturing of flight components without compromising safety and performance stimulates the search of novel manufacturing routes. AM's ability to manage small batches, create complex designs and fabricate lightweight but strong structures makes it a natural fit, especially for titanium alloys, which are hard to produce by traditional processes such as forging, machining and casting and for which the waste of material also makes it very expensive.

Titanium alloys are extensively used in aerospace applications such as components in aero-engines and space shuttles, mainly due to their high strength-to-weight ratio, as well as good creep resistance at high temperatures. It has also to found application in the biomedical and chemical industries because of its high corrosion resistance, low Young's modulus, and good biocompability. Table 8 presents the some of the basic characteristics of titanium compared to other structural metals.

Table 8 – Some important characteristics of titanium compared to other structural metals [89].

	Ti	Fe	Ni	Al
Melting Temperature (°C)	1670	1538	1455	660
Allotropic Transformation (°C)	$\beta \overset{882}{\longrightarrow} \alpha$	$\gamma \overset{912}{\longrightarrow} \alpha$	-	-
Crystal Structure	bcc → hex	fcc → bcc	fcc	fcc
Room Temperature E (GPa)	115	215	200	72
Yield Stress Level (MPa)	1000	1000	1000	500
Density (g/cm^3)	4.5	7.9	8.9	2.7
Comparative Corrosion Resistance	Very High	Low	Medium	High
Comparative Reactivity with Oxygen	Very High	Low	Low	High
Comparative Price of Metal	Very High	Low	High	Medium

Due to its high cost, titanium is limited to certain niche application areas. This high price is mainly a result of the high reactivity of titanium with oxygen, especially at high temperatures. Oxygen diffusion can occur at high temperatures, which can cause embrittlement. For this reason, when titanium is brought to high temperatures, for example during metal processing or

welding, an inert gas environment/vacuum is necessary to prevent reactivity. Since special care must be taken during processing, production costs are increased [89].

Pure titanium undergoes an allotropic transformation from body-centered cubic crystal structure (β phase) at higher temperatures to hexagonal closed-packed crystal structure (α phase) at lower temperatures – see Figure 16. The exact transformation temperature is strongly influenced by interstitial and substitutional elements and therefore depends on the purity of the metal. Alloying elements in titanium are usually classified into α or β stabilizers depending on whether they increase or decrease the α/β transformation temperature of 882°C of pure titanium. Figure 17 shows the most common alloying elements and their stabilizing effect. In alloys, the α phase and β phase regions are not adjacent as in pure titanium, but separated by a two phase α+β region whose width increases with increasing solute concentration. Therefore, titanium alloys are divided into three major groups, α alloys, β alloys and α+β alloys, depending on type and amount of alloying elements which decide the phases that are dominant at room temperature. α alloys are characterized by little response to heat treatment. α+β alloys form from fast cooling from the β phase field to room temperature; near α alloys are alloys that have less than 10 vol% of β phase. β alloys are less commonly used and formed when coupled with β stabilizers such as vanadium [89, 90].

The transformation of the bcc β phase to the hcp α phase in titanium alloys can occur by (a) diffusion controlled nucleation and growth process or (b) martensitically depending on cooling rate and alloy composition. When the cooling rate from the β phase field into the α+β phase field is sufficiently low, α phase forms by nucleation at β grain boundaries, leading to a continuous α layer along β grain boundaries. As the metal is cooled further α plates nucleate either at the interface of the continuous α layer or at the β grain boundary and grow into the β grain as parallel plates (called α colonies). The resulting microstructure is a fully lamellar microstructure with α and β lamellae. With increased cooling rate the size of α plates and α colonies become smaller, leading to a unique microstructure called “basket weave” structure or Widmanstätten structure. The martensite transformation results in a hexagonal crystal (HC) phase designated α’ and is observed in two morphologies: (a) massive (or lath) martensite, which consists of large irregular regions of small α colonies; and (b) “acicular” martensite, which an intimate mixture of individual α plates [89].

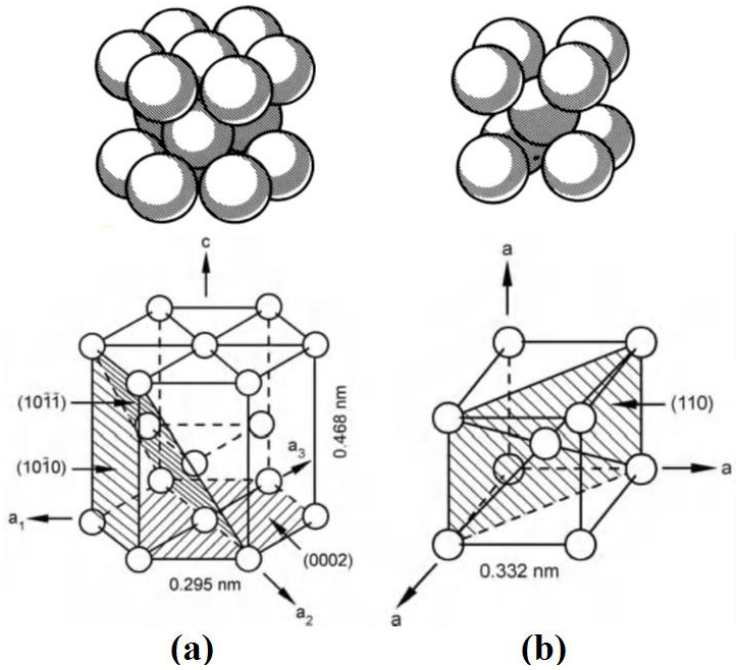

Figure 16 – Titanium crystal structures; (a) hexagonal close-packed (hcp), α phase; (b) body-centered cubic (bcc), β phase. Adapted from [89].

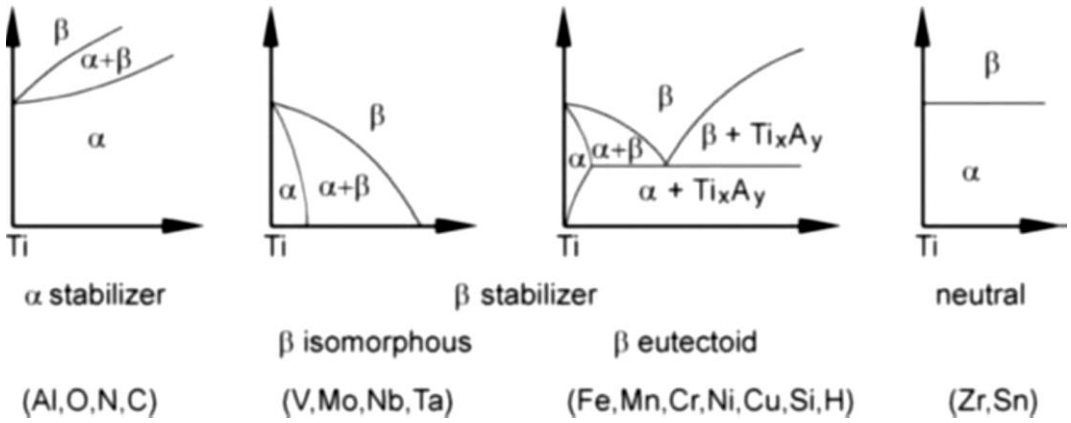

Figure 17 – Effect of alloying elements on phase diagrams of titanium alloys (schematically) [89].

2.3.2 Titanium Ti6Al4V

Among titanium alloys, the Ti6Al4V, also known as Ti64, is the most widespread– >60% of all titanium alloys produced in USA and EU [91]. Ti64 is a two phase (α+β) alloy, with 6 wt% aluminum and 4 wt% vanadium – see Table 9. The addition of aluminum is correlated with an increase of mechanical resistance and a decrease of ductility, whereas the vanadium increases elongation at room temperature and decreases the resistance to oxidation. This leads to an alloy with exceptional good balance of strength, ductility, fatigue, and fracture properties but can be used only up to temperatures of about 300°C. The ELI version of this popular alloy has especially high fracture toughness values and excellent damage tolerance properties [89, 92].

Table 9 – Chemical Composition of Ti6Al4V alloy [93].

Element	Ti6Al4V (wt %)		Ti6Al4V ELI (wt %)	
	Min.	Max.	Min.	Max.
Al	5.5	6.75	5.5	6.5
V	3.5	4.5	3.5	4.5
N	–	0.05	–	0.03
C	–	0.08	–	0.08
O	–	0.20	–	0.13
Fe	–	0.40	–	0.25
H	–	0.015	–	0.0125
Ti	Balanced		Balanced	

2.3.2.1 Phase Diagram

Figure 18 shows the binary Ti-Al phase diagram. For the aluminum level of 6% the α/β transformation temperature is increased to about 1000°C for the two phase region (α+β). However, for the case of multicomponent alloys such as Ti64, the binary phase can serve only as a qualitative guideline. Once the vanadium content on Ti64 cannot be neglected, a ternary phase diagram should be used. As vanadium works as a β stabilizer, the transus temperature is decreased from 1000ºC to about 995ºC, as it can be seen in Figure 19. The Ti64 alloys contains in equilibrium at 800 ºC about 15 vol% β phase, which explains the low service temperature typical of common α+β alloys, as opposite to "near α" alloys [89, 94].

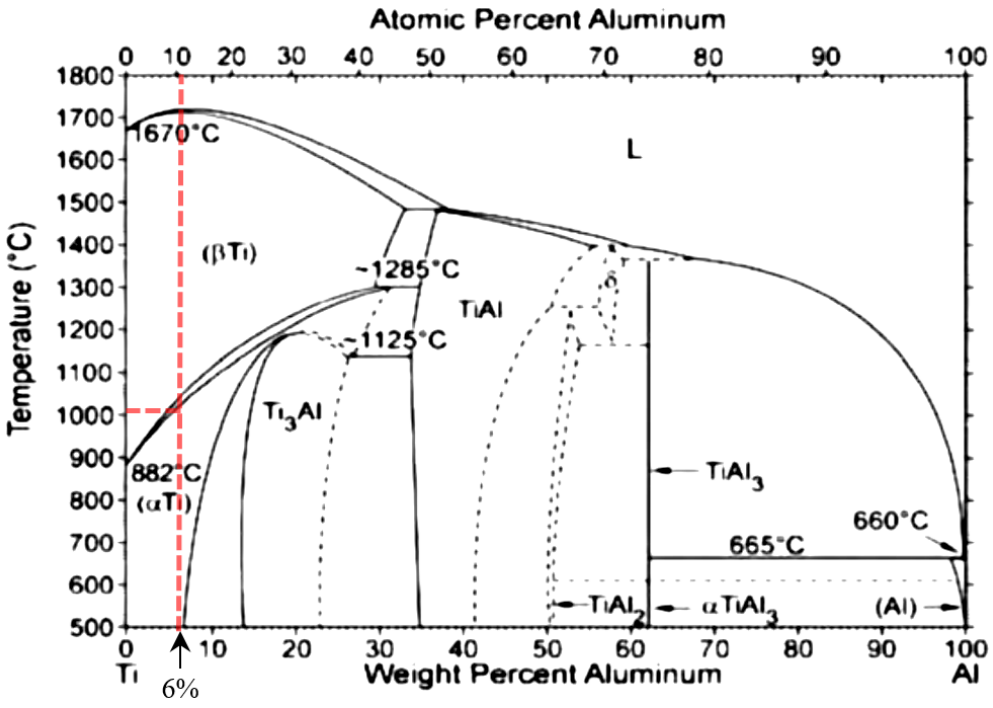

Figure 18 – Ti-Al phase diagram showing the Ti6Al4V aluminium content line. Adapted from [89].

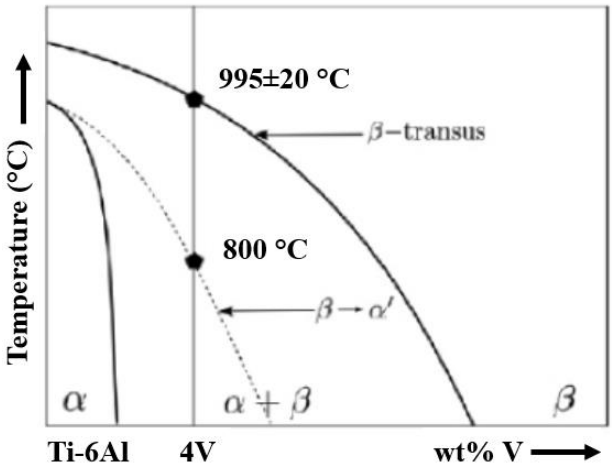

Figure 19 – Partial Ti-6Al-V phase diagram showing the Ti6Al4V composition line. Adapted from [94].

2.3.2.2 Development of Microstructure during Continuous Cooling

The microstructure and mechanical properties of titanium alloys are strongly dependent on alloy composition and cooling rate. One important characteristic of the alloy is a range of α+β→β phase transformation temperature that determines conditions of thermomechanical processing to develop the projected microstructure. This range of temperature is determined by the content of β stabilizer. Table 10 shows the start and end temperatures of α+β→β phase transformation for very low cooling/heating rates [91].

Table 10 – Start and end temperature of α+β→β phase transformation for Ti6AL4V ($v_c = v_h = 0.08$°C/s). Adapted from [91].

	Phase transformation	Temperature (°C)
Heating	$T^{ns}_{\alpha+\beta\rightarrow\beta}$	890
	$T^{ps}_{\alpha+\beta\rightarrow\beta}$	930
	$T^{f}_{\alpha+\beta\rightarrow\beta}$	985
Cooling	$T^{s}_{\beta\rightarrow\alpha+\beta}$	950
	$T^{f}_{\beta\rightarrow\alpha+\beta}$	870

ns – nucleation start; ps – precipitation start; s – start; f - finish

Phase composition of titanium alloys after cooling from β phase range is controlled by cooling rate. Figure 20 shows the CCT (Continuous Cooling Transformation) diagram for Ti64, from which the values on Table 11 were obtained. The type of microstructures obtained from continuous (see Figure 21) is also stated in Table 11. It is worth mentioning that other microstructures can be obtained for Ti64 by recrystallization, such as the bi-modal microstructure or fully equiaxed microstructure [89].

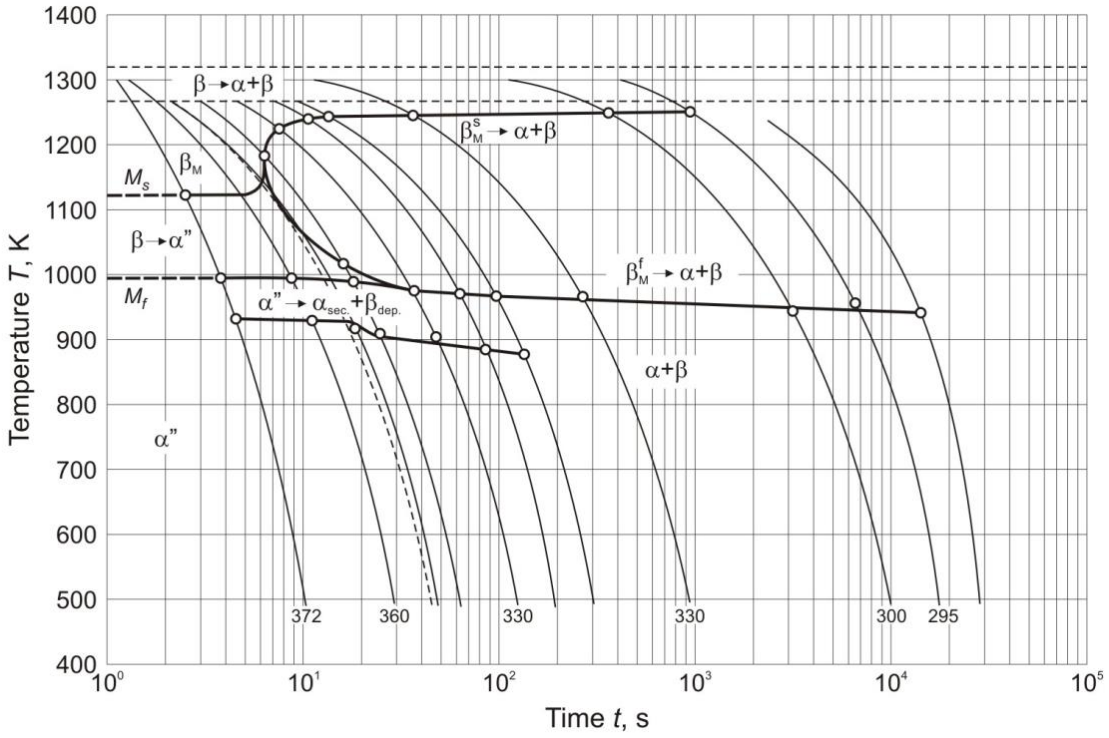

Figure 20 – CCT diagram for Ti6Al4V [91].

Table 11 – Phase composition and microstructure of T6Al4V after controlled cooling from the β phase range. Adapted from [91].

Cooling rate (°C/s)		Phase composition	Type of microstructure
Min	Max		
0.004	1.2	α + β	Lamellar microstructure
1.2	9	α + α'(α'') + β	Widmanstätten or "basket weave" microstructure
18	–	α'(α'') + β	Martensitic microstructure

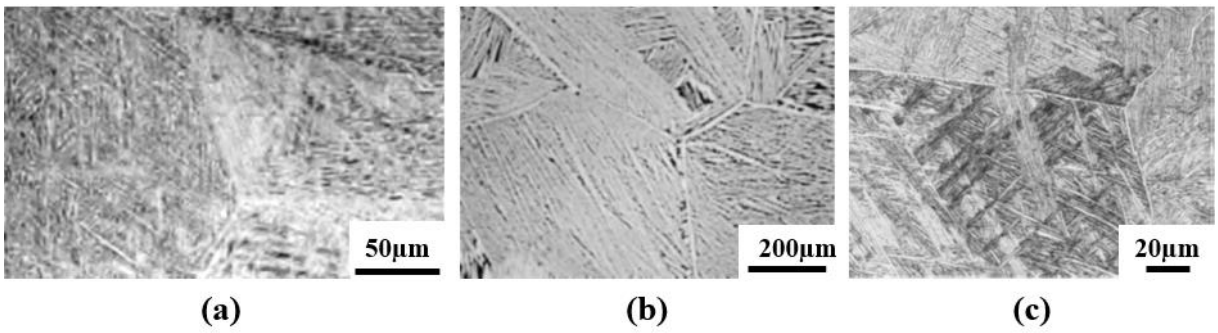

Figure 21 – Types of microstructures obtained from continuous cooling of Ti6Al4V: (a) "Acicular" martensitic microstructure; (b) Lamellar α+β microstructure (Source [89]); (c) Widmanstätten or "basket weave" microstructure (Source [91]).

2.3.2.3 Microstructure and Mechanical Properties

Being an α+β alloy, the mechanical properties of Ti64 can be adjusted to suit the requirements for a particular application by heat treatment, which is used to adjust the microstructure. Therefore, the mechanical properties are directly related to microstructure features. A qualitative summary of the basic microstructure/properties correlation is shown in Table 12. The qualitative trends (+, 0, –) point out the influence of a microstructural feature on a specific mechanical property. In the case of tensile properties, yield stress and ductility are used, whereas fatigue properties are measured by high cycle fatigue HCF (resistance to crack nucleation) and crack propagation. The fracture toughness is also evaluated [89-91].

Table 12 – Qualitative correlation between important microstructural features and mechanical properties. Adapted from [89].

	$\sigma_{0.2}$	ε_F	HCF	Microcracks	Macrocracks	Fracture toughness
Small α colonies/lamellae	+	+	+	+	–	–
Large α_p volume fraction	–	–	+	–	–	–
Texture: Stress || c-Axis	+	0	+ Vac – Air	0 Vac – Air	0 Vac – Air	+

For lamellar microstructures, the thickness of α lamellae and diameter of their colonies have the most significant influence. Refinement of the microstructure leads to higher yield stress and ductility, as well the microcrack propagation and crack nucleation. However the increase of yield stress is moderate unless martensitic phase is present, which increases with higher cooling rates. The macrocrack propagation and fracture toughness are improved by a large α colony size, probably due to increased crack roughness and crack closure phenomena [89-91].

Another important parameter also shown to affect the mechanical properties for this alloy is the alloying element partitioning effect. This partitioning increases the volume fraction of primary (globular) α (α_p), which results in a better response to age hardening, having a negligible effect in strength, ductility, crack propagation and fracture toughness [89-91].

The mechanical properties of Ti64 are also affected by the texture of the α phase. The adaptation of properties for a given application requires good control of the induced texture. Albrecht et al. [95] proved that the orientation of the basal plane with respect to the loading direction is of primary importance. When the loading direction was normal to the basal plane the yield stress was higher, whereas ductility was hardly affected by texture. Regarding HCF,

they found that highest fatigue life in vacuum is achieved for a loading direction normal to the basal plane, whereas in an atmosphere of air the fatigue life drops dramatically [89-91].

2.3.3 Published Mechanical Properties of Additively Manufactured Ti6Al4V

This section reviews published data on the mechanical properties of additively manufactured Ti64 parts. Summary tables for published mechanical properties will be grouped by the AM technique used and include values from hardness for as-built, heat-treated, and/or HIP conditions. The effects of test orientation and build direction on properties will be also documented, along with discussion of the potential sources (texture, microstructure changes, defects, etc.). Gaps and future research needs will be discussed as well.

As it was discussed before, the microstructure of titanium alloys are highly dependent on cooling rate. In metal AM, cooling rates during and after solidification are affected and controlled by different combinations of absorbed power and beam velocity (Figure 22). These variables, along with the thermal cycles that occur during such layered manufacturing and any post-processing affect the resulting microstructure. Unbalanced microstructures and defects can arise in as-built components, depending on the processing parameters and feedstock quality, whereas post-processing via heat-treatment/HIP can be applied to change this microstructural features and reduce/eliminate defects. These changes affect both orientation dependence and magnitude of mechanical properties [96].

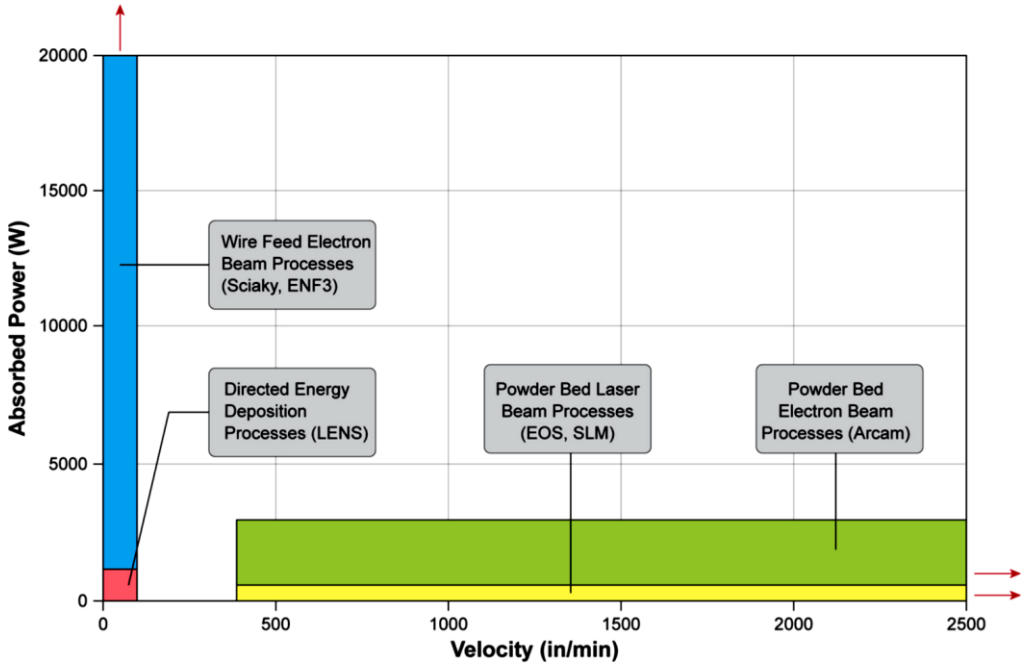

Figure 22 – Regimes of absorbed power and beam velocity in metal AM processes [96].

The influence test orientation and build direction on properties will be documented in a XYZ coordinate system defined by ASTM [97] – Figure 23. In this terminology, Z is the build

direction, whereas X is parallel to the front of the machine. For rectangular and nonsymmetrical specimens three letters are required, while for cylindrical specimens only one letter is enough.

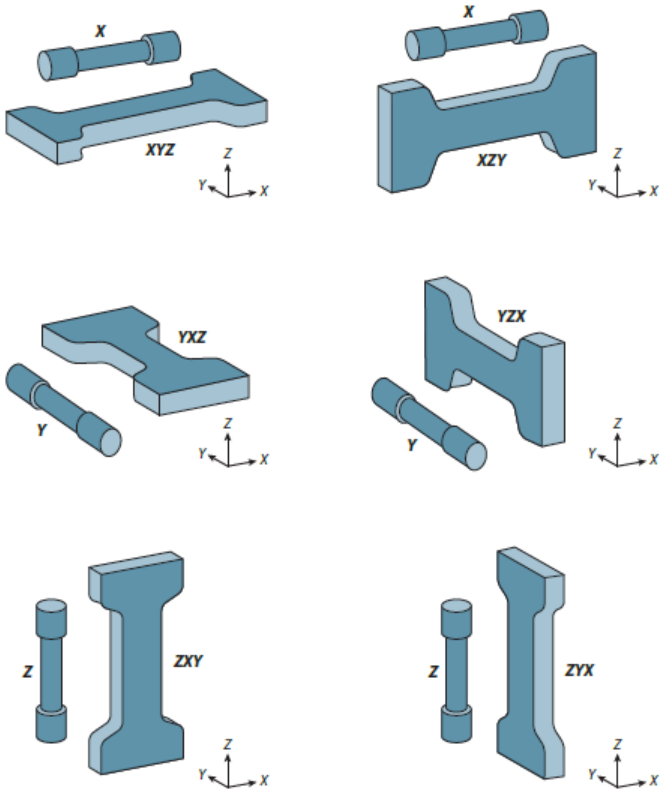

Figure 23 – Orientation for AM coordinate system and test methodology [97].

Table 13, Table 14 and Table 15 present published tensile properties and hardness data for TI64 produced via EBM, laser-based power bed and DED systems, respectively; it also provides the machine type and powder (conventional vs ELI), specimen orientation (S.O.), condition of material testing. Once the specimen gauge length varies between different investigations, the elongation to failure is hard to compare directly. However, the published values reveal an orientation-dependence for both yield strength, UTS and elongation to failure, that are also affect by heat-treatment and/or HIP. It appears also that machine type affect the reported properties, which proves that processing parameters affect mechanical properties. Moreover, the reported properties for all the conditions are often similar to and superior to those reported for conventional manufacturing of Ti64 [16], as it can be seen in Figure 24. The sources of orientation-dependent tensile property differences is starting to receive additional attention from AM community [98, 99]. The variance of properties can be explained by orientation-dependent differences in microstructure, texture, and defects, which are more influent in the fracture-critical properties (HCF, fatigue crack growth and fracture toughness). Post-processing (e.g. heat treatment and/or HIP) can be used to produce more desirable microstructures and reduce/eliminate defects (lack of fusion, isolated porosity, etc.).

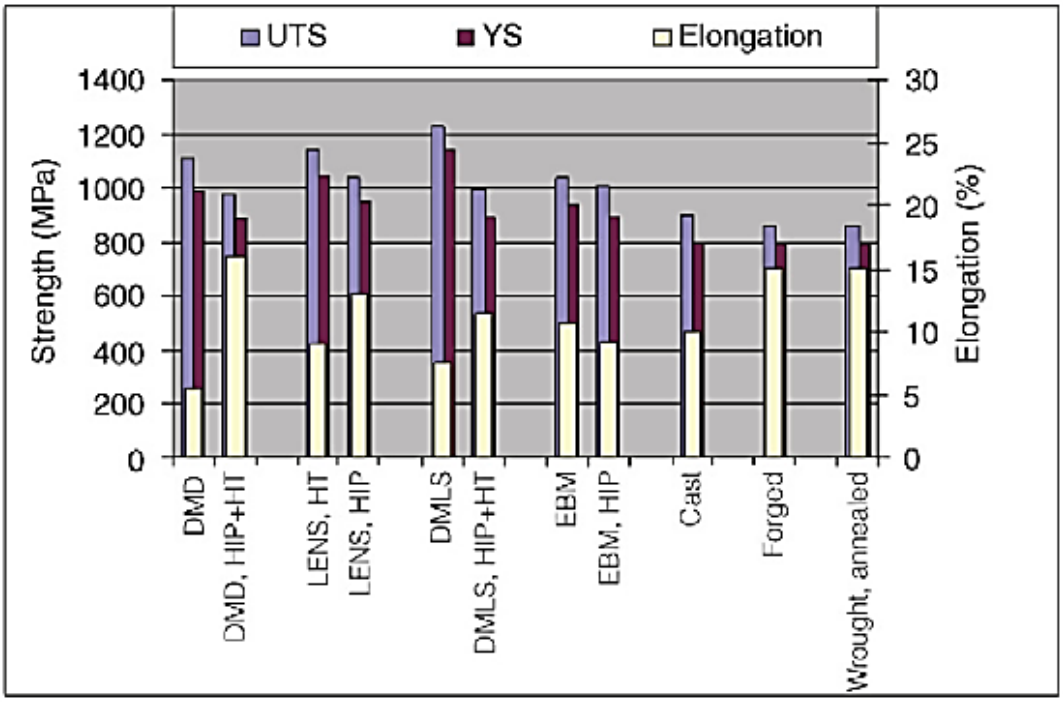

Figure 24 – Tensile strength, yield strength and elongation of Ti6Al4V alloy built using various metal AM processes and comparison with traditional manufacturing processes [100].

EBM process typically produces α+β lamellar microstructures with prior β grain sizes that can be affected or controlled by the combinations of P-V utilized in the process – see Figure 22. This is due to the use of preheated powder beds in the EBM process, which reduces the cooling rate during and after processing. It also leads to lower levels of residual stress in EBM materials in the as-built condition, compared to layer-based processes that do not use preheat – faster cooling rates produce highly nonequilibrium microstructures, such as martensite, and higher levels of residual stress, which requires post-processing. On the other hand, the chemistry control in EBM process can become an issue in Ti64 due to the preferential loss of aluminum during EBM of powders in vacuum. In laser-based powder bed systems, highly nonequilibrium microstructures (e.g. martensite), along with significant residual stresses that increase strength and decrease elongation to failure, are possible in as-built Ti64. As mentioned before, post-processing (e.g. stress relief) has been used to increase elongation while decreasing strength [101-107].

For DED processes, the combinations of P-V (Figure 22) usually produce α+β lamellar microstructures with prior β grain sizes larger than those obtained by laser-based powder bed systems, due to slower cooling rates typically present in DED [101-104, 108, 109].

Table 13 – Summary of EBM AM Ti6Al4V tensile properties.

Machine type	Condition	S.O.	E (GPa)	$\sigma_{0.2}$ (MPa)	UTS (MPa)	ε_F (%)	Hardness (HV)	Ref.
ARCAM	Heat treated	ZX	NA	869 ± 7	965 ± 5	6 ± 0	NA	[110]
ARCAM A1	As-built	XY ZX	NA	783 ± 15 812 ± 12	833 ± 22 851 ± 19	2.7 ± 0.4 3.6 ± 0.9	NA NA	[111]
ARCAM	As-built HIP	XY Z XY Z	NA	870 ± 8.1 879 ± 12.5 866 ± 6.4 868 ± 2.9	971 ± 3.1 953 ± 8.8 959 ± 8.2 942 ± 2.6	12.1 ± 0.9 13.8 ± 0.9 13.6 ± 0.6 12.9 ± 0.8	NA	[112]
ARCAM ELI	As-built HIP	XY Z XY Z	NA	817 ± 4.3 802 ± 7.9 814 ± 2.4 807 ± 8.4	918 ± 1.0 904 ± 6.0 916 ± 2.5 902 ± 8.7	12.6 ± 0.8 13.8 ± 0.9 13.6 ± 1.2 14.8 ± 0.5	NA	
ARCAM A2xx ELI	As-built	XY	NA	851.8 ± 5.8	964 ± 0.3	16.3 ± 0.8	NA	[113]
ARCAM A2 ELI	As-built HIP	Z Z	NA	928 ± 13.3 813 ± 14.3	1001 ± 14.8 908 ± 3.2	13.6 ± 1.4 17.7 ± 0.9	NA	[114]
ARCAM S12	As-built	XY	NA	975	1033	16.78	NA	[115]
ARCAM	As-built HIP	XY XY	NA	881 ± 12.5 876 ± 12.5	978 ± 11.5 978 ± 9.5	10.7 ± 1.5 13.5 ± 1.5	NA	[116]
ARCAM S12	As-built	XY Z	NA	982 ± 5.7 984 ± 8.5	1029 ± 7 1032 ± 12.9	12.2 ± 0.8 9 ± 2.9	372 ± 7.2 367 ± 8.3	[117]
ARCAM S400	As-built	XY ZX	NA	899 ± 4.7 869 ± 7.2	978 ± 3.2 928 ± 9.8	9.5 ± 1.2 9.9 ± 1.7	NA	[118]
ARCAM S400	As-built	XY Z	104 ± 2.3 101 ± 2.5	844 ± 21.6 782 ± 5.1	917 ± 30.5 842 ± 13.8	8.8 ± 1.4 9.9 ± 1.0	NA	[119]
ARCAM S400 ELI	As-built	Z	NA	1150	1200	16	380	[120]
ARCAM	As-built	NA	118 ± 5 117 ± 4	830 ± 5 795 ± 10	915 ± 10 870 ± 10	13.1 ± 0.4 13.7 ± 1.0	NA	[121]
ARCAM A2 ELI	As-built	Z	93 ± 2	735 ± 28	775 ± 26	2.3 ± 0.8	369 ± 2	[122]
ARCAM	As-built HIP	Z XY Z	NA	856 841 800	924 938 876	15 20 16	NA	[123]
ARCAM	As-built	NA	114 ± 6	1135 ± 12	NA	NA	NA	[124]
ARCAM S400	As-built	Z	109 ± 2.1	1098 ± 15	1237 ± 13	8.8 ± 0.6	NA	[125]
ARCAM	As-built	NA	128	880	930	>10	NA	[126]

Note: NA – Not available

Table 14 - Summary of laser-based powder bed systems AM Ti6Al4V tensile properties.

Machine type	Condition	S.O.	E (GPa)	$\sigma_{0.2}$ (MPa)	UTS (MPa)	ε_F (%)	Hardness	Ref.
EOS	As-built	XZY	91.8 ± 0.5	938 ± 7.7	1140 ± 5	NA	NA	[127]
	Stress relieved	XZY	98.2 ± 1.2	862 ± 3.1	936 ± 3.6			
	HIP	XZY	106.8 ± 1.3	835 ± 3.8	910 ± 2.9			
SLM	As-built	XY	NA	1093 ± 64	1279 ± 13	6 ± 0.7	NA	[128]
		ZX		1125 ± 22	1216 ± 8	6 ± 0.4		
	Stress relieved	XY		1145 ± 17	1187 ± 10	7 ± 2.7		
		ZX		1132 ± 13	1156 ± 13	8 ± 0.4		
	Heat treated	XY		973 ± 8	996 ± 10	3 ± 0.4		
		ZX		964 ± 7	998 ± 14	6 ± 2		
EOS M280	As-built	ZX	NA	1017 ± 7	1096 ± 7	12 ± 0.5	NA	[110]
SLM	As-built	NA	110	736	1051	11.9	360 HV	[129]
	HIP		115.4	885	973	19	351 HV	
	Heat treated		117.4	1051	1115	11.3	321 HV	
Renishaw MTT250	As-built	XY	NA	910 ± 9.9	1035 ± 29	3.3 ± 0.76	NA	[130]
SLM250	As-built	ZX	NA	NA	1134 ± 15.6	4 ± 1.2	NA	[131]
	HIP	ZX			1088 ± 26.3	13.8 ± 1.3		
	Heat treated	ZX			1228 ± 32.4	8 ± 1.5		
Renishaw AM250	As-built	XZ	115 ± 6	978 ± 5	1143 ± 6	11.8 ± 0.5	NA	[132]
		ZX	119 ± 7	967 ± 10	1117± 3	8.9 ± 0.4		
		XY	113 ± 5	1075 ± 25	1199 ± 49	7.6 ± 0.5		
	Stress relieved	XZ	113 ± 9	958 ± 6	1057 ± 8	12.4 ± 0.7		
		ZX	117 ± 6	937 ± 9	1052 ± 11	9.6 ± 0.9		
		XY	112 ± 6	974 ± 7	1065 ± 21	7.0 ± 0.5		
SLM250	As-built	ZX	NA	1008	1080	1.6	NA	[133]
	HIP	ZX		962	1080	5		
	Heat treated	ZX		912	1005	8.3		
Realizer	As-built	ZX	119 ± 7	967 ± 10	117 ± 3	8.9 ± 0.4	NA	[134]
EOS M270	As-built	ZX	NA	1143 ± 30	1219 ± 20	4.89 ± 0.6	NA	[118]
		XY		1195 ± 19	1269 ± 9	5 ± 0.5		
SLM	As-built	XY	109.2 ± 3.1	1110 ± 9	1267 ± 5	7.28 ± 1.12	NA	[135]
EOS M270	As-built	NA	110 ± 5	990 ± 5	1095 ± 10	8.1 ± 0.3	NA	[136]
	Heat treated		NA	1040 ± 10	1140 ± 10	8.2 ± 0.3		
EOSM270	As-built	ZX	111	1120	1257	8.0	37 HRC	[125]
EOS M27	As-built	Z	NA	1333	1407	4.54	NA	[16]
SLM	As-built	NA	94	1125	1250	6	NA	[137]

Machine type	Condition	S.O.	E (GPa)	$\sigma_{0.2}$ (MPa)	UTS (MPa)	ε_F (%)	Hardness	Ref.
SLM (Trumpf)	As-built	XY	105 ± 5	1137 ± 20	1206 ± 8	7.6 ± 2	NA	[138]
		ZX	102 ± 5	962 ± 47	1166 ± 25	1.7 ± 0.3		
	Heat treated	XY	103 ± 11	944 ± 8	1036 ± 30	8.5 ± 1		
		ZX	98 ± 3	925 ± 14	1040 ± 40	7.5 ± 2		
Renishaw MTT	As-built	X	NA	1166 ± 6	1321 ± 6	2.0 ± 0.7	NA	[139]
DLF	As-built	X	118 ± 2.3	1100 ± 12	1211 ± 31	6.5 ± 0.6	NA	[140]
Concept Laser M2	As-built	X	NA	1070 ± 50	1250 ± 50	5.5 ± 1	NA	[141]
		Z		1050 ± 40	1180 ± 30	8.5 ± 1.5		
EOS M280	As-built	X/Y	NA	1109	1172	8	391	[35]
SLM	As-built	X/Y	NA	858	937	8	393	
		Z		1100	1209	11	398	

Note: NA – Not available

Table 15 – Summary of DED AM Ti6Al4V tensile properties.

Machine type	Condition	S.O.	E (GPa)	$\sigma_{0.2}$ (MPa)	UTS (MPa)	ε_F (%)	Hardness	Ref.
LENS (Optomec)	Stress relieved	X	116	1065	1109	4.9	NA	[142]
		Y	116	1066	1112	5.5		
		Z	112	832	832	0.8		
	HIP	X	118	946	1005	13.1		
		Y	118	952	1007	13.0		
		Z	114	899	1002	11.8		
DLD (Trumpf)	As built	X	NA	950 ± 2	1025 ± 10	12 ± 1	NA	[143]
		Z		950 ± 2	1025 ± 2	5 ± 1		
	HIP	NA		850 ± 2	920 ± 1	17 ± 2		
LMD	As-built	X	NA	976 ± 24	1099 ± 2	4.9 ± 0.1	NA	[144]
LSF	As-built	Z	NA	1070	1140	6	NA	[145]
LF	As-built	X	NA	892 ± 10	911 ± 10	6.4 ± 0.6	NA	[146]
		Z		522	797 ± 27	1.7 ± 0.3		
	As-built (machined)	X		984 ± 25	1069 ± 19	5.4 ± 1		
		Z		958 ± 14	1026 ± 17	3.8 ± 0.9		
	Heat treated	X		681 ± 35	750 ± 20	4.8 ± 1.6		
		Z		637 ± 13	717 ± 12	3.4 ± 1.0		
	Heat treated (machined)	X		870 ± 37	953 ± 18	11.8 ± 1.3		
		Z		930 ± 15	942 ± 13	9.7 ± 2.2		
DMD	As-built	X	NA	1015 ± 19	1163 ± 22	4 ± 1	NA	[147]
	Heat treated	X		975 ± 15	1053 ± 18	7.5 ± 1		
IPG YLR	As-built	X	NA	960 ± 26	1063 ± 20	10.9 ± 1.4	NA	[148]
		Z		958 ± 19	1064 ± 26	14 ± 1		

Machine type	Condition	S.O.	E (GPa)	$\sigma_{0.2}$ (MPa)	UTS (MPa)	ε_F (%)	Hardness	Ref.
DLF	Heat treated	NA	NA	958	1027	6.2	NA	[149]
LENS	Heat treated	NA	NA	827 – 965	896 – 1000	1 – 16	NA	[150]
LENS (Optomec)	As-built (low power)	X	NA	1005	1103	4	NA	[151]
	Heat treated (low power)	X		1000	1073	9		
	As-built (high power)	X		990	1042	7		
	Heat treated (high power)	X		991	1044	10		
Laser forming	Heat treated	NA	NA	839	900	12.3	NA	[152]
LENS	As-built	Z	119	908	1038	3.8	NA	[153]
	Annealed	Z	112	959	1049	3.7		
	Heat treated	Z	118	957	1097	3.4		

Note: NA – Not available

Optical micrographs for SLM and EBM are given in Figure 25 and Figure 26, respectively. The materials processed by these two techniques undergo very high cooling rates. Figure 25 shows the expected martensitic (α') microstructure for SLM Ti64. Martensitic laths formed from the prior β grain boundaries and fill the columnar grains. In EBM-produced Ti64, the microstructure is mainly composed by an α phase and a small amount of β within the β prior β columnar grains oriented along the build direction. The α phase has a lamellar morphology with α surrounding the a lamellae boundary. The α lamellae are arranged in a basket weave structure with different sizes and orientations, and forms α colonies within the columnar grains (Figure 26). Although SLM and EBM techniques produce different microstructures, both cases prior β columnar grain boundaries are clearly visible, which implies that the difference in microstructure is because of the differences in cooling rate. Moreover, both microstructures from SLM and EBM-produced Ti64 differ from conventional wrought materials as shown in Figure 27. In this case the microstructure is composed of both α and β grains oriented in the rolling direction [118].

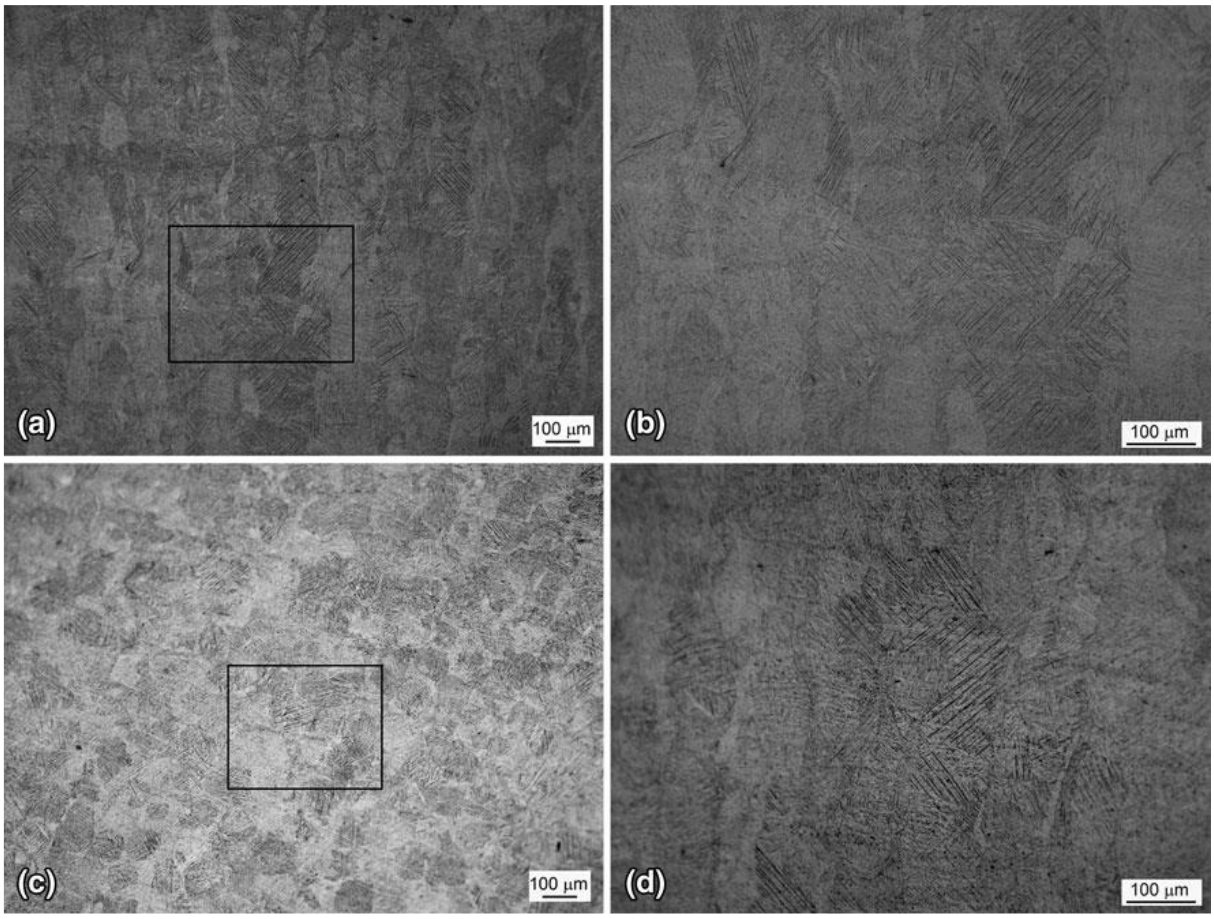

Figure 25 - Optical micrographs of SLM-produced Ti64 samples: (a) Longitudinal cross-section showing columnar grains; (b) High magnification longitudinal cross-section image showing fine martensitic laths [from the boxed region in (a)]; (c) Transverse cross-section showing bundles of columnar grains. (d) High magnification transverse cross-section image showing fine martensitic laths in a columnar grain [from the boxed region in (c)] [118].

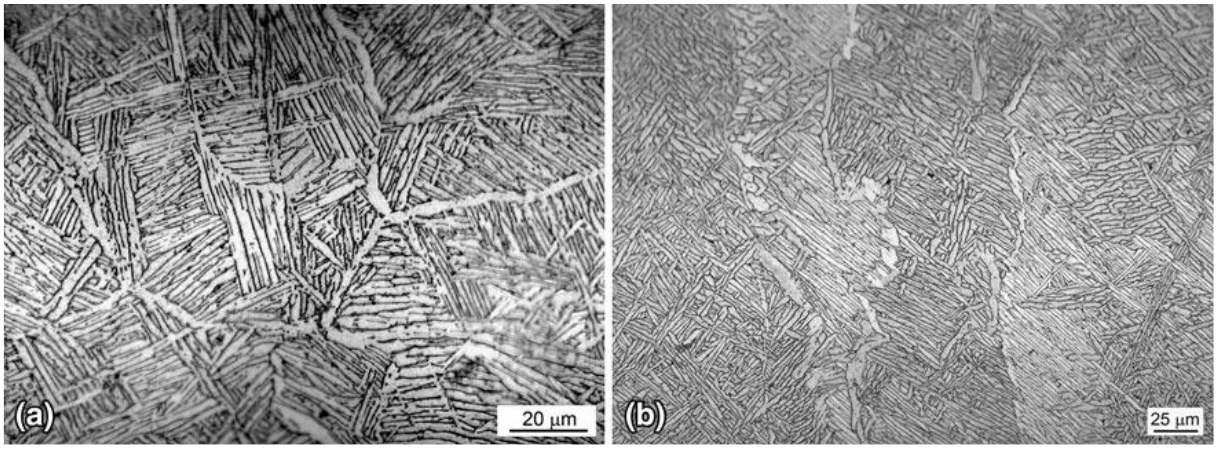

Figure 26 - Optical micrograph of EBM-produced Ti64 samples: (a) Transverse cross-section; (b) Longitudinal cross-section [118].

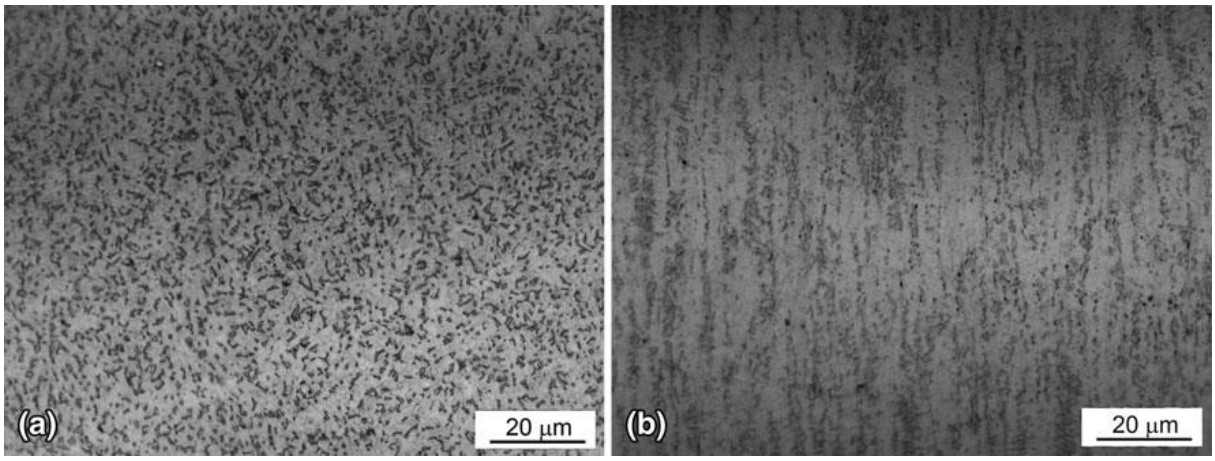

Figure 27 - Optical micrograph of wrought Ti64 (annealed and rolled): (a) Transverse cross-section; (b) Longitudinal cross-section [118].

2.3.4 Gaps and Future Research Needs

Figure 28 presents a summary of the range of properties usually considered in the mechanical characterization of structural materials depending on their specific application. Despite the extent of published mechanical properties has not covered the whole range of those shown in Figure 28, some of them have reported to approach, or even exceed, properties obtained with conventional processes, such as casting, extrusion, and forging. However, relatively few published data exist on standard testing methodologies, and little to no publish work exist for low cycle fatigue, fatigue crack growth, fracture toughness, impact, creep, creep fatigue, multiaxial testing, and environmental effects. Moreover, the variance of properties (controlled by microstructure, residual stresses, defects, etc.) within and between builds in one machine and across different machines and techniques, along with the presence of process-induced defects and location/orientation-dependence, limits the use of metal AM for fracture-critical applications. An understanding of the influence of microstructural features on properties, as well as the source(s), detection and elimination of process-induced defects, are some of the goals that can accomplish the metal AM-enabled "third industrial revolution" [154].

Recently, the NSWCCD-61 organization (Naval Surface Warfare Center, Carderock Division) [155] has proposed one approach and that is summarized in Figure 29. It shows some of the various challenges that can be address, such as lack of computationally efficient tools, lack of in-situ monitoring systems, lack of materials/testing standards, feedstock and recyclability/reusability issues, surface roughness and residual stress control and process feedback. Addressing these challenges in a cost-effective manner will be the path to follow for the next 5-10 years.

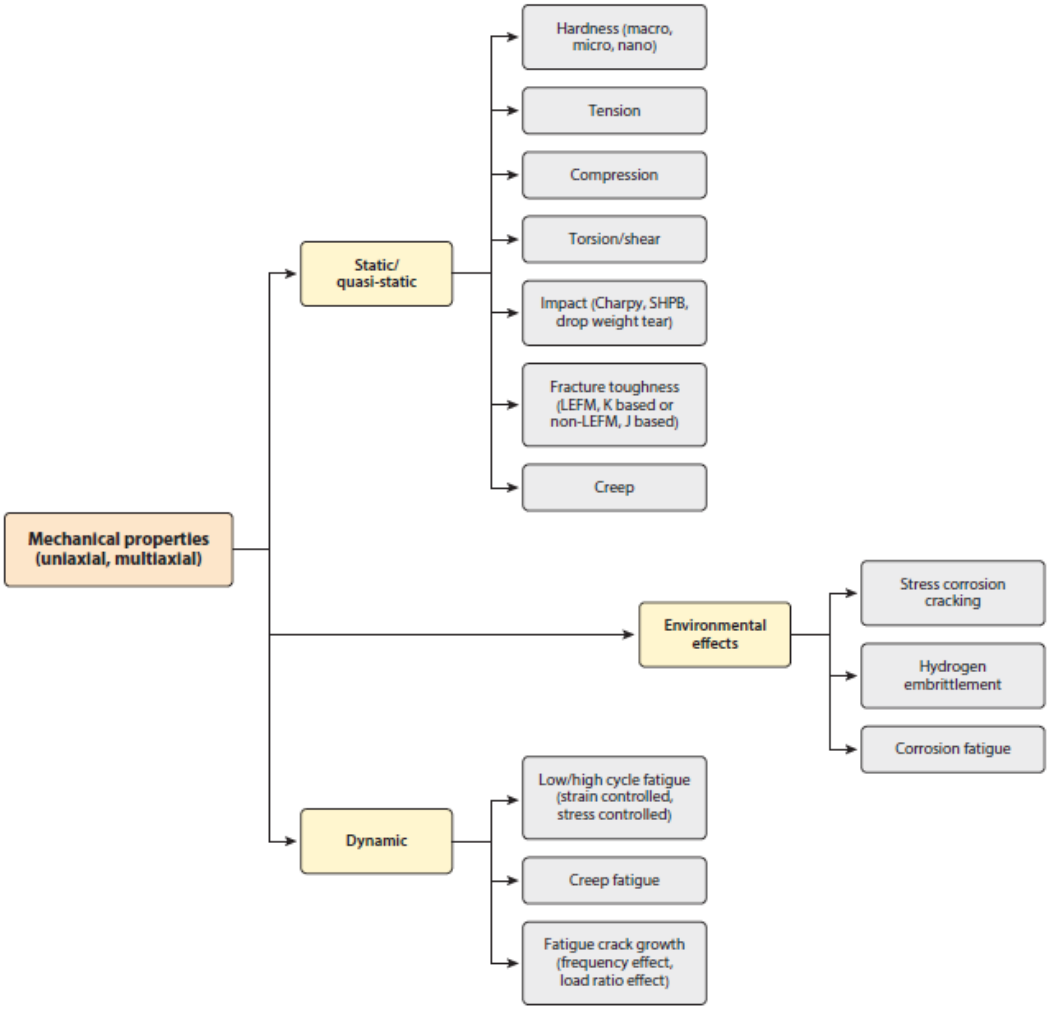

Figure 28 – Range of mechanical properties generated for structural materials; the specific properties are designed for a specific application [154].

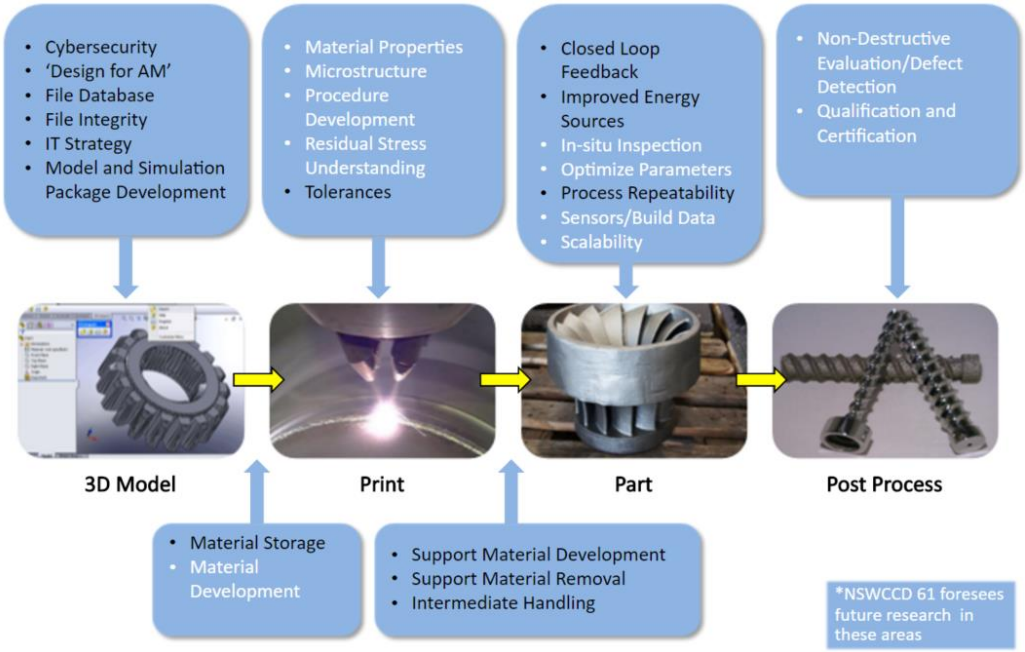

Figure 29 - AM technology gaps and Research and Development opportunities identified by the NSWCCD-61 organization [155].

3 Methods and Materials

3.1 Introduction

The following chapter present relevant procedures used in this thesis for specimen preparation, measurement, and analysis. The material examined will be presented, including the AM process and post-processing. An insight of microsample mechanical testing technique will be provided. There, the preparation of microsamples will be discussed including specimen extraction, as well as sample polishing and etching. The specifics of the microsample testing system will also be discussed. Finally, the digital image correlation (DIC) procedure will be outlined, including relevant parameters used for the analysis.

3.2 Additively Manufactured Ti6Al4V

The AM Ti64 material that will be examined in this work was received from NAS Pax River. The material received was made in an EOS M280 and then HIPed.

EOS M 280 (Figure 30 is based on the innovative DMLS (Direct Metal Laser Sintering) system by EOS. It produces components by means of Additive Manufacturing – fully automatically, without tools and based directly on three-dimensional CAD design data. For this purpose it is equipped with a 200 W or 400 W fiber laser which melts fine metal powder and builds up the product layer by layer [156]. Table 16 presents the EOS M280 machine technical data.

Figure 30 – EOS M280 system [156].

Table 16 – EOS M280 system data [156].

Technical Data	
Building volume (including building platform)	250 mm x 250 mm x 325 mm
Laser type	Yb-fiber laser, 200 W or 400 W (optional)
Precision optics	F-theta-lens, high-speed scanner
Scan speed	up to 7.0 m/s
Variable focus diameter	100 – 500 µm
Power supply	32 A
Power consumption	maximum 8.5 kW / typical 3.2 kW
Nitrogen generator	integrated
Compressed air supply	7000 hPa; 20 m^3/h
Dimensions (W x D x H)	
System	2200 mm x 1070 mm x 2290 mm
Recommended installation space	min. 4.8 m x 3.6 m x 2.9 m
Weight	approx. 1250 kg
Data preparation	
Software	EOS RP Tools; EOSTATE Magics RP (Materialize)
CAD interface	STL Optional; converter for all standard formats
Network	Ethernet

The HIP post-processing was chosen to close internal voids and cracks. Regarding the HIP parameters, as well as other processing parameters of the EOS M280 and powder dimensions, cannot be disclosed because they are proprietary. The material as-HIPed was then sliced into 1 mm thick plates with wire EDM of the bulk of the additively manufactured Ti64 block to characterize the material at the surface.

3.3 Microsample Mechanical Testing Technique

The ability to measure local properties can provide valuable insight into material behavior, particularly when inhomogeneous materials or microstructures are present or small amounts of material might only be available. Microscale-sample (microsample) characterization provides information that would otherwise be averaged or masked on the macroscale. Testing microsamples harvested from bulk materials can be difficult due to the sample preparation required. In addition, it is important to understand the local microstructure within the gage length of the sample. The microsample mechanical testing technique has been

proven to work well in characterizing a variety of materials such as thin films [157-160] or bulk, metal alloys [161-166].

3.3.1 Microsample Preparation

The microsamples are extracted directly from the AM Ti64 plate with a thickness of 1 mm. The microsample geometry used in this thesis is shown in Figure 31.

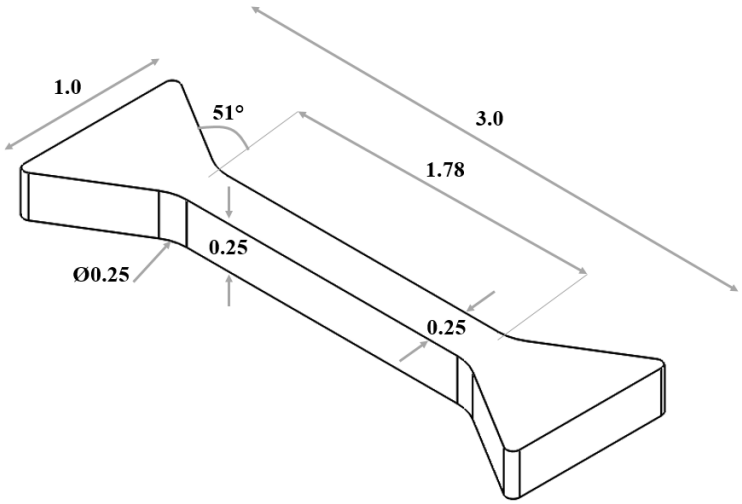

Figure 31 – Microsample geometry (units in mm) [167].

All samples were extracted using a Fanuc Alpha OiE wire electric discharge machine (EDM). The samples were machined using a finishing pass setting within the EDM which results in a slow, controlled cutting process with little damage to the material. Examples of cut samples are shown in Figure 32. After the samples are extracted they are polished to thickness using 180, 320, 400, 600, 800 and 1200 grit SiC paper, followed by a final polish using a 0.05 µm colloidal silica suspension. To prepare samples for microstructural observations before mechanical testing, the samples were polished by a vibratory polish using a 10:1 mixture of 0.05 µm colloidal silica and 30% hydrogen peroxide. The samples were then etched using Kroll's reagent for 60 seconds. Microsample measurements were made using an Olympus BX51.

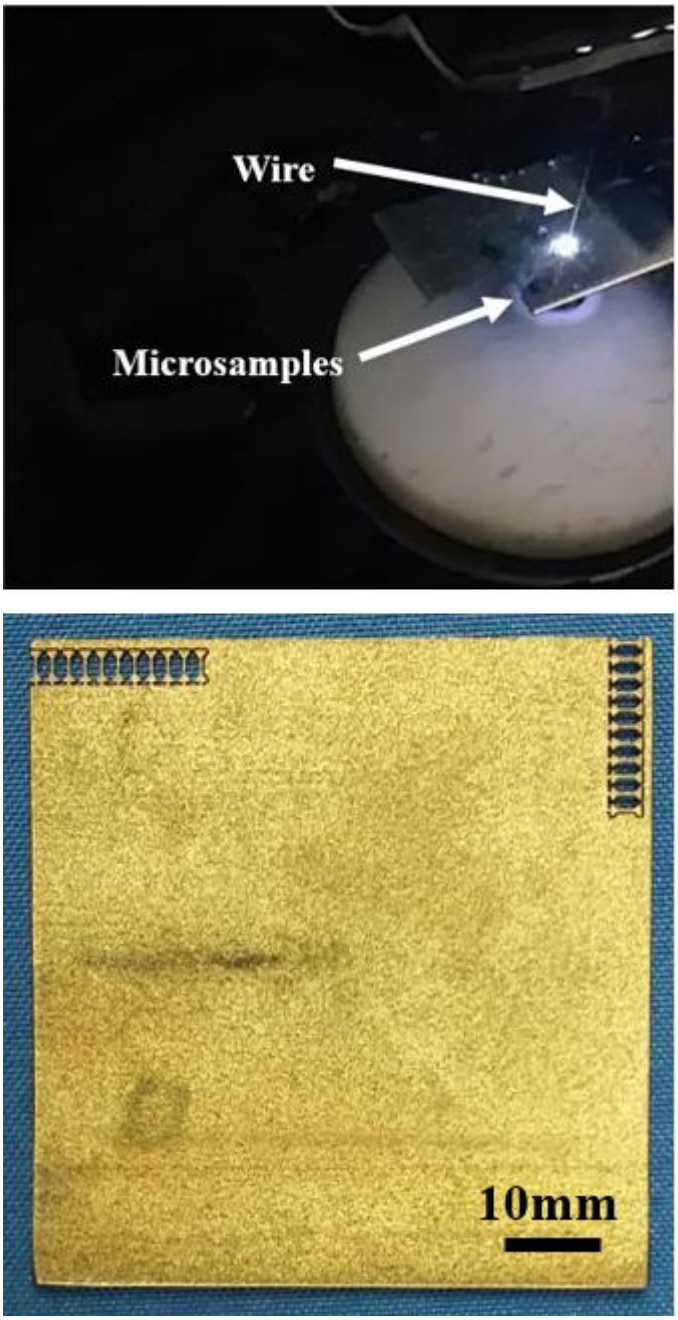

Figure 32 – Top: Wire EDM extracting samples; Bottom: samples extracted from AM Ti64 plate.

Regarding the microsamples orientation, these were machined such that the tensile axis was aligned along (a) the building direction and (b) transversal to building direction, as shown in Figure 33. Following the XYZ coordinate system defined by ASTM [97] – see Figure 23 – the specimens along the building direction would be designated ZXY/ZYX and the specimens transversal to building direction would be designated XZY/YZX. Nonetheless, in this work the samples along the building direction and transversal do building direction will be named d1 and d2, respectively.

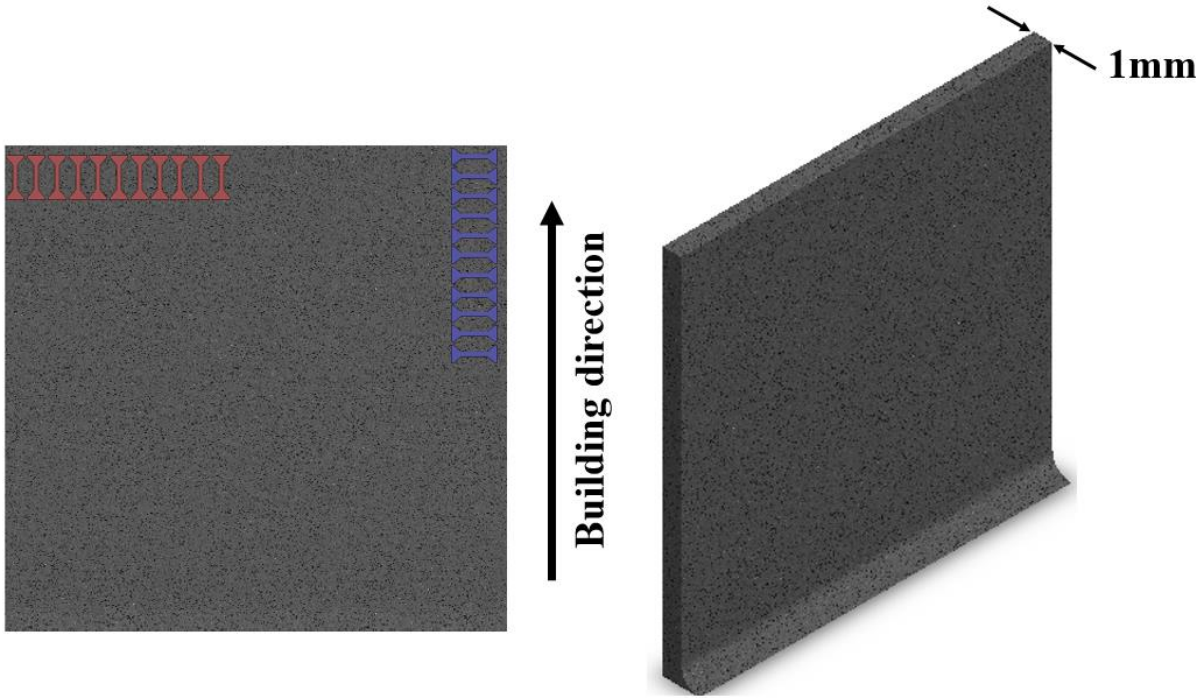

Figure 33 – Schematic of microsample's location cut from AM Ti6Al4V sample.

3.3.2 Microsample Testing System Design

The microsample testing system used in this thesis was developed by Salahudin Nimer under the scope of its doctoral program [167]. The scope of his work was to validate a microsample testing system capable of characterizing materials at temperatures up to 600 °C, utilizing digital image correlation (DIC) to measure response of samples that have a 3 mm x 1 mm footprint and a cross sectional gage area of 250 µm x 250 µm.

The elevated temperature system is shown in Figure 34. It shares many similarities with its room temperature counterpart [165, 166]. In this system, the load frame used a piezoelectric actuator producing a quasi-static strain rate of 10^{-4} sec^{-1}, as shown in Figure 34b. The actuator used in the system is an LTA-HL from Newport; the actuator specifications are shown in Table 17. This actuator produces an adequately high resolution step size for loading of the microsamples examined in this work. A load cell is placed in line between the actuator and a linear air bearing, which is used to minimize any friction during the test. The load cell range is tailored to achieve the highest resolution possible for the material being tested [167].

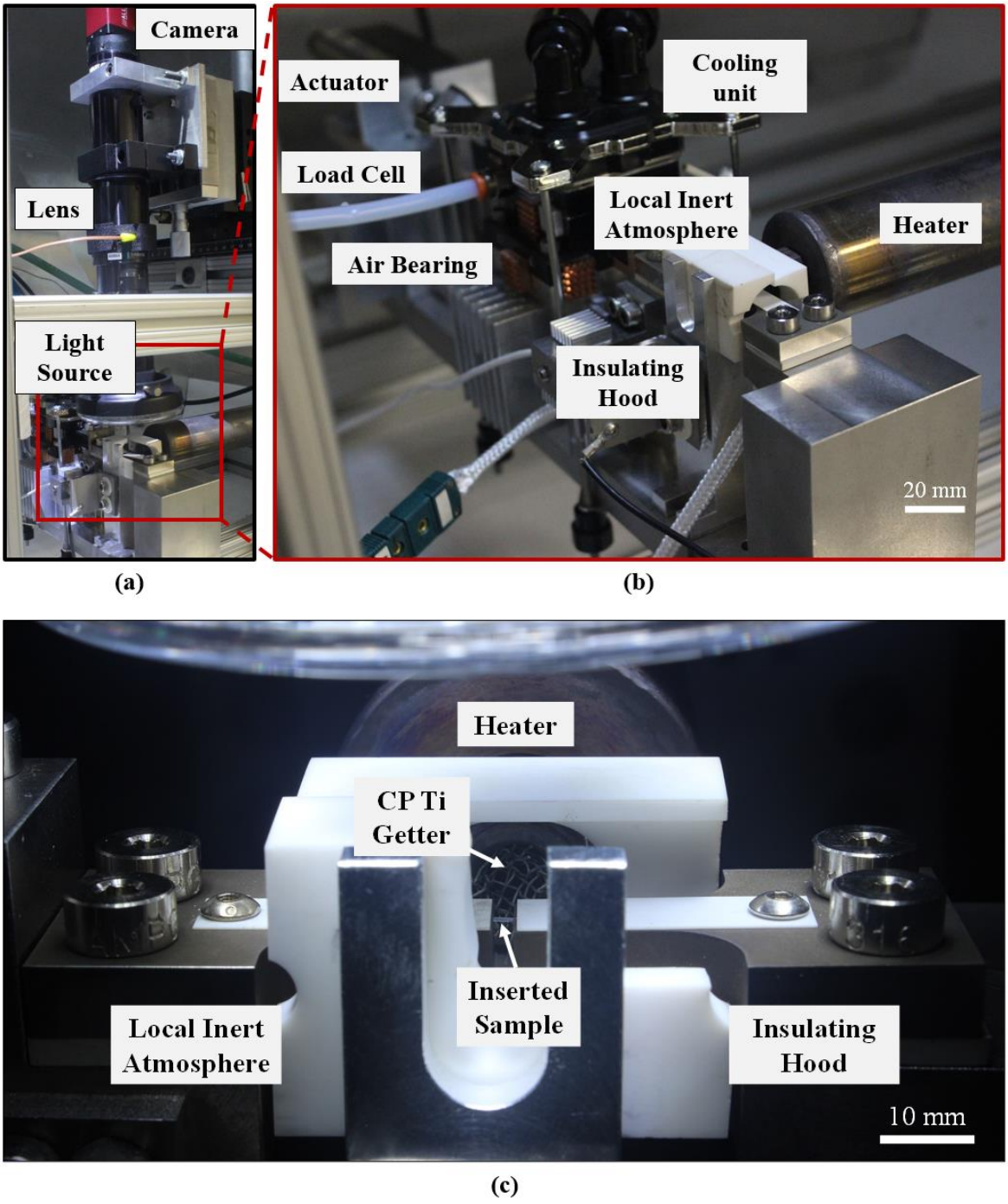

Figure 34 – Elevated temperature microsample testing system; (a) camera, lens and light source used for DIC measurement; (b) and (c) heating system and load frame [167].

Table 17 – LTA-HL Newport actuator specifications.

Maximum Speed	1 mm/s
Axial Load Capacity	
Push	120 N
Pull	120 N
Stroke	25 mm

3.3.3 Strain Measurement

In this system, a method to perform DIC analysis of microsamples was developed. Before the samples were tested they were coated with a white and black high temperature paint (Rust-Oleum high heat enamel). The white paint was used for the background followed by a black paint for the speckle pattern that was diluted with acetone in a 1:1 ratio by weight. The black speckle pattern (Figure 35) was applied using an airbrush that produces speckles that are on average 10 μm in diameter [167]. The samples were illuminated using a white LED source and imaged with a lens and camera.

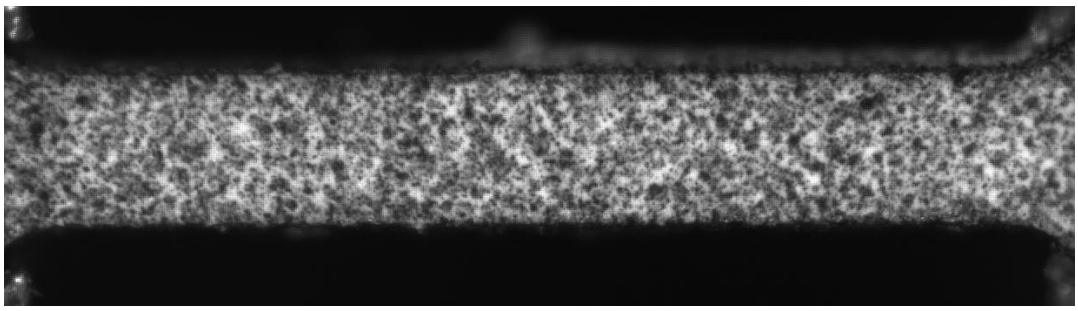

Figure 35 – Produced speckle pattern for DIC analysis.

3.4 Digital Image Correlation (DIC)

In this thesis, all presented stress strain responses are a result of DIC measurements of the microsamples. Images were recorded at a rate of 4 frames per second during testing. Load and displacement were recorded at the same rate and each value is synced with each image so that the reference image corresponds to the first load value. This allows for stress-strain responses to be generated. To analyze these images to produce strain, the DIC software VIC-2D by Correlated Solutions [168] was used. All samples were analyzed using the settings listed in Table 18.

Table 18 – DIC analysis settings.

Subset size	33
Step	4
Interpolation	Optimized 4-tap
Correlation Criterion	Normalized squared differences
Subset weights	Gaussian
Exhaustive search	Enabled
Low-pass filter images	Enabled
Incremental Correlation	Enabled
Prediction margin (pixel)	0.02
Confidence interval (pixel)	0.1
Matchability (pixel)	0.1

4 Results and Discussion

4.1 Introduction

In this chapter, the more relevant results of microsample mechanical testing of a simple geometry produced by additive manufacturing using DMLS will be presented. The results hereby presented were carried out with 22 microsamples of a total of two different directions (11 microsamples per direction), and comprise microstructure characterization, mechanical properties, including individual and average values, and fractography. The mechanical properties evaluated cover yield strength ($\sigma_{0.2}$), ultimate tensile strength (UTS), strain do failure (ε_F) and Young's modulus (E). The stress-strain curves will also be presented. The main aspects related to these results will be mentioned throughout this chapter, including the influence of microstructure in both orientation dependence and magnitude of mechanical properties, as well as the relationship between fracture surfaces and mechanical properties.

4.2 Microstructure Characterization

The microstructures were characterized utilizing optical metallography and imaged directly from the microsamples surfaces in order to understand the influence of microstructural features on properties. Figure 36 illustrate the microstructure for Ti64 produced by the DMLS system and it shows a predominantly acicular α phase microstructure with very small amounts of β in α boundaries.

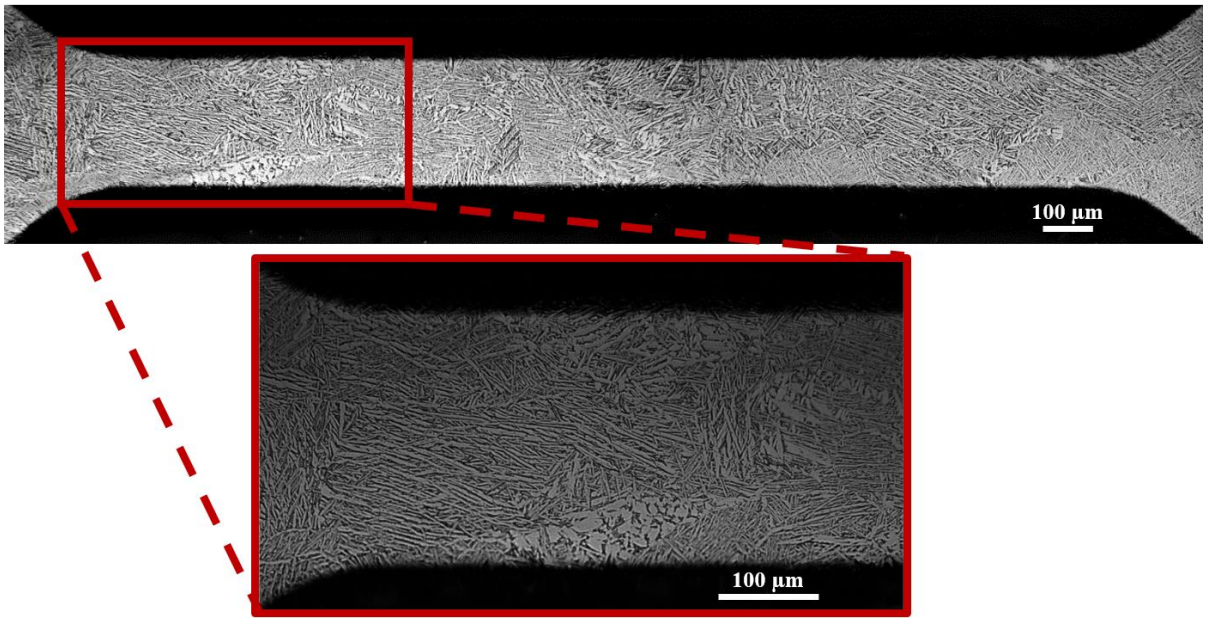

Figure 36 – Optical metallographic views for DMLS Ti6Al4V showing coarse, plate-like (acicular) α with some intergranular β (microsample #5 for direction d1).

The inherent rapid cooling of the material during DMLS resulted in martensitic laths that originated from the prior β grain boundaries and fill the columnar grains. Since the microstructure of the specimens is strongly dependent on cooling rate when β transforms to α from the transus temperature, different grain structures can result within the same AM part – see appendix A. These differences can also be explained by the number of layers within a microsample, which reflects the variance in properties. Thus, the implementation of a system to monitor temperature during processing is essential to understand the differences in microstructure.

Despite the microstructure shown in Figure 36 can be interpreted as acicular martensitic, coarsened α phase and larger α laths and colony sizes are also present. This a result of HIP post-processing used to close internal pores and cracks, that significantly changed the grain structure from the complete martensitic (α') microstructure expected in as-built conditions (see Figure 25) to an intermediate state between α-Ti dominated microstructure and martensite, i.e., increased α grain size and a still very small fraction of β phase. Therefore, one can easily conclude that the characterization of as-built microstructure is critical to applying the correct HIP post-processing of AM products.

4.3 Microsample Tensile Test Results

Table 19 shows the tensile test results obtained for the two tested directions, including Young's modulus (E), yield strength ($\sigma_{0.2}$), ultimate tensile strength (UTS) and elongation to failure (ε_F). Both individual (for each microsample) and average values are presented. Figure 37 shows the stress vs strain response for directions d1 and d2, whereas Figure 38 presents a summary plot of the resulting UTS and $\sigma_{0.2}$ for both directions. Figure 39 presents the plot of the resulting UTS as a function of distance from edge. As one can easily conclude, the values reveal an orientation-dependence for both yield strength, UTS and elongation to failure, in which direction d1 exhibits better mechanical properties. Furthermore, a smaller standard deviation for direction d1 can be seen, which indicates a more narrow range for UTS when compared to direction d2. This can also be witnessed in the stress-strain plots, where for direction d1 the curves are more close to each other. This may be due to the fact that the building layers within the microsamples are the same, since the distance from the substrate is the same. On the other hand, the Young's modulus is similar for both directions, demonstrating a non-dependency on sample orientation, which proves the Young's modulus is only dependent on the material. In fact, the value was found to be similar to what was expected.

Table 19 – Results of microsample tensile testing.

Direction	Microsample #	E (GPa)	$\sigma_{0.2}$ (MPa)	UTS (MPa)	ε_F (%)
d1	1	115.41	900.00	1006.76	15.51
	2	116.37	930.00	1021.96	11.46
	3	119.50	925.00	1020.67	13.03
	4	113.23	881.25	959.79	13.56
	5	122.68	960.00	1084.17	12.64
	6	115.55	975.00	1067.31	12.83
	7	118.55	962.50	1048.68	13.01
	8	111.94	975.50	1023.04	15.31
	9	109.59	927.50	1011.77	12.17
	10	118.38	965.00	1041.07	16.00
	11	100.43	975.00	1021.17	14.61
	Average	114.69 ± 5.71	943.34 ± 31.12	1027.85 ± 31.37	13.65 ± 1.42
d2	1	111.10	922.50	1049.18	13.18
	2	114.31	885.00	981.51	11.63
	3	109.68	870.00	966.96	11.44
	4	115.26	890.00	1013.44	8.41
	5	117.83	875.00	962.43	12.37
	6	100.07	874.50	941.19	11.51
	7	111.48	862.50	969.84	10.40
	8	124.98	865.00	980.52	12.64
	9	121.16	877.50	980.02	12.59
	10	117.30	750.00	858.41	12.26
	11	115.33	825.00	943.93	10.93
	Average	114.41 ± 6.23	863.36 ± 42.11	967.95 ± 45.21	11.58 ± 1.27

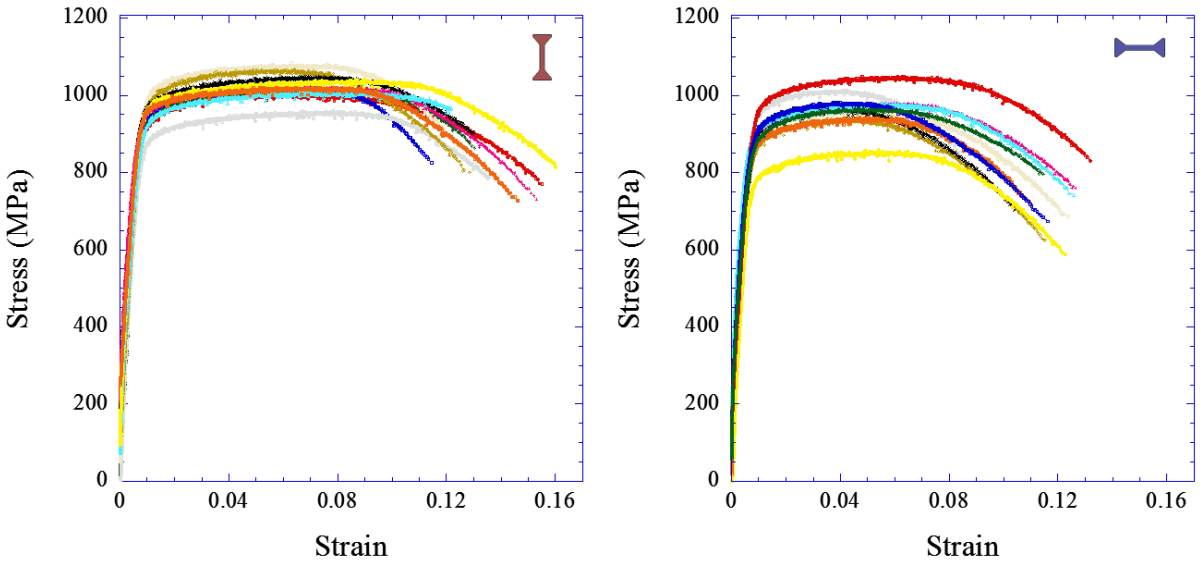

Figure 37 – Stress vs. Strain Curves for direction d1 (left) and direction d2 (right).

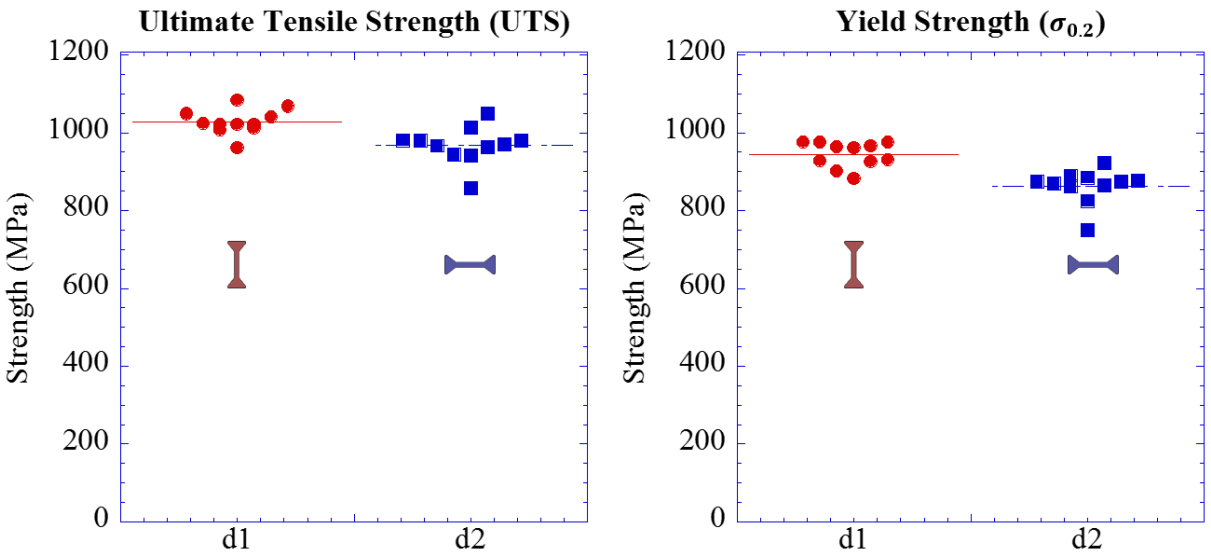

Figure 38 – Ultimate Tensile and Yield Strength values from directions d1 and d2 microsample testing.

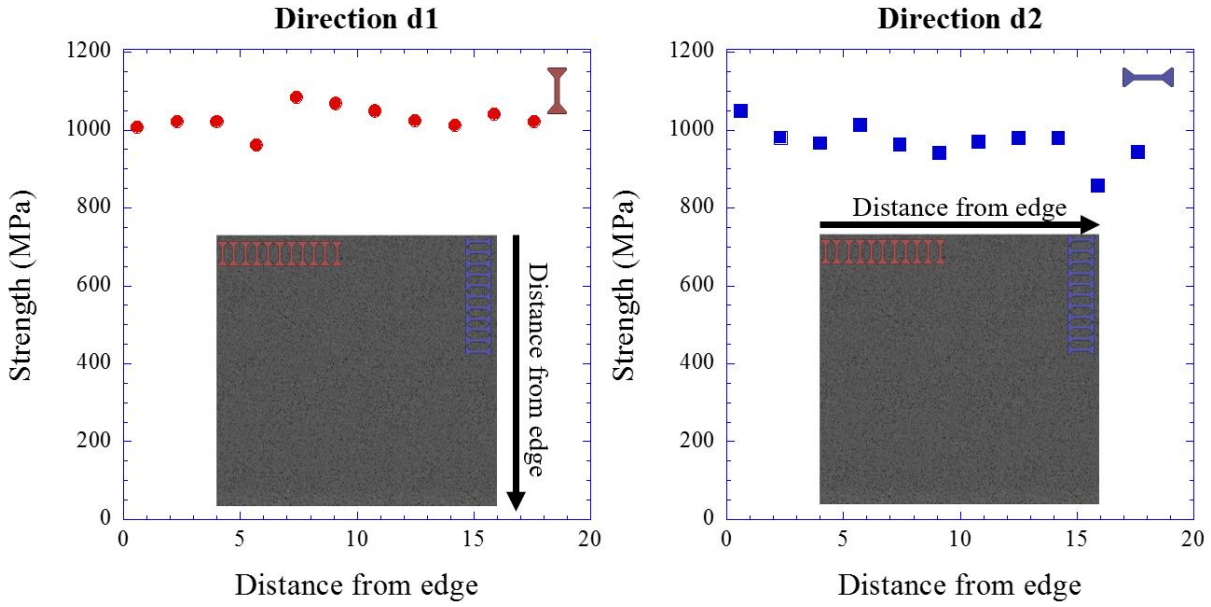

Figure 39 – Ultimate Tensile Strength vs. Distance from edge for directions d1 (left) and d2 (right).

In order to understand if there is in fact an orientation-dependence, a t-test was performed with the UTS values – see Table 20. As one can see, the t Stat is bigger than t Critical two-tail, thus rejecting the null hypothesis of mean difference. The observed difference between the two directions is convincing enough to say that the difference in properties is significantly dependent on the testing orientation/building orientation. However, it is recommended to perform more testing, since a higher number of observations will allow to describer better the magnitude of this difference.

Table 20 – Results from t-test: two samples assuming equal variances with UTS values.

	d1	d2
Mean	1027.85	967.95
Variance	1082.72	2248.23
Observations	11	11
Pooled Variance	1665.48	
Hypothesized Mean Difference	0	
df	20	
t Stat	3.44	
P(T<=t) one-tail	0.00129	
t Critical one-tail	1.72	
P(T<=t) two-tail	0.00258	
t Critical two-tail	2.09	

As mentioned before the mechanical properties of titanium alloys are directly related to microstructure features. The non-equilibrium microstructure present in Figure 36, with thin α' martensite laths (1-2 μm in width) along with coarsened α phase and larger α laths (4-12 μm in width) lead to a high strength, high elongation to failure. The fast heating and cooling of the laser conducted to improved tensile strength, which is explained by the fine martensite laths. However, the thermal post-processing HIP used to reduce porosity, led to an increase in α grain size, which reflects in the increased elongation to failure.

Table 21 shows a comparison of the results obtained from microsample testing with published values for other laser-based powder bed systems; the values are shown for samples with the same orientation and same conditions, i.e. as-HIPed condition. However, the elongation to failure is hard to compare directly, once the specimen gauge length varies between different investigations; it should be noted that there is no published work for additively manufactured Ti64 tested on a microscale. As it can be seen, the results obtained are comparable to the available published properties from the literature, which proves the reliability of the microsample mechanical testing technique in charactering AM parts. Moreover, the same material investigated in this work was also tested by NAS Pax River with macroscale samples; from a private communication [169], the results were reported to be very close to each other (e.g. the UTS values had an offset of 3 MPa). Nevertheless, one can conclude that properties depend on machine type, once they have different processing parameters.

Table 21 – Comparison of the results obtained from microsample testing with the published values for other laser-based powder bed systems AM Ti6Al4V.

Machine type	S.O	E (GPa)	$\sigma_{0.2}$ (MPa)	UTS (MPa)	ε_F (%)	Ref.
EOS M280	ZXY/ZYX (d1)	114.69 ± 5.71	943.34 ± 31.12	1027.85 ± 31.37	13.65 ± 1.42	–
SLM250	ZX	NA	NA	1088 ± 26.3	13.8 ± 1.3	[131]
SLM250	ZX	NA	962	1080	5	[133]
EOS M280	XZY/YZX (d2)	114.41 ± 6.23	863.36 ± 42.11	967.95 ± 45.21	11.58 ± 1.27	–
EOS	XZY	106.8 ± 1.3	835 ± 3.8	910 ± 2.9	NA	[127]
SLM	NA	115.4	885	973	19	[129]
SLM	X/Y	NA	858	937	8	[35]
	Z		1100	1209	11	
EOS M280	X/Y	NA	1109	1172	8	

Note: NA – Not available

Table 22 reports the material performance of additively manufactured Ti6Al4V compared to traditional manufacturing processes. From Table 22 one can conclude that DMLS process has the ability to deliver products having a microstructure which gives a mechanical behavior similar to and superior to cast, forged or wrought Ti64 products. Ultimate tensile strength of additively manufactured Ti64 exhibits a substantial increase over traditionally manufactured products with similar elongation to failure, thus demonstrating to be a reliable manufacturing process.

Table 22 – Comparison of tensile strength, yield strength and elongation of DMLS Ti6Al4V with traditional manufacturing processes.

Manufacturing Process	S. O	$\sigma_{0.2}$ (MPa)	UTS (MPa)	ε_F (%)	Ref.
DMLS, HIP	ZXY/ZYX (d1)	943.34 ± 31.12	1027.85 ± 31.37	13.65 ± 1.42	–
	XZY/YZX (d2)	863.36 ± 42.11	967.95 ± 45.21	11.58 ± 1.27	–
Cast	NA	795	900	10	[100]
Forged	NA	795	860	15	[100]
Wrought, Annealed	NA	795	860	15	[100]

Note: NA – Not available

4.4 Fractography

In order to understand the failure mechanisms and to explain the mechanical properties, the fracture surfaces of the tested samples were examined using scanning electron microscopy (SEM). Figure 40 shows EM views of a fracture surface of a tested microsample. The fracture surface shows a cup and cone type of fracture with shear dimpling and void coalescence, showing the material failed by ductile fracture (reflected on the increased elongation to failure). This ductile failure mode exhibits equiaxed dimples as a result of voids nucleation in the necking region. This equiaxed array is represented by the matching dimples on both fracture surfaces. In addition, the evident distribution of dimple sizes can be explained by inclusions, such as micro-porosity seen in Figure 40. It should be also noted that the apparent surface roughness it is not a result from AM, but from microsample extraction by wire EDM, and it does not influence mechanical properties.

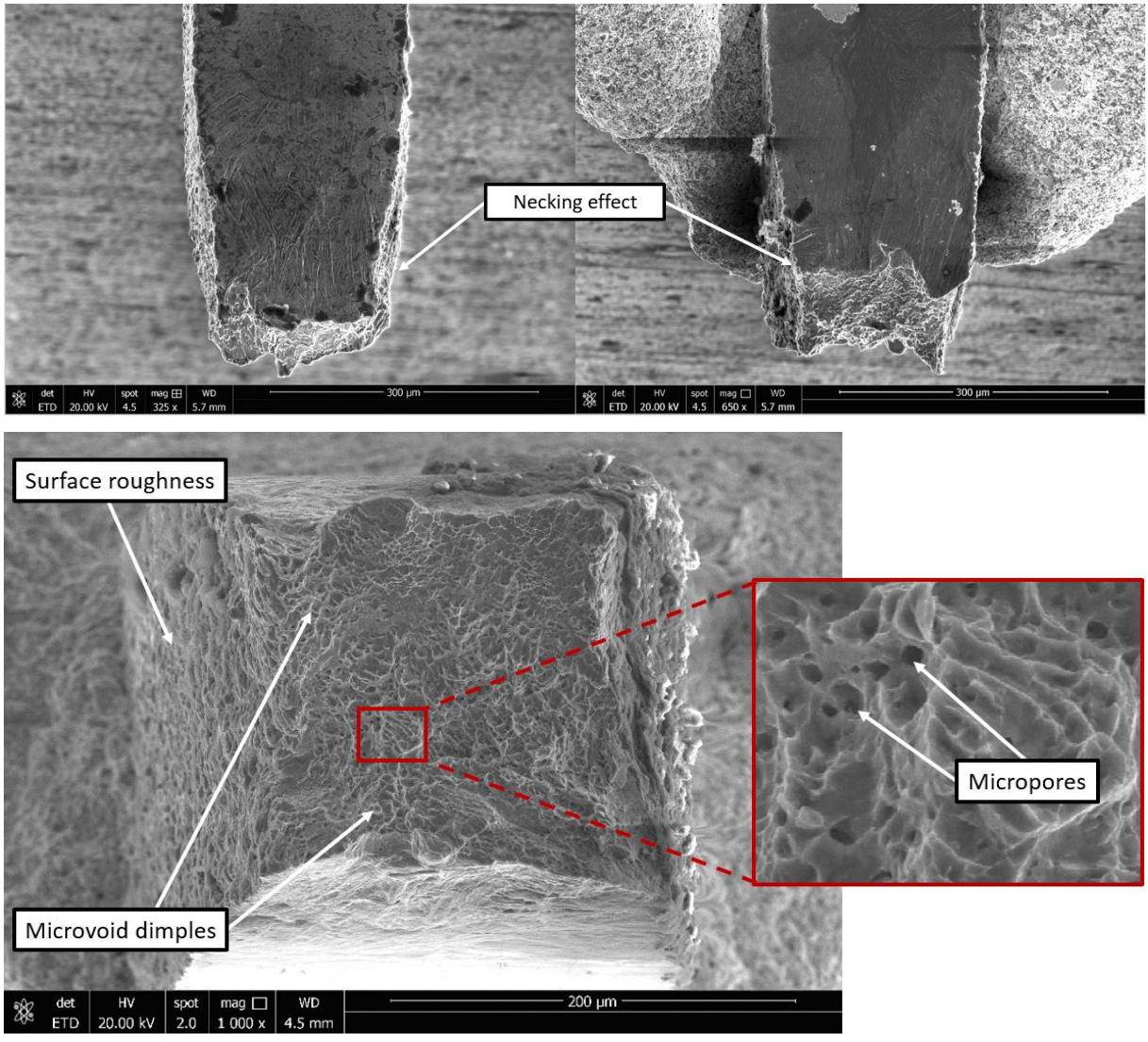

Figure 40 – SEM images showing microsample fracture surface features for DMLS Ti6Al4V (microsample #5 for direction d1).

4.5 Discussion of microstructure, tensile properties and fracture surfaces correlation

First and foremost, the characterization of microstructure, mechanical properties and fracture surfaces of DMLS Ti64 in two different directions exposed the anisotropy in properties typical of AM. This effect of test orientation/build direction is particularly shown in microsample mechanical testing. The size of the samples (microscale) allowed to directly-measure material mechanical data on critical regions, which was reflected in higher standard deviations when compared to macroscale testing. Furthermore, this anisotropic behavior was specially observed in microstructural changes (see appendix A), more specifically between directions d1 and d2; even though this differences can also be seen within the same direction. The potential sources of anisotropy in properties will be summarized as follows.

As stated before, the anisotropy can be mainly witnessed in microstructure changes. Evolution of microstructure is determined by the temperature gradient and laser reheating time. Since DMLS is a layer-by-layer deposition, different layers can result within a microsample. This significant layers distribution can be attributed to element segregation during the laser reheating process [135]. This effect can be mainly seen in direction d2, where the standard deviation is higher. In addition, poor bonding between layers can occur, which may be the explanation for the lower values of direction d2; different corrosion effects can occur from poor bonding, thus leading to a larger variance of results. Therefore, an in-situ inspection system should be used to monitor temperature and atmosphere, as these play an important role on microstructure and, therefore, mechanical properties.

The presence of defects can also describe anisotropy. Due to the small cross section area (250µm x 250µm), the present of a defect (e.g. voids) within the gage will result in lower strength. In the same way, the presence of pores at the surface (called “open” pores) is a problem, especially for as-HIP conditions. These “open” pores are a problem as they allow deeper infiltration into material from air during high heat cycles; even though the microsamples were polished before testing, these infiltrations could still be present.

In order to understand the correlation between microstructure, tensile properties and fracture surfaces, as well as the ability of microsample testing in analyzing anisotropy, four different situations will be discussed: (a) highest UTS, (b) lowest UTS, (c) highest elongation do failure, and (d) lowest elongation to failure.

Figure 41 and Figure 42 show SEM and optical metallographic images respectively for microsample #5 for direction d1, which represents the highest UTS (1084.17 MPa). As one can

see, there is no evidence of defects on the fracture surface. In addition, the fracture appears to be around a zone that exhibits very fine laths (0.7 – 0.9 μm in width). Furthermore, it can also be witnessed a basket-weave kind of structure around the fracture, which leads to a higher strength. All of these factors led to an increase of strength for this microsample (approximately 5% greater than the average). Another possible reason may be a good bonding between building layers, which also describes why the properties are higher along the building direction (d1).

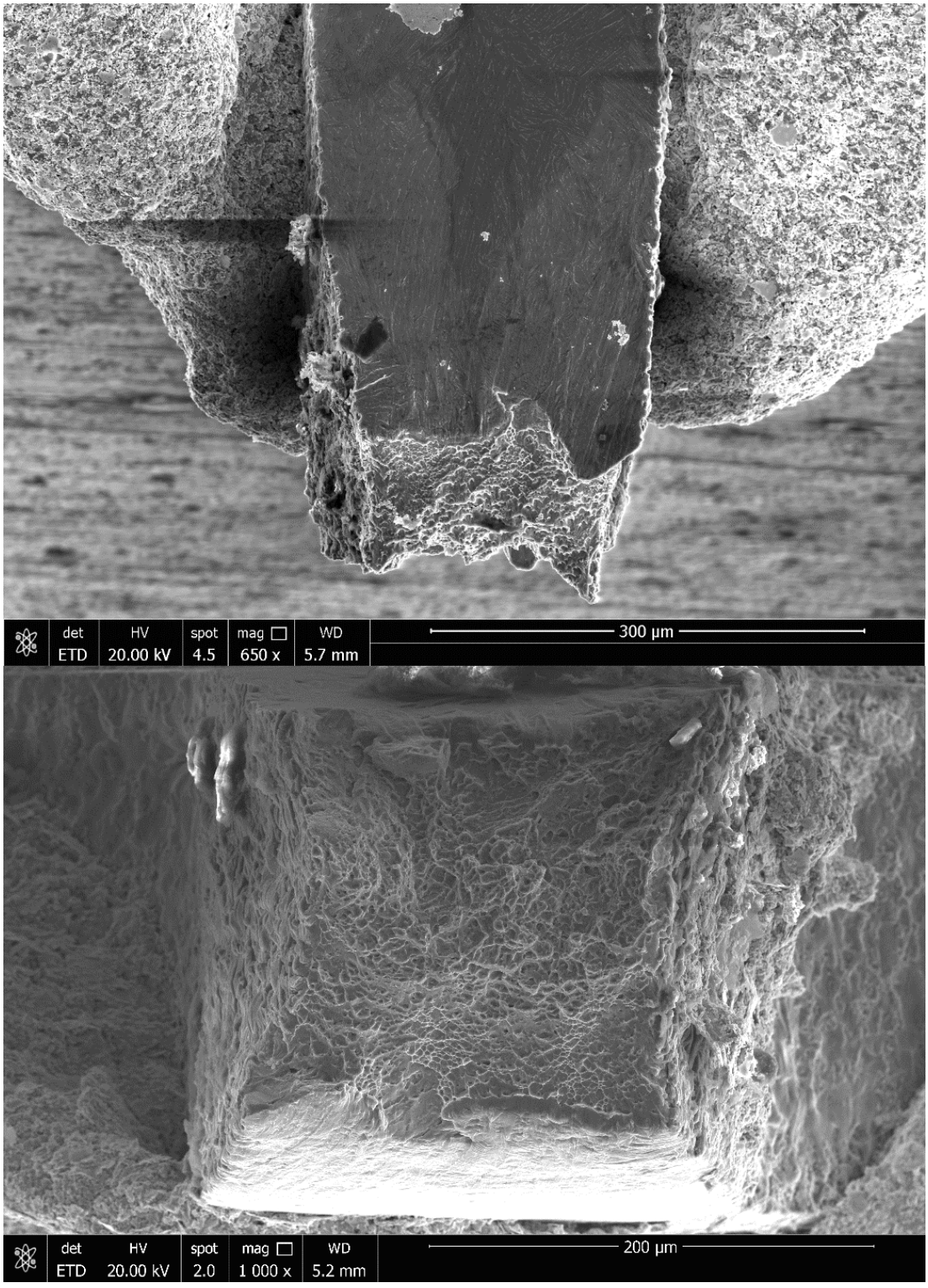

Figure 41 – SEM view for microsample #5 direction d1.

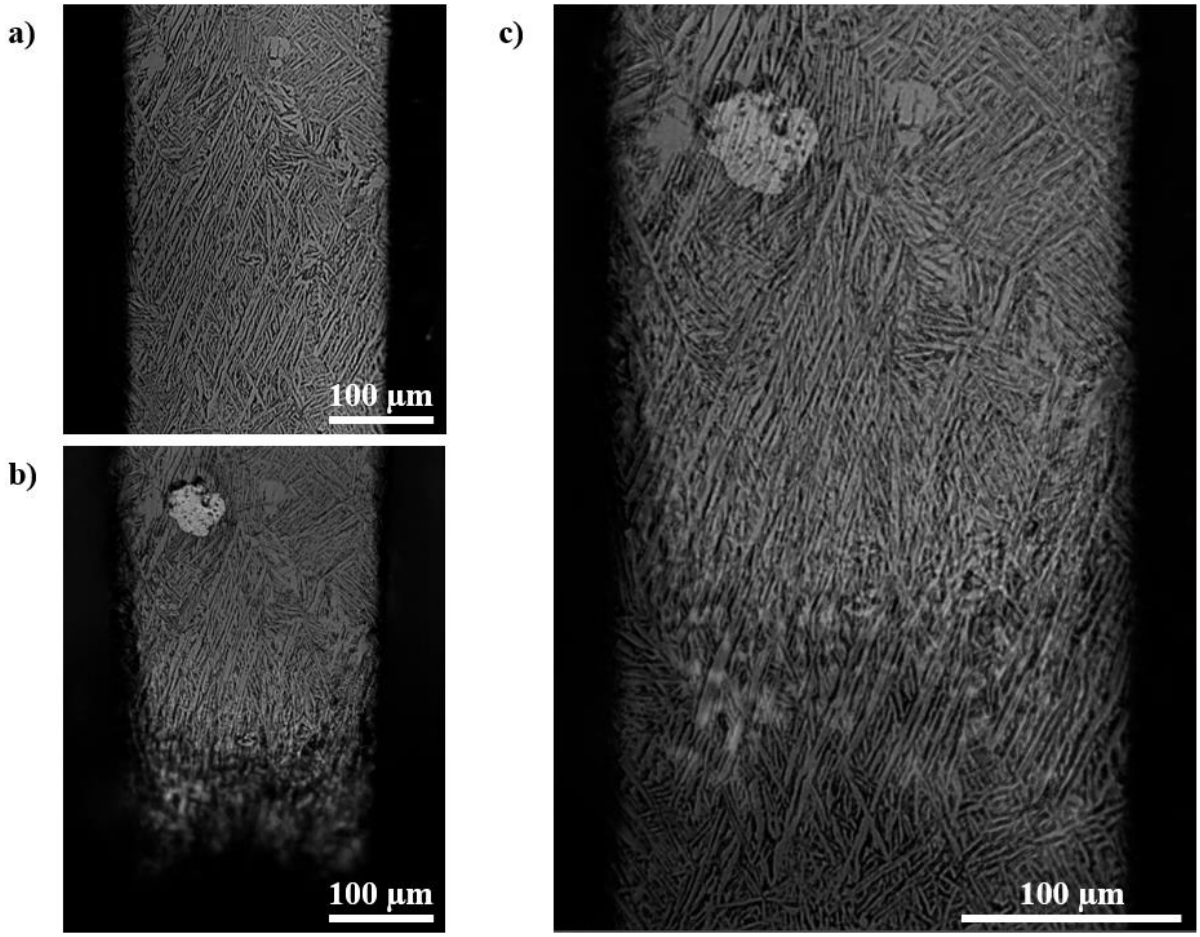

Figure 42 – Optical metallographic view from microsample #5 direction d1; (a) before testing; (b) after testing; (c) superimposition of (a) and (b) images.

The lowest UTS (858.41 MPa), exhibited by microsample #10 direction d2, will now be discussed. From microstructure and fractography analysis, some features were found to be potential sources for this lower value. From Figure 43, two different potential sources can be found. On the first view an evident inclusion can be seen. This inclusion as the appearance of dust that may be unsintered powder, which could be a result from spatter ejection during beam melting; this "dust" can also be vaporized metal, which could lead to what can be interpreted as a void – see last image of Figure 43. An electron dispersive spectroscopy (EDS) analysis was also made, which discarded the hypothesis of this defect being interpreted as a second-phase micro-cavity.

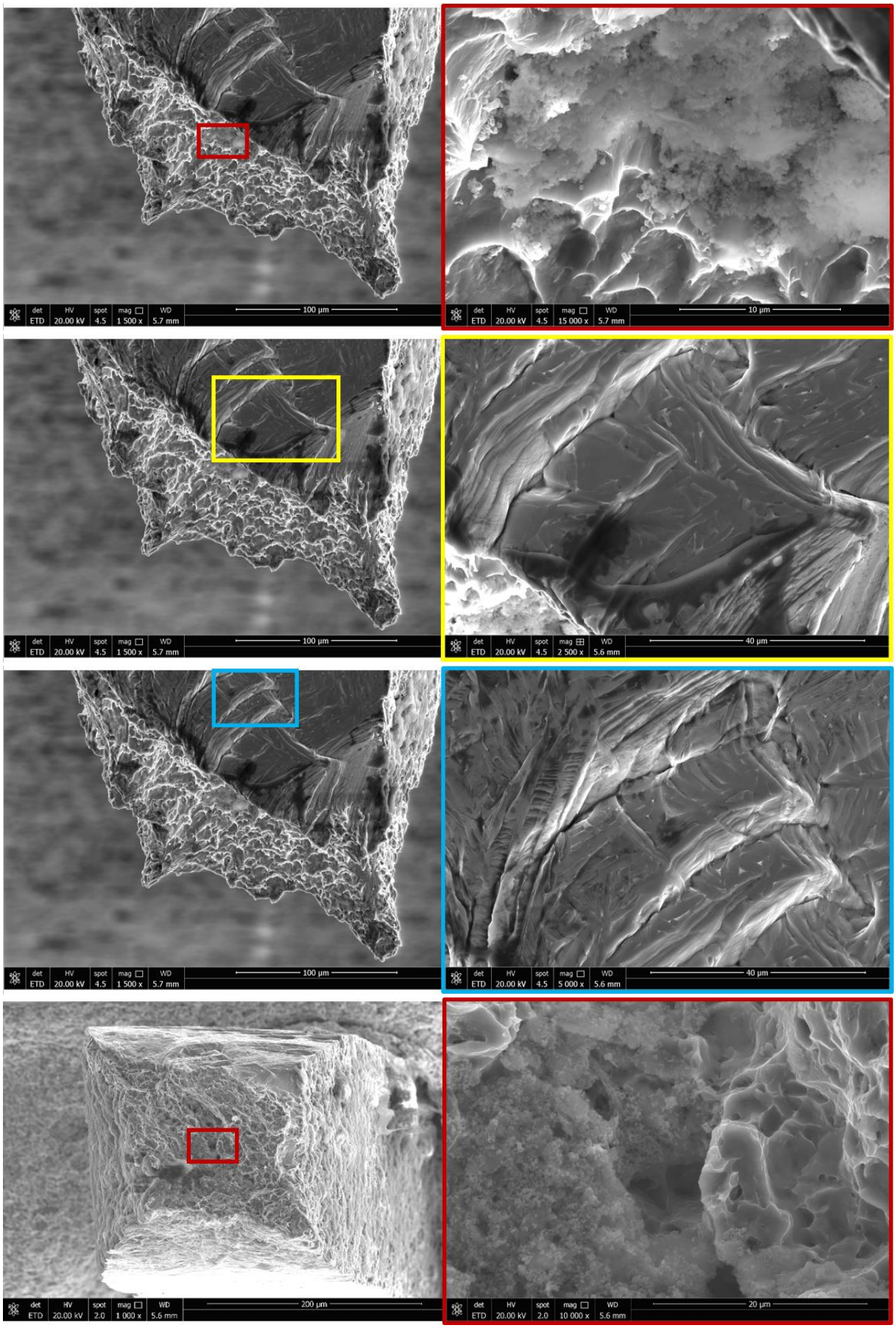

Figure 43 – SEM views showing potential sources for the lowest UST value of microsample #10 direction d2.

On the other two views in Figure 43, there is surface features that can be related to dislocation bands that resulted from necking. Even though necking is common for every sample, only this sample showed these features, which can be related to localized strain and, therefore, a lower strength. It can also be a microstructure related defect (Figure 44) or even a crack; however, in order to fully understand what these features mean, further investigation needs to be done.

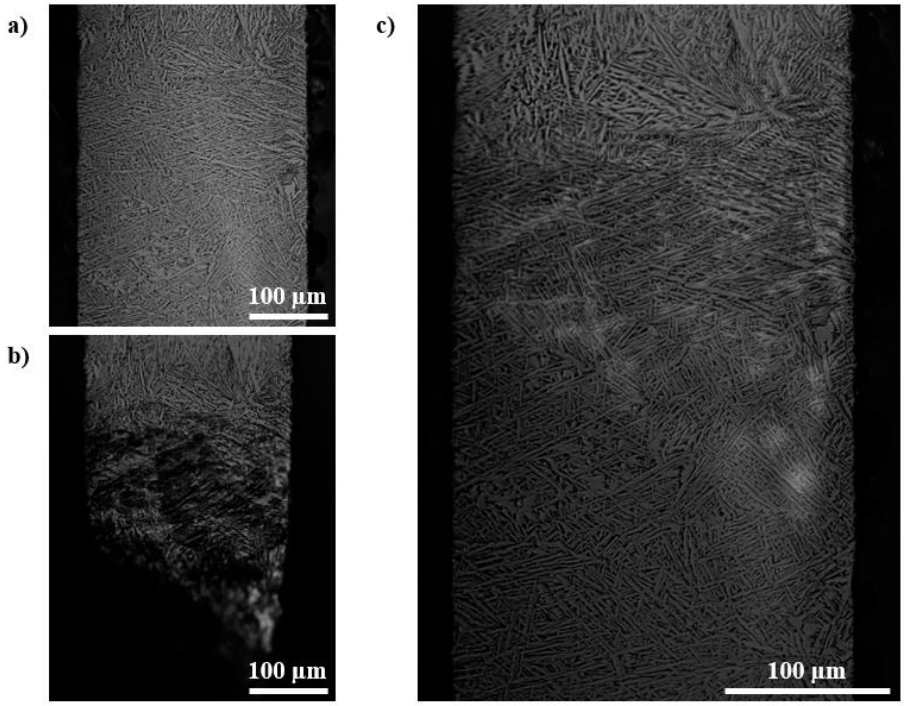

Figure 44 - Optical metallographic view from microsample #10 direction d2; (a) before testing; (b) after testing; (c) superimposition of (a) and (b) images.

Figure 45 shows another potential source for the lowest strength of microsample #10 direction d2. As it can be seen, there is a smoother surface, on what seems to be a presence of a microcrack, decreasing in this way the strength of the sample.

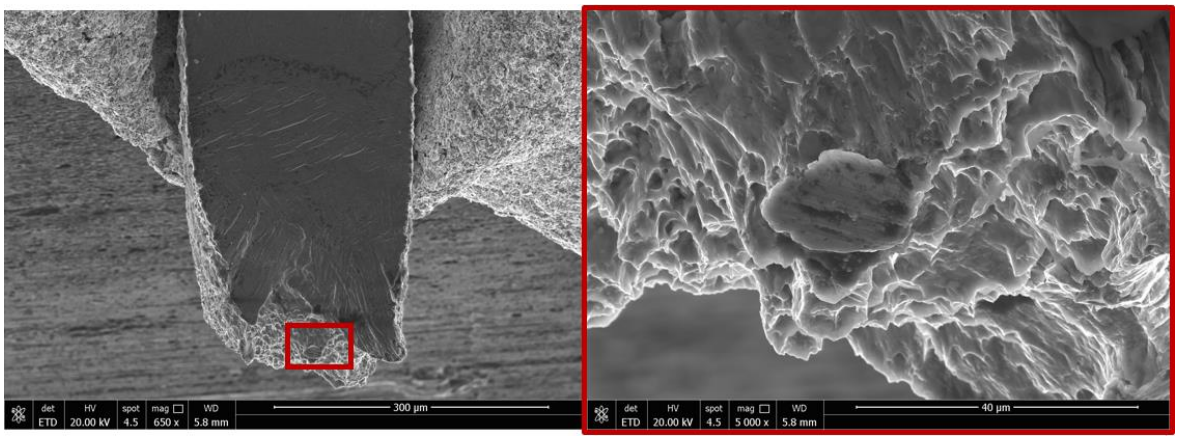

Figure 45 – SEM view of the fracture surface from the other half of microsample #10 direction d2 showing a potential source for the lowest UTS.

Regarding elongation to failure, the highest value was registered by microsample #10 direction d1 (16.00%). As it can be seen in Figure 46 the fracture occurred near coarse α grains, which is a result of HIP post-processing. This larger grains will carry a higher elongation. Furthermore, this higher elongation is also represented by the more pronounced necking effect (characterized by the higher reduction of cross sectional area) seen in the fracture surface (Figure 47).

On the other hand, the fracture surface of the microsample with the lowest elongation to failure (8.41%; microsample #4 direction d2) exhibits less necking effect and, therefore, less reduction of area, as it can be seen in Figure 48. In addition, point-initiated fracture appeared to result from microstructural inhomogeneities (see Figure 49), which can lead to a substantial decrease in ductility.

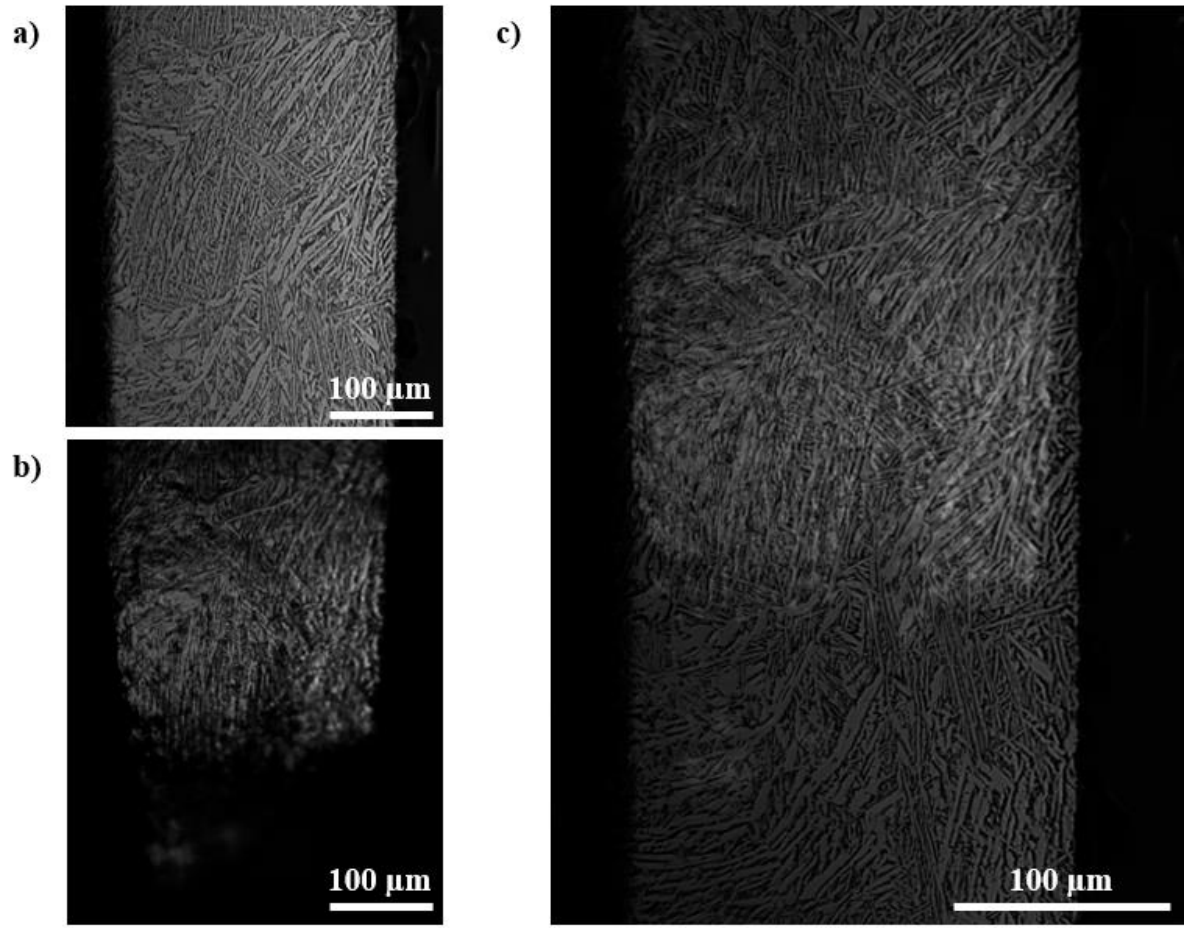

Figure 46 - Optical metallographic view from microsample #10 direction d1; (a) before testing; (b) after testing; (c) superimposition of (a) and (b) images.

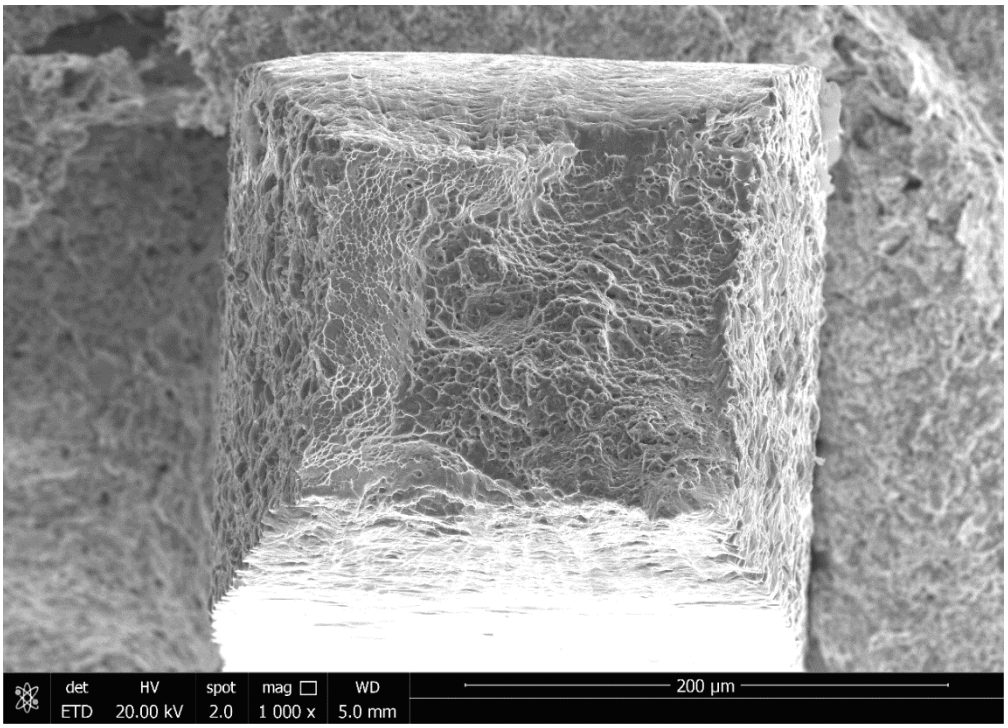

Figure 47 - SEM top view of the fracture surface of microsample #10 direction d1.

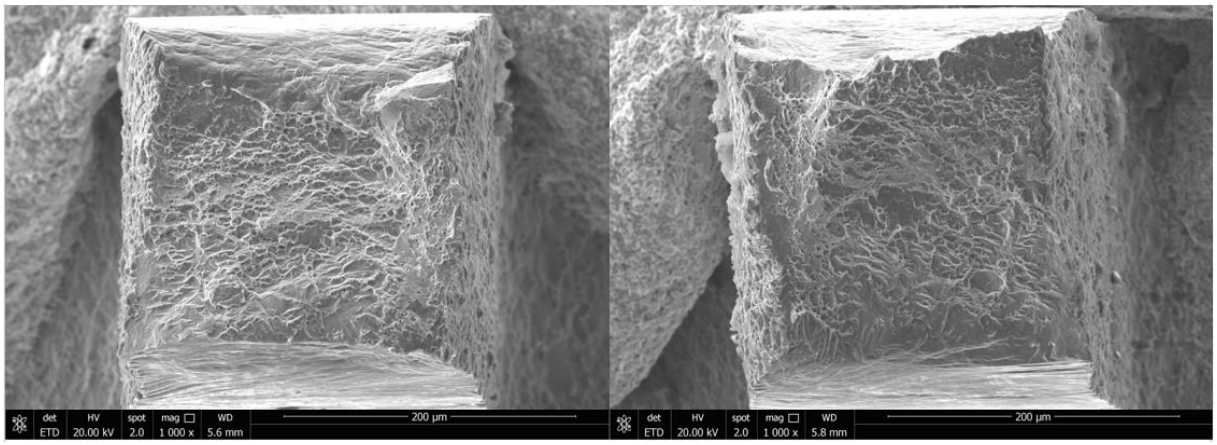

Figure 48 - SEM top views of the matching fracture surfaces of microsample #10 direction d1.

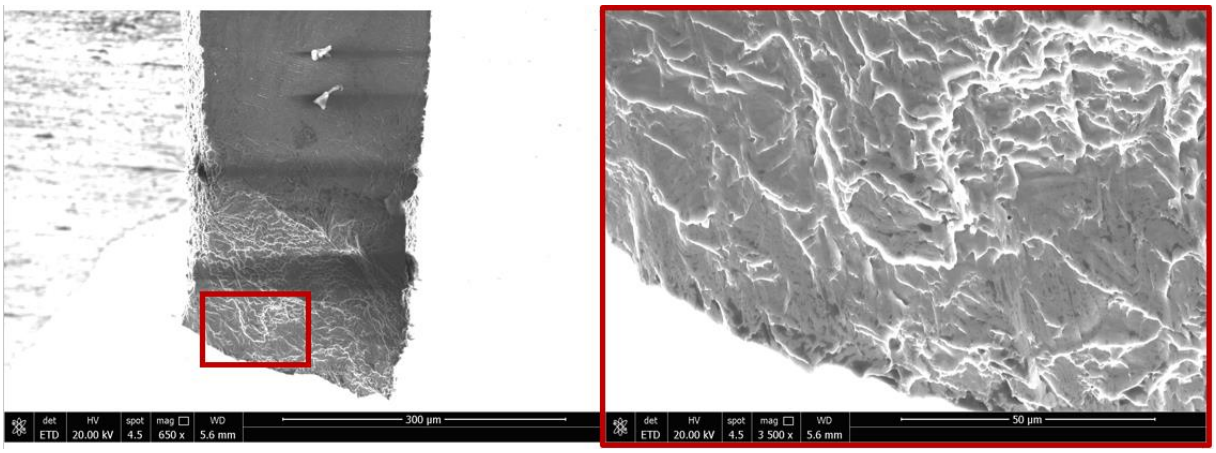

Figure 49 - SEM view of the fracture surface from microsample #4 direction d2 showing a potential source for the lowest elongation to failure.

5 Concluding Remarks

5.1 Introduction

In this work, a new qualification methodology for additively manufactured parts has been evaluated. A Ti6Al4V DMLS produced plate was subjected to microsample mechanical testing technique, in which the local mechanical behavior was characterized in two different directions such that the tensile axis was aligned along (a) the building direction (d1) and (b) transversal to building direction (d2). The results were then compared with macrosample tested samples and published values. After this work, the sensibility needed to better understand the mechanical behavior of AM produced components has been acquired, as well as the skills to perform mechanical testing in a microscale.

5.2 Materials, Applications and Producing Steps

In recent years additive manufacturing (AM) has provided a renaissance in manufacturing. As a disruptive technology, AM is able to produce complex shapes of custom-designed components and depending on the heat source (laser or electron beam), these shapes are built through computer-controlled, self-assembly by sintering or melting powder at different combinations of absorbed power and beam velocity. Therefore, the proper design and application of additively manufactured parts is essential. It mainly depends on a thorough characterization and understanding of not only the processing and post-processing parameters, but also of the raw material. Particularly, understand the effect of changing the material and/or geometry features is of very importance, once it affects considerably the whole component behavior.

Compared to traditional manufacturing, AM is distinctly suitable for applications with low volume production, especially for parts with complex geometries and expensive materials. Over the past 20 years, the research community has developed innovative, advanced AM techniques and applied them in aerospace, automotive, biomedical, among others fields. Although only a limited number of metallic alloy systems are currently available, such as titanium alloys, aluminum alloys, and stainless steels, being the bulk of published data generated on Ti6Al4V.

Developed in the early 1950s for aerospace applications, Ti6Al4V, also known as Ti64, is the most widely used titanium alloy due to its exceptional good balance of strength, ductility, fatigue, and fracture properties. Being an $\alpha+\beta$ alloy, its microstructure is highly dependent on

cooling rate from the β transus temperature. In AM, the evolution of microstructure is determined by temperature gradient and laser reheating time. Therefore, a variety of microstructures can result from AM depending not only on machine type, but also on post-processing (e.g. HIP) parameters.

During this work, in addition to the widespread dissemination of the excellent capabilities of AM, one can conclude that a lot of challenges remain for AM to become a common fabrication method for in-service parts. Even though there is a lot of studies developed for metal AM, it was found to be relatively few data published on standard samples, environmental effects, and inconsistency of properties within and between builds in one machine and across different machines. Furthermore, the source(s), detection, and elimination of process-induced defects, as well as location/orientation-dependent properties, remain areas requiring additional focus.

Although the breadth of published data to not cover these existing problems, some of the mechanical properties for AM Ti64 reported to be similar and superior to wrought or cast products. However, despite AM has opened new possibilities in manufacturing, whether AM is the best manufacturing method for a particular product must be determined based on the part to be made.

5.3 Experimental Testing

The microsample mechanical testing technique has proven to be reliable in characterizing a Ti6Al4V additively manufactured plate. The results showed values similar to the NAS Pax River macrosample results, as well as the available published properties from the literature, which attests this new developed approach to work well in characterizing a variety of materials such as bulk, metal alloys or thin films.

The microscale sized samples characterization has confirmed the aptitude to provide information that would otherwise be averaged or masked on the macroscale. During this investigation, this technique has found out to be particularly suitable to characterize the typical anisotropic behavior of additively manufactured parts. The micro-tensile measurements allowed to directly-measure material mechanical data on critical regions, which resulted in higher standard deviations when compared to macroscale testing. In this type of testing, microstructural features, as well as the presence of process-induced defect such as micro-porosity, micro-cracks, or even un-melted powder, turned out to be particularly important in the mechanical behavior of each sample. Moreover, this anisotropy was also reflected in the

orientation-dependent properties, in which the samples with the tensile axis aligned along the building direction (d1) exhibited better mechanical properties.

Summing up, this innovative developed methodology demonstrated the importance to understand the local microstructure within the gage length of a sample. For that reason this alternative route showed the potential to substitute the outputs of intermediate microstructural models, thus providing verifiable property data as inputs to global part performance and failure models. In addition, it was possible to conclude that testing microsamples harvested from bulk materials can be difficult due to the sample preparation required.

In this work, the DMLS process has demonstrated to produce a wide range of characteristic crystallographic phases – α (hcp), β (bcc) and α' (hc martensite) – on Ti6Al4V. The resulted microstructure showed a predominantly acicular α phase microstructure with very small amounts of β in α boundaries. This non-equilibrium microstructure presented thin α' martensite laths (1-2 μm in width) along with coarsened α phase and larger α laths (4-12 μm in width), which led to a high strength, high elongation to failure material. The high tensile strength, explained by the fine martensite laths, was due to fast heating and cooling of the laser, whereas the high elongation was due to thermal post-processing (HIP) used to reduce porosity, that increase the α grain size.

Regarding the material performance of the additively manufactured Ti6Al4V, the results have corroborated the scenario of a third industrial revolution. The DMLS Ti6Al4V produced plate has showed an increase of strength over traditional processes and similar elongation to failure. Yield strengths have reached 943 MPa and 863 MPa for directions d1 and d2, respectively, over 795 MPa for cast, forged and wrought products [100]. Likewise, ultimate tensile strength has increased from 900 MPa for cast products, and 860 MPa for forged and wrought [100], to 1028 MPa and 968 for directions d1 and d2, respectively. The corresponding elongations to failure were similar: 14% for d1 and 12% for d2, against 10% for cast and 15% for forged and wrought [100]. The difference in properties between d1 and d2 evidenced once again the orientation-dependent properties, showing future research needs addressing this issue.

Lastly, the fracture surfaces were also examined. These have exhibited a cup and cone type of fracture with shear dimpling and void coalescence, showing the material failed by ductile fracture (reflected on the increased elongation to failure). From fractography was possible to understand the correlation between microstructure, tensile properties and fracture surfaces.

5.4 Future Development and Research

As mentioned in the introduction of this work, this represents the first step in the development of a new qualification methodology for additively manufactured components. Therefore, there are a few areas that should be addressed concerning not only the microscale testing system design, but also the AM technology as well.

Regarding the system design a few improvements could be made, such as the implementation of a new lens with better resolution, or even a device that could measure strain in real time. It could be also installed a load cell capable of higher forces to allow testing of stronger materials.

About the tested material, future research addressing the effects of chamber environment where the part is being built in, as well the temperature gradient during processing, should be made to better understand their influence on properties. Moreover, other processing parameters, such as the laser scanning velocity and/or scanning strategy, along with the use of different starting powders, should be investigated to produce specific microstructures and microstructural variations during the build process to make AM a truly multi-functional materials manufacturing process. In addition, mechanical testing should be made for as-built conditions and after post-processing operations with the same material, in order to compare results and, then, comprehend the effects of post-processing.

Likewise, and using the capabilities of microscale testing, it could be interesting to understand the influence of some features (e.g. holes or thin walls) on the mechanical performance of additively manufactured components. High temperature testing could also be an interesting approach, as the microstructure of titanium alloys, and more specifically Ti64, has proven to be highly influence by heating cycles.

Another area that should be addressed is the orientation-dependent properties seen in the results, as it seemed to be a trend along direction d2 (Figure 50). However, by only testing all the way through the height of the plate a conclusion could be drawn.

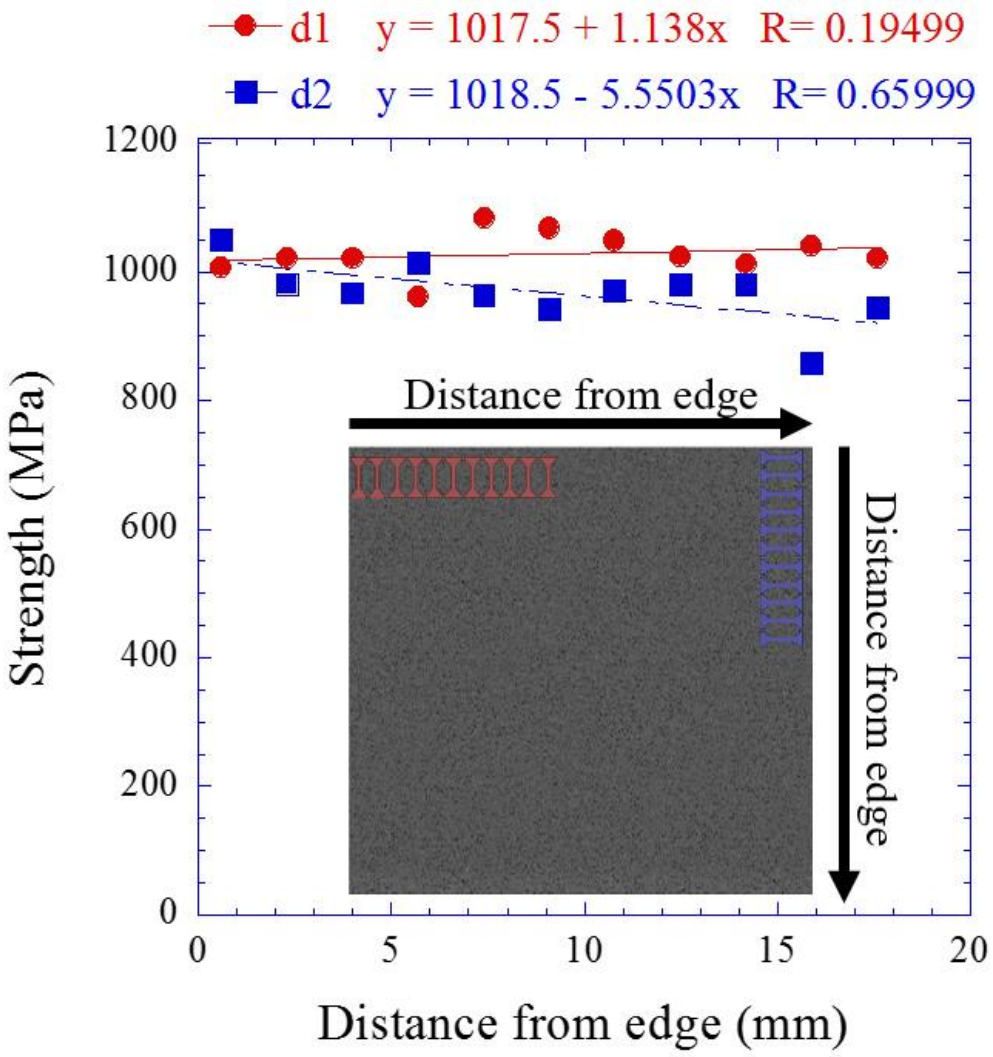

Figure 50 – Ultimate Tensile Strength vs. Distance from edge for directions d1 and d2, with respective linear regression curves.

Lastly, the presence of voids within the microspecimen's gage should also be investigated, to understand their influence in the mechanical resistance, or even understand if microporosity could lead to cracking. In fact, as one can see in Figure 51, this issue has started to already be addressed, as the DMLS studied plate was scanned with a CT scanner, and some voids were observed. Moreover, the area where these voids were found was polished up to the point where these voids could be viewed with the optical microscope.

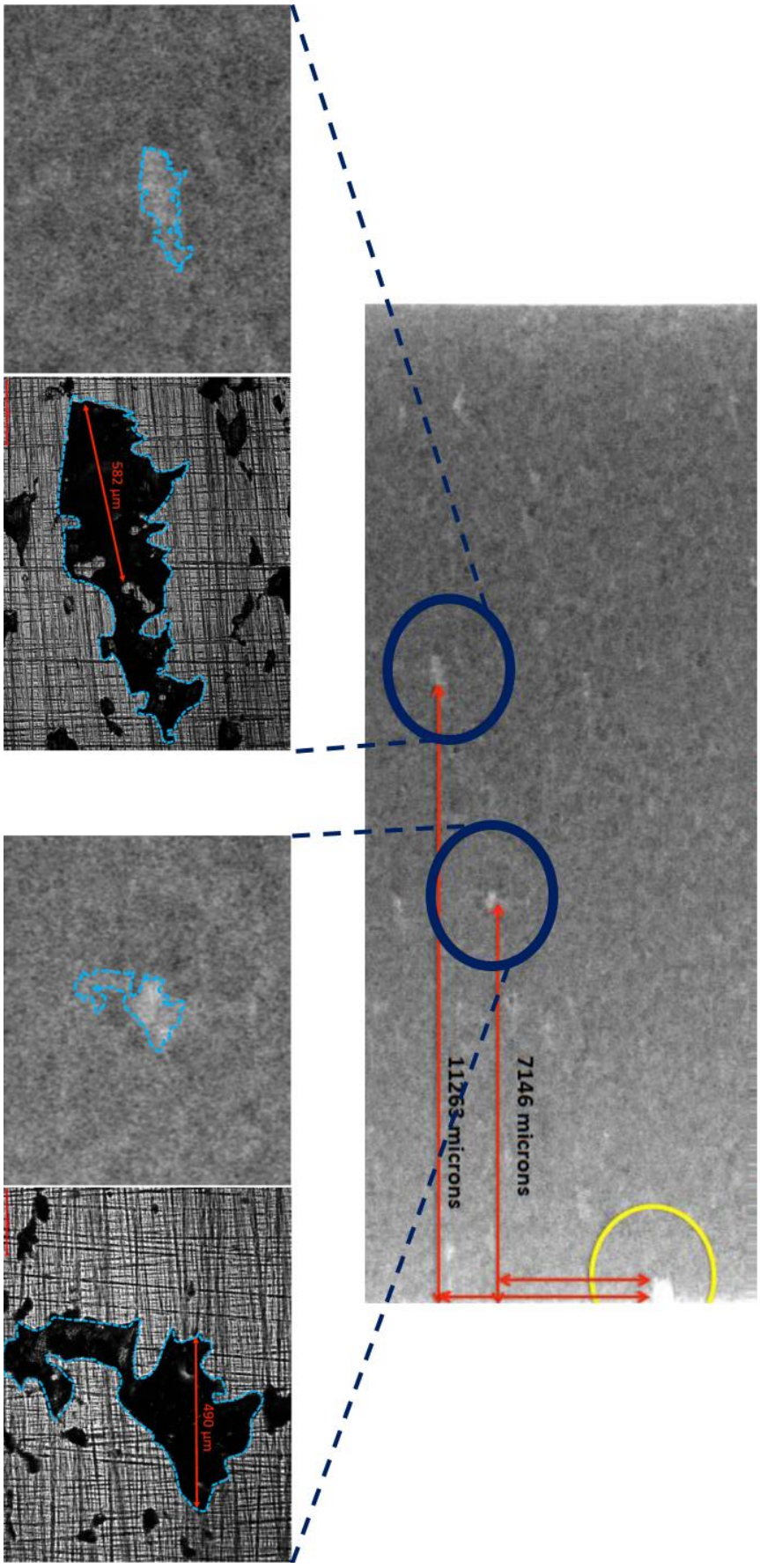

Figure 51 – Voids investigation in the DMLS Ti6Al4V plate.

References

[1] ASTM, 2012, "ASTM F2792-10 Standard Terminology for Additive Manufacturing Technologies," ASTM F2792-10e1West Conshohocken, PA.

[2] Guo, N., and Leu, M. C., 2013, "Additive manufacturing: technology, applications and research needs," Frontiers of Mechanical Engineering, 8(3), pp. 215-243.

[3] Huang, Y., Leu, M. C., Mazumder, J., and Donmez, A., 2015, "Additive manufacturing: Current state, future potential, gaps and needs, and recommendations," Journal of Manufacturing Science and Engineering, 137(1), p. 014001.

[4] Gibson, I., Rosen, D. W., and Stucker, B., 2010, Additive Manufacturing Technologies, Springer.

[5] Cooper, K., 2001, Rapid Prototyping Technology: Selection and Application, CRC press.

[6] Palermo, E., 2016, "What is Stereolithography?", http://www.livescience.com/38190-stereolithography.html. [Accessed in May 26, 2016]

[7] 3DSystems, "What Is An STL File?", http://www.3dsystems.com/quickparts/learning-center/what-is-stl-file. [Accessed in May 27, 2016]

[8] Campbell, T., Williams, C., IVANOVA, O., and Garrett, B., 2011, "Could 3D Printing Change the World? Technologies, Potential and Implications of Additive Manufacturing, Strategic Foresight," Atlantic Council (www. acus. org).

[9] Coykendall, J., Cotteleer, M., Holdowsky, J., and Mahto, M., 2014, "3D opportunity in aerospace and defense: Additive manufacturing takes flight," A Deloitte series on additive manufacturing, 1.

[10] Goldsberry, C., 2009, "Rapid change in additive-manufacturing landscape", http://www.plasticstoday.com/rapid-change-additive-manufacturing-landscape/85941459213194. [Accessed in May 27, 2016]

[11] Kruth, J.-P., Leu, M.-C., and Nakagawa, T., 1998, "Progress in additive manufacturing and rapid prototyping," CIRP Annals-Manufacturing Technology, 47(2), pp. 525-540.

[12] Huang, Y., and Leu, M. C., 2014, "Frontiers of Additive Manufacturing Research and Education."

[13] Wohlers, T., 2005, "Wohlers Report," Rapid Prototyping, Tooling & Manufacturing State of the Industry, Fort Collins, Colorado, USA.

[14] Pham, D., and Dimov, S., 2003, "Rapid prototyping and rapid tooling—the key enablers for rapid manufacturing," Proceedings of the Institution of Mechanical Engineers, Part C: Journal of Mechanical Engineering Science, 217(1), pp. 1-23.

[15] Scheck, C., Jones, N., Farina, S., George, C., and Melendez, M., 2014, "Technical Overview of Additive Manufacturing," Naval Surface Warfare Center, Carderock Division.

[16] Murr, L., Quinones, S., Gaytan, S., Lopez, M., Rodela, A., Martinez, E., Hernandez, D., Martinez, E., Medina, F., and Wicker, R., 2009, "Microstructure and mechanical behavior of Ti–6Al–4V produced by rapid-layer manufacturing, for biomedical applications," Journal of the mechanical behavior of biomedical materials, 2(1), pp. 20-32.

[17] Thomas, C. L., Gaffney, T. M., Kaza, S., and Lee, C. H., "Rapid prototyping of large scale aerospace structures," Proc. Aerospace Applications Conference, 1996. Proceedings., 1996 IEEE, IEEE, pp. 219-230.

[18] Concept Laser Gmb H., http://www.concept-laser.de/. [Accessed in May 28, 2016]

[19] ExOne, http://www.exone.com/. [Accessed in May 28, 2016]

[20] Optomec, http://www.optomec.com/. [Accessed in May 28, 2016]

[21] Giffi, C., Gangula, B., and Illinda, P., 2014, "3D opportunity for the automotive industry: Additive manufacturing hits the road," Deloitte University Press, May.

[22] Mironov, V., Visconti, R. P., Kasyanov, V., Forgacs, G., Drake, C. J., and Markwald, R. R., 2009, "Organ printing: tissue spheroids as building blocks," Biomaterials, 30(12), pp. 2164-2174.

[23] Ringeisen, B. R., Pirlo, R. K., Wu, P. K., Boland, T., Huang, Y., Sun, W., Hamid, Q., and Chrisey, D. B., 2013, "Cell and organ printing turns 15: diverse research to commercial transitions," MRS bulletin, 38(10), pp. 834-843.

[24] Sames, W., List, F., Pannala, S., Dehoff, R., and Babu, S., 2016, "The metallurgy and processing science of metal additive manufacturing," International Materials Reviews, pp. 1-46.

[25] Vayre, B., Vignat, F., and Villeneuve, F., 2012, "Metallic additive manufacturing: state-of-the-art review and prospects," Mechanics & Industry, 13(02), pp. 89-96.

[26] Herderick, E., 2011, "Additive Manufacturing of Metals: A Review," Materials Science & Technology, pp. 1413-1425.

[27] Frazier, W. E., 2014, "Metal Additive Manufacturing: A Review," Journal of Materials Engineering and Performance, 23(6), pp. 1917-1928.

[28] Wohlers, T., 2014, "Wohlers report 2014: 3D printing and additive manufacturing state of the industry annual worldwide progress report., Fort Collins, CO: Wohlers Associates," Inc.

[29] ASTM, 2012, "ASTM F2792-12a Standard Terminology for Additive Manufacturing Technologies," ASTM F2792-12aWest Conshohocken, PA.

[30] King, W., Anderson, A., Ferencz, R., Hodge, N., Kamath, C., Khairallah, S., and Rubenchik, A., 2015, "Laser powder bed fusion additive manufacturing of metals; physics, computational, and materials challenges," Applied Physics Reviews, 2(4), p. 041304.

[31] Singh, B., and Sewell, N., "Knowledge based process planning and design for additive manufacturing (KARMA)," Proc. Innovative Developments in Virtual and Physical Prototyping-Proceedings of the 5th International Conference on Advanced Research and Rapid Prototyping, University of Exeter, Exeter, pp. 619-624.

[32] Kruth, J.-P., Vandenbroucke, B., Vaerenbergh, v. J., and Mercelis, P., 2005, "Benchmarking of different SLS/SLM processes as rapid manufacturing techniques."

[33] Xu, F., Wong, Y., and Loh, H., 2001, "Toward generic models for comparative evaluation and process selection in rapid prototyping and manufacturing," Journal of Manufacturing Systems, 19(5), pp. 283-296.

[34] Scaravetti, D., Dubois, P., and Duchamp, R., 2008, "Qualification of rapid prototyping tools: proposition of a procedure and a test part," The International Journal of Advanced Manufacturing Technology, 38(7-8), pp. 683-690.

[35] Thesis: Gomes, F. A. d. S., 2014, "Comparação de processos de fabrico aditivo que utilizam metais," M.Sc., Faculdade de Engenharia da Universidade do Porto, Porto.

[36] Kumar, S., and Kruth, J.-P., 2007, "Effect of bronze infiltration into laser sintered metallic parts," Materials & design, 28(2), pp. 400-407.

[37] Atzeni, E., and Salmi, A., 2012, "Economics of additive manufacturing for end-usable metal parts," The International Journal of Advanced Manufacturing Technology, 62(9-12), pp. 1147-1155.

[38] ARCAM, http://www.arcam.com/. [Accessed in June 1, 2016]

[39] Diegel, O., Singamneni, S., Reay, S., and Withell, A., 2010, "Tools for sustainable product design: additive manufacturing," Journal of Sustainable Development, 3(3), p. 68.

[40] Kellens, K., Dewulf, W., Deprez, W., Yasa, E., and Duflou, J., "Environmental analysis of SLM and SLS manufacturing processes," Proc. Proceedings of LCE2010 Conference, pp. 423-428.

[41] Mumtaz, K., and Hopkinson, N., 2010, "Selective laser melting of thin wall parts using pulse shaping," Journal of Materials Processing Technology, 210(2), pp. 279-287.

[42] Pan, Y., Zhao, X., Zhou, C., and Chen, Y., 2012, "Smooth surface fabrication in mask projection based stereolithography," Journal of Manufacturing Processes, 14(4), pp. 460-470.

[43] Ferrar, B., Mullen, L., Jones, E., Stamp, R., and Sutcliffe, C., 2012, "Gas flow effects on selective laser melting (SLM) manufacturing performance," Journal of Materials Processing Technology, 212(2), pp. 355-364.

[44] Santomaso, A., Lazzaro, P., and Canu, P., 2003, "Powder flowability and density ratios: the impact of granules packing," Chemical Engineering Science, 58(13), pp. 2857-2874.

[45] Sames, W., Medina, F., Peter, W., Babu, S., and Dehoff, R., "Effect of Process Control and Powder Quality on Inconel 718 Produced Using Electron Beam Melting," Proc. 8th International Symposium on Superalloy 718 and Derivatives, Wiley Online Library, pp. 409-423.

[46] Karlsson, J., Snis, A., Engqvist, H., and Lausmaa, J., 2013, "Characterization and comparison of materials produced by Electron Beam Melting (EBM) of two different Ti–6Al–4V powder fractions," Journal of Materials Processing Technology, 213(12), pp. 2109-2118.

[47] ASTM, 2013, "Standard test methods for flow rate of metal powders using the Hall Flowmeter funnel," B213-13, ASTM International, West Conshohocken, PA.

[48] ASTM, 2013, "Standard test method for apparent density of free-flowing metal powders using the Hall Flowmeter funnel," B212-13, ASTM International, West Conshohocken, PA.

[49] AP&C, 2014, "Designed for additive manufacturing", http://advancedpowders.com/our-plasma-atomized-powders/designed-for-additive-manufacturing/. [Accessed in June 3, 2016]

[50] Zekovic, S., Dwivedi, R., and Kovacevic, R., 2007, "Numerical simulation and experimental investigation of gas–powder flow from radially symmetrical nozzles in laser-based direct metal deposition," International Journal of Machine Tools and Manufacture, 47(1), pp. 112-123.

[51] Stecker, S., Lachenberg, K., Wang, H., and Salo, R., 2006, "Advanced Electron Beam Free Form Fabrication Methods & Technology," Session, 2, p. 12.

[52] Tang, H., Qian, M., Liu, N., Zhang, X., Yang, G., and Wang, J., 2015, "Effect of powder reuse times on additive manufacturing of Ti-6Al-4V by selective electron beam melting," Jom, 67(3), pp. 555-563.

[53] Murav'ev, V., Krupskii, R., Fizulakov, R., and Demyshev, P., 2008, "Effect of the quality of filler wire on the formation of pores in welding of titanium alloys," Welding International, 22(12), pp. 853-858.

[54] A. F. H. Kaplan, and J. Powell, 2011, "Spatter in laser welding," J. Laser Appl, 23.

[55] Santos, E. C., Shiomi, M., Osakada, K., and Laoui, T., 2006, "Rapid manufacturing of metal components by laser forming," International Journal of Machine Tools and Manufacture, 46(12), pp. 1459-1468.

[56] Li, S., Chen, G., Katayama, S., and Zhang, Y., 2014, "Relationship between spatter formation and dynamic molten pool during high-power deep-penetration laser welding," Applied Surface Science, 303, pp. 481-488.

[57] Eschey, C., Lutzmann, S., and Zaeh, M., 2009, "Examination of the powder spreading effect in Electron Beam Melting (EBM)," Solid Freeform Fabrication, Austin, TX, August, pp. 3-5.

[58] King, W. E., Barth, H. D., Castillo, V. M., Gallegos, G. F., Gibbs, J. W., Hahn, D. E., Kamath, C., and Rubenchik, A. M., 2014, "Observation of keyhole-mode laser melting in laser powder-bed fusion additive manufacturing," Journal of Materials Processing Technology, 214(12), pp. 2915-2925.

[59] Körner, C., Bauereiß, A., and Attar, E., 2013, "Fundamental consolidation mechanisms during selective beam melting of powders," Modelling and Simulation in Materials Science and Engineering, 21(8), p. 085011.

[60] Carter, L. N., Attallah, M. M., and Reed, R. C., 2012, "Laser Powder Bed Fabrication of Nickel-Base Superalloys: Influence of Parameters; Characterisation, Quantification and Mitigation of Cracking," Superalloys 2012, pp. 577-586.

[61] Syed, W. U. H., Pinkerton, A. J., and Li, L., 2006, "Combining wire and coaxial powder feeding in laser direct metal deposition for rapid prototyping," Applied surface science, 252(13), pp. 4803-4808.

[62] TWI, 2015, "What is hot cracking (solidification cracking)?", http://www.twi-global.com/technical-knowledge/faqs/

material-faqs/faq-what-is-hot-cracking-solidification-cracking/. [Accessed in June 6, 2016]

[63] Kempen, K., Thijs, L., Vrancken, B., Buls, S., Van Humbeeck, J., and Kruth, J., "PRODUCING CRACK-FREE, HIGH DENSITY M2 HSS PARTS BY SELECTIVE LASER MELTING: PRE-HEATING THE BASEPLATE," Proc. Solid Freeform Fabrication Symposium.

[64] Kruth, J.-P., Froyen, L., Van Vaerenbergh, J., Mercelis, P., Rombouts, M., and Lauwers, B., 2004, "Selective laser melting of iron-based powder," Journal of Materials Processing Technology, 149(1), pp. 616-622.

[65] Zäh, M. F., and Lutzmann, S., 2010, "Modelling and simulation of electron beam melting," Production Engineering, 4(1), pp. 15-23.

[66] Wu, A., LeBlanc, M., Kumar, M., Gallegos, G., Brown, D., and King, W., "Effect of Laser Scanning Pattern and Build Direction in Additive Manufacturing on Anisotropy, Porosity and Residual Stress," Proc. 2014 TMS Annual Meeting & Exhibition.

[67] Mercelis, P., and Kruth, J.-P., 2006, "Residual stresses in selective laser sintering and selective laser melting," Rapid Prototyping Journal, 12(5), pp. 254-265.

[68] Gnäupel-Herold, T., Slotwinski, J., and Moylan, S., "Neutron measurements of stresses in a test artifact produced by laser-based additive manufacturing," Proc. 40TH ANNUAL REVIEW OF PROGRESS IN QUANTITATIVE NONDESTRUCTIVE EVALUATION: Incorporating the 10th International Conference on Barkhausen Noise and Micromagnetic Testing, AIP Publishing, pp. 1205-1212.

[69] Rangaswamy, P., Holden, T., Rogge, R., and Griffith, M., 2003, "Residual stresses in components formed by the laserengineered net shaping (LENS®) process," The Journal of strain analysis for engineering design, 38(6), pp. 519-527.

[70] Sochalski-Kolbus, L., Payzant, E. A., Cornwell, P. A., Watkins, T. R., Babu, S. S., Dehoff, R. R., Lorenz, M., Ovchinnikova, O., and Duty, C., 2015, "Comparison of residual stresses in Inconel 718 simple parts made by electron beam melting and direct laser metal sintering," Metallurgical and Materials Transactions A, 46(3), pp. 1419-1432.

[71] Brice, C. A., and Hofmeister, W. H., 2013, "Determination of bulk residual stresses in electron beam additive-manufactured aluminum," Metallurgical and Materials Transactions A, 44(11), pp. 5147-5153.

[72] Ding, J., Colegrove, P., Mehnen, J., Ganguly, S., Almeida, P. S., Wang, F., and Williams, S., 2011, "Thermo-mechanical analysis of Wire and Arc Additive Layer Manufacturing process on large multi-layer parts," Computational Materials Science, 50(12), pp. 3315-3322.

[73] Wu, A. S., Brown, D. W., Kumar, M., Gallegos, G. F., and King, W. E., 2014, "An experimental investigation into additive manufacturing-induced residual stresses in 316L stainless steel," Metallurgical and Materials Transactions A, 45(13), pp. 6260-6270.

[74] Suresh, S., and Giannakopoulos, A., 1998, "A new method for estimating residual stresses by instrumented sharp indentation," Acta Materialia, 46(16), pp. 5755-5767.

[75] Song, B., Dong, S., Liu, Q., Liao, H., and Coddet, C., 2014, "Vacuum heat treatment of iron parts produced by selective laser melting: Microstructure, residual stress and tensile behavior," Materials & Design, 54, pp. 727-733.

[76] Prime, M. B., 2001, "Cross-sectional mapping of residual stresses by measuring the surface contour after a cut," Journal of Engineering Materials and Technology, 123(2), pp. 162-168.

[77] Moat, R., Pinkerton, A., Li, L., Withers, P., and Preuss, M., 2011, "Residual stresses in laser direct metal deposited Waspaloy," Materials Science and Engineering: A, 528(6), pp. 2288-2298.

[78] Zaeh, M. F., and Branner, G., 2010, "Investigations on residual stresses and deformations in selective laser melting," Production Engineering, 4(1), pp. 35-45.

[79] Prabhakar, P., Sames, W., Dehoff, R., and Babu, S., 2015, "Computational modeling of residual stress formation during the electron beam melting process for Inconel 718," Additive Manufacturing, 7, pp. 83-91.

[80] Brandl, E., and Greitemeier, D., 2012, "Microstructure of additive layer manufactured Ti–6Al–4V after exceptional post heat treatments," Materials Letters, 81, pp. 84-87.

[81] Brandl, E., Schoberth, A., and Leyens, C., 2012, "Morphology, microstructure, and hardness of titanium (Ti-6Al-4V) blocks deposited by wire-feed additive layer manufacturing (ALM)," Materials Science and Engineering: A, 532, pp. 295-307.

[82] Amato, K., Gaytan, S., Murr, L., Martinez, E., Shindo, P., Hernandez, J., Collins, S., and Medina, F., 2012, "Microstructures and mechanical behavior of Inconel 718 fabricated by selective laser melting," Acta Materialia, 60(5), pp. 2229-2239.

[83] Cao, J., Liu, F., Lin, X., Huang, C., Chen, J., and Huang, W., 2013, "Effect of overlap rate on recrystallization behaviors of Laser Solid Formed Inconel 718 superalloy," Optics & Laser Technology, 45, pp. 228-235.

[84] Blackwell, P., 2005, "The mechanical and microstructural characteristics of laser-deposited IN718," Journal of materials processing technology, 170(1), pp. 240-246.

[85] Unocic, K. A., Kolbus, L. M., Dehoff, R. R., Dryepondt, S. N., and Pint, B. A., 2014, "High-temperature performance of N07718 processed by additive manufacturing," NACE corrosion 2014.

[86] Kim, Y., Kim, E.-P., Song, Y.-B., Lee, S. H., and Kwon, Y.-S., 2014, "Microstructure and mechanical properties of hot isostatically pressed Ti–6Al–4V alloy," Journal of Alloys and Compounds, 603, pp. 207-212.

[87] Łyczkowska, E., Szymczyk, P., Dybała, B., and Chlebus, E., 2014, "Chemical polishing of scaffolds made of Ti–6Al–7Nb alloy by additive manufacturing," Archives of Civil and Mechanical Engineering, 14(4), pp. 586-594.

[88] Dehoff, R. R., Tallman, C., Duty, C. E., Peter, W. H., Yamamoto, Y., Chen, W., and Blue, C. A., 2013, "Case study: additive manufacturing of aerospace brackets," Advanced Materials and Processes, 171(3).

[89] Lütjering, G., and Williams, J. C., 2007, Titanium, Springer, New York.

[90] Pederson, R., 2002, "Microstructure and Phase transformation of Ti-6Al-4V."

[91] Sieniawski, J., Ziaja, W., Kubiak, K., and Motyka, M., 2013, "Microstructure and mechanical properties of high strength two-phase titanium alloys," Titanium Alloys-Advances in Properties Control, pp. 69-80.

[92] Boivineau, M., Cagran, C., Doytier, D., Eyraud, V., Nadal, M.-H., Wilthan, B., and Pottlacher, G., 2006, "Thermophysical properties of solid and liquid Ti-6Al-4V (TA6V) alloy," International journal of thermophysics, 27(2), pp. 507-529.

[93] TIMET, 2000, "TIMETAL ® 6-4, 6-4 ELI & 6-4-.1 Ru Datashhet"

[94] Schrock, D. J., Kang, D., Bieler, T. R., and Kwon, P., 2014, "Phase dependent tool wear in turning Ti-6Al-4V using polycrystalline diamond and carbide inserts," Journal of manufacturing science and engineering, 136(4), p. 041018.

[95] Albrecht, J., and Lütjering, G., 2000, "Microstructure and mechanical properties of titanium alloys," Titanium'99: Science and Technology, pp. 363-374.

[96] Seifi, M., Salem, A., Beuth, J., Harrysson, O., and Lewandowski, J. J., 2016, "Overview of materials qualification needs for metal additive manufacturing," JOM, 68(3), pp. 747-764.

[97] ISO/ASTM, 2013, "Standard terminology for additive manufacturing-coordinate systems and test methodologies," ASTM/ISO Stand. 52921.

[98] Moylan, S., Land, J., and Possolo, A., "Additive Manufacturing - Round Robin Protocols: a pilot study."

[99] Moylan, S., Brown, C. U., and Slotwinski, J., 2016, "Recommended Protocol for Round-Robin Studies in Additive Manufacturing," Journal of testing and evaluation, 44(2), pp. 1009-1018.

[100] Dutta, B., and Froes, F. H. S., 2015, "The additive manufacturing (AM) of titanium alloys," Titanium Powder Metallurgy: Science, Technology and Applications, p. 447.

[101] Gockel, J., Beuth, J., and Taminger, K., 2014, "Integrated control of solidification microstructure and melt pool dimensions in electron beam wire feed additive manufacturing of Ti-6Al-4V," Additive Manufacturing, 1, pp. 119-126.

[102] Beuth, J., Fox, J., Gockel, J., Montgomery, C., Yang, R., Qiao, H., Soylemez, E., Reeseewatt, P., Anvari, A., and Narra, S., "Process mapping for qualification across multiple direct metal additive manufacturing processes," Proc. Proceedings of SFF Symposium., Austin, TX, Aug, pp. 12-14.

[103] Gockel, J., and Beuth, J., 2013, "Understanding Ti-6Al-4V microstructure control in additive manufacturing via process maps," Solid Freeform Fabrication Proceedings, Austin, TX, Aug, pp. 12-14.

[104] Nassar, A. R., Keist, J. S., Reutzel, E. W., and Spurgeon, T. J., 2015, "Intra-layer closed-loop control of build plan during directed energy additive manufacturing of Ti–6Al–4V," Additive Manufacturing, 6, pp. 39-52.

[105] Soylemez, E., Beuth, J. L., and Taminger, K., "Controlling melt pool dimensions over a wide range of material deposition rates in electron beam additive manufacturing," Proc. Proceedings of 21st Solid Freeform Fabrication Symposium, Austin, TX, Aug, pp. 9-11.

[106] Montgomery, C., Beuth, J., Sheridan, L., and Klingbeil, N., "Process Mapping of Inconel 625 in Laser Powder Bed Additive Manufacturing."

[107] Seifi, M., Christiansen, D., Beuth, J., Harrysson, O., and Lewandowski, J. J., "Process Mapping, Fracture and Fatigue behavior of Ti-6Al-4V produced by EBM Additive Manufacturing."

[108] Kobryn, P., and Semiatin, S., 2001, "The laser additive manufacture of Ti-6Al-4V," JOM, 53(9), pp. 40-42.

[109] Kobryn, P., and Semiatin, S., 2003, "Microstructure and texture evolution during solidification processing of Ti–6Al–4V," Journal of Materials Processing Technology, 135(2), pp. 330-339.

[110] Greitemeier, D., Dalle Donne, C., Syassen, F., Eufinger, J., and Melz, T., 2015, "Effect of surface roughness on fatigue performance of additive manufactured Ti-6Al-4V," Materials Science and Technology, p. 1743284715Y. 0000000053.

[111] Edwards, P., O'Conner, A., and Ramulu, M., 2013, "Electron beam additive manufacturing of titanium components: Properties and performance," Journal of Manufacturing Science and Engineering, 135(6), p. 061016.

[112] Ackelid, U., and Svensson, M., "Additive manufacturing of dense metal parts by electron beam melting," Proc. Materials Science and Technology Conference, pp. 2711-2719.

[113] Tan, X., Kok, Y., Tan, Y. J., Descoins, M., Mangelinck, D., Tor, S. B., Leong, K. F., and Chua, C. K., 2015, "Graded microstructure and mechanical properties of additive manufactured Ti–6Al–4V via electron beam melting," Acta Materialia, 97, pp. 1-16.

[114] Lu, S., Tang, H., Ning, Y., Liu, N., StJohn, D., and Qian, M., 2015, "Microstructure and Mechanical Properties of Long Ti-6Al-4V Rods Additively Manufactured by Selective Electron Beam Melting Out of a Deep Powder Bed and the Effect of Subsequent Hot Isostatic Pressing," Metallurgical and Materials Transactions A, 46(9), pp. 3824-3834.

[115] Rodriguez, O. L., Allison, P. G., Whittington, W. R., Francis, D. K., Rivera, O., Chou, K., Gong, X., Butler, T., and Burroughs, J. F., 2015, "Dynamic tensile behavior of electron beam additive manufactured Ti6Al4V," Materials Science and Engineering: A, 641, pp. 323-327.

[116] Mohammadhosseini, A., Fraser, D., Masood, S., and Jahedi, M., 2013, "Microstructure and mechanical properties of Ti–6Al–4V manufactured by electron beam melting process," Materials Research Innovations, 17(sup2), pp. s106-s112.

[117] Hrabe, N., and Quinn, T., 2013, "Effects of processing on microstructure and mechanical properties of a titanium alloy (Ti–6Al–4V) fabricated using electron beam melting (EBM), Part 2: energy input, orientation, and location," Materials Science and Engineering: A, 573, pp. 271-277.

[118] Rafi, H., Karthik, N., Gong, H., Starr, T. L., and Stucker, B. E., 2013, "Microstructures and mechanical properties of Ti6Al4V parts fabricated by selective laser melting and electron beam melting," Journal of materials engineering and performance, 22(12), pp. 3872-3883.

[119] Rafi, H. K., Karthik, N., Starr, T. L., and Stucker, B. E., "Mechanical property evaluation of Ti-6Al-4V parts made using electron beam melting," Proc. Proceedings of the Solid Freeform Fabrication Symposium, pp. 526-535.

[120] Murr, L., Esquivel, E., Quinones, S., Gaytan, S., Lopez, M., Martinez, E., Medina, F., Hernandez, D., Martinez, E., and Martinez, J., 2009, "Microstructures and mechanical properties of electron beam-rapid manufactured Ti–6Al–4V biomedical prototypes compared to wrought Ti–6Al–4V," Materials characterization, 60(2), pp. 96-105.

[121] Facchini, L., Magalini, E., Robotti, P., and Molinari, A., 2009, "Microstructure and mechanical properties of Ti-6Al-4V produced by electron beam melting of pre-alloyed powders," Rapid Prototyping Journal, 15(3), pp. 171-178.

[122] Koike, M., Martinez, K., Guo, L., Chahine, G., Kovacevic, R., and Okabe, T., 2011, "Evaluation of titanium alloy fabricated using electron beam melting system for dental applications," Journal of Materials Processing Technology, 211(8), pp. 1400-1408.

[123] Christensen, A., Kircher, R., and Lippincott, A., "Qualification of electron beam melted (EBM) Ti6Al4V-ELI for orthopaedic applications," Proc. Medical Device Materials IV: Proceedings of the Materials and Processes for Medical Devices Conference, pp. 48-53.

[124] McLouth, T., Chang, Y.-W., Wooten, J., and Yang, J.-M., 2015, "The Effects of Electron Beam Melting on the Microstructure and Mechanical Properties of Ti-6Al-4V and Gamma-TiAl," Microscopy and Microanalysis, 21(S3), pp. 1177-1178.

[125] Gong, H., Rafi, K., Gu, H., Ram, G. J., Starr, T., and Stucker, B., 2015, "Influence of defects on mechanical properties of Ti–6Al–4V components produced by selective laser melting and electron beam melting," Materials & Design, 86, pp. 545-554.

[126] Larsson, M., Lindhe, U., and Harrysson, O., "Rapid Manufacturing With Electron Beam Melting (EBM)—A Manufacturing Revolution?," Proc. Solid Freeform Fabrication Symposium, Austin, TX, August, pp. 4-6.

[127] Rekedal, K. D., and Liu, D., "Fatigue life of selective laser melted and hot isostatically pressed Ti–6Al–4V absent of surface machining," Proc. Proceedings of the 56th AIAA/ASCE/AHS/ASC Structures, Structural Dynamics, and Materials Conference, Kissimmee, FL.

[128] Cain, V., Thijs, L., Van Humbeeck, J., Van Hooreweder, B., and Knutsen, R., 2015, "Crack propagation and fracture toughness of Ti6Al4V alloy produced by selective laser melting," Additive Manufacturing, 5, pp. 68-76.

[129] Kasperovich, G., and Hausmann, J., 2015, "Improvement of fatigue resistance and ductility of TiAl6V4 processed by selective laser melting," Journal of Materials Processing Technology, 220, pp. 202-214.

[130] Edwards, P., and Ramulu, M., 2014, "Fatigue performance evaluation of selective laser melted Ti–6Al–4V," Materials Science and Engineering: A, 598, pp. 327-337.

[131] Leuders, S., Lieneke, T., Lammers, S., Tröster, T., and Niendorf, T., 2014, "On the fatigue properties of metals manufactured by selective laser melting–The role of ductility," Journal of Materials Research, 29(17), pp. 1911-1919.

[132] Simonelli, M., Tse, Y., and Tuck, C., 2014, "Effect of the build orientation on the Mechanical Properties and Fracture Modes of SLM Ti–6Al–4V," Materials Science and Engineering: A, 616, pp. 1-11.

[133] Leuders, S., Thöne, M., Riemer, A., Niendorf, T., Tröster, T., Richard, H., and Maier, H., 2013, "On the mechanical behaviour of titanium alloy TiAl6V4 manufactured by selective laser melting: Fatigue resistance and crack growth performance," International Journal of Fatigue, 48, pp. 300-307.

[134] Simonelli, M., Tse, Y. Y., and Tuck, C., 2014, "The formation of α+ β microstructure in as-fabricated selective laser melting of Ti–6Al–4V," Journal of Materials Research, 29(17), pp. 2028-2035.

[135] Vrancken, B., Thijs, L., Kruth, J.-P., and Van Humbeeck, J., 2012, "Heat treatment of Ti6Al4V produced by selective laser melting: microstructure and mechanical properties," Journal of Alloys and Compounds, 541, pp. 177-185.

[136] Facchini, L., Magalini, E., Robotti, P., Molinari, A., Höges, S., and Wissenbach, K., 2010, "Ductility of a Ti-6Al-4V alloy produced by selective laser melting of prealloyed powders," Rapid Prototyping Journal, 16(6), pp. 450-459.

[137] Vandenbroucke, B., and Kruth, J.-P., 2007, "Selective laser melting of biocompatible metals for rapid manufacturing of medical parts," Rapid Prototyping Journal, 13(4), pp. 196-203.

[138] Vilaro, T., Colin, C., and Bartout, J.-D., 2011, "As-fabricated and heat-treated microstructures of the Ti-6Al-4V alloy processed by selective laser melting," Metallurgical and Materials Transactions A, 42(10), pp. 3190-3199.

[139] Mertens, A., Reginster, S., Paydas, H., Contrepois, Q., Dormal, T., Lemaire, O., and Lecomte-Beckers, J., 2014, "Mechanical properties of alloy Ti–6Al–4V and of stainless steel 316L processed by selective laser melting: influence of out-of-equilibrium microstructures," Powder Metallurgy, 57(3), pp. 184-189.

[140] Hollander, D. A., Von Walter, M., Wirtz, T., Sellei, R., Schmidt-Rohlfing, B., Paar, O., and Erli, H.-J., 2006, "Structural, mechanical and in vitro characterization of individually structured Ti–6Al–4V produced by direct laser forming," Biomaterials, 27(7), pp. 955-963.

[141] Qiu, C., Adkins, N. J., and Attallah, M. M., 2013, "Microstructure and tensile properties of selectively laser-melted and of HIPed laser-melted Ti–6Al–4V," Materials Science and Engineering: A, 578, pp. 230-239.

[142] Kobryn, P., and Semiatin, S., "Mechanical properties of laser-deposited Ti-6Al-4V," Proc. Solid Freeform Fabrication Proceedings, Austin, pp. 6-8.

[143] Qiu, C., Ravi, G., Dance, C., Ranson, A., Dilworth, S., and Attallah, M. M., 2015, "Fabrication of large Ti–6Al–4V structures by direct laser deposition," Journal of Alloys and Compounds, 629, pp. 351-361.

[144] Yu, J., Rombouts, M., Maes, G., and Motmans, F., 2012, "Material properties of Ti6Al4V parts produced by laser metal deposition," Physics Procedia, 39, pp. 416-424.

[145] Zhang, S., Lin, X., Chen, J., and Huang, W., 2009, "Heat-treated microstructure and mechanical properties of laser solid forming Ti-6Al-4V alloy," Rare metals, 28(6), pp. 537-544.

[146] Alcisto, J., Enriquez, A., Garcia, H., Hinkson, S., Steelman, T., Silverman, E., Valdovino, P., Gigerenzer, H., Foyos, J., and Ogren, J., 2011, "Tensile properties and microstructures of laser-formed Ti-6Al-4V," Journal of materials engineering and performance, 20(2), pp. 203-212.

[147] Dinda, G., Song, L., and Mazumder, J., 2008, "Fabrication of Ti-6Al-4V scaffolds by direct metal deposition," Metallurgical and Materials Transactions A, 39(12), pp. 2914-2922.

[148] Carroll, B. E., Palmer, T. A., and Beese, A. M., 2015, "Anisotropic tensile behavior of Ti–6Al–4V components fabricated with directed energy deposition additive manufacturing," Acta Materialia, 87, pp. 309-320.

[149] Lewis, G. K., and Schlienger, E., 2000, "Practical considerations and capabilities for laser assisted direct metal deposition," Materials & Design, 21(4), pp. 417-423.

[150] Griffith, M. L., Ensz, M. T., Puskar, J. D., Robino, C. V., Brooks, J. A., Philliber, J. A., Smugeresky, J. E., and Hofmeister, W., "Understanding the microstructure and properties of components fabricated by laser engineered net shaping (LENS)," Proc. MRS proceedings, Cambridge Univ Press, p. 9.

[151] Zhai, Y., Galarraga, H., and Lados, D. A., 2015, "Microstructure evolution, tensile properties, and fatigue damage mechanisms in Ti-6Al-4V alloys fabricated by two additive manufacturing techniques," Procedia Engineering, 114, pp. 658-666.

[152] Arcella, F. G., and Froes, F., 2000, "Producing titanium aerospace components from powder using laser forming," Jom, 52(5), pp. 28-30.

[153] Sterling, A. J., Torries, B., Shamsaei, N., Thompson, S. M., and Seely, D. W., 2016, "Fatigue behavior and failure mechanisms of direct laser deposited Ti–6Al–4V," Materials Science and Engineering: A, 655, pp. 100-112.

[154] Lewandowski, J. J., and Seifi, M., 2016, "Metal Additive Manufacturing: A Review of Mechanical Properties," Annual Review of Materials Research, 46(1).

[155] Wolk, J., "Distribution Statement A – Approved for Public Release ADDITIVE MANUFACTURING," Naval Surface Warfare Center Carderock Division.

[156] EOS, "EOSINT M 280", http://www.eos.info/systems_solutions/metal/systems_equipment/eosint_m280. [Accessed in June 28, 2016]

[157] Gianola, D., and Sharpe, W., 2004, "Techniques for testing thin films in tension," Experimental techniques, 28(5), pp. 23-27.

[158] Sharpe Jr, W., Pulskamp, J., Gianola, D., Eberl, C., Polcawich, R., and Thompson, R., 2007, "Strain measurements of silicon dioxide microspecimens by digital imaging processing," Experimental Mechanics, 47(5), pp. 649-658.

[159] Eberl, C., Gianola, D., Wang, X., He, M., Evans, A., and Hemker, K., 2011, "A method for in situ measurement of the elastic behavior of a columnar thermal barrier coating," Acta Materialia, 59(9), pp. 3612-3620.

[160] Eberl, C., Wang, X., Gianola, D. S., Nguyen, T. D., He, M. Y., Evans, A. G., and Hemker, K. J., 2011, "In situ measurement of the toughness of the interface between a thermal barrier coating and a Ni alloy," Journal of the American Ceramic Society, 94(s1).

[161] Zupan, M., and Hemker, K., 1998, "Tension and compression testing of single-crystalline gamma Ti-55.5 pct Al," Metallurgical and Materials Transactions A, 29(1), pp. 65-71.

[162] Cheng, C. L., 2008, Mechanical and Microstructural Characterization of Copper Microsamples after Cold Drawing, ProQuest.

[163] LaVan, D., and Sharpe Jr, W., 1999, "Tensile testing of microsamples," Experimental mechanics, 39(3), pp. 210-216.

[164] Nimer, S. M., 2011, Local property characterization of friction stir welded titanium 5111, University of Maryland, Baltimore County.

[165] Nimer, S., Wolk, J., and Zupan, M., 2014, "Location and Orientation Specific Material Property Evaluation of Friction Stir Welded Ti-5111: A Microsample Approach," Advanced Engineering Materials, 16(4), pp. 452-458.

[166] Nimer, S., Wolk, J., and Zupan, M., 2013, "Local property characterization of friction stir welded Ti-5111: Transverse orientation measurements," Acta Materialia, 61(8), pp. 3050-3059.

[167] Thesis: Nimer, S., 2016, "Microscale Mechanical experiments at elevated temperatures: system development and material characterization," Doctor of Philosophy in Mechanical Engineering, University of Maryland, Baltimore County, Baltimore, MD.

[168] Computer Program: Solutions, C., VIC-2D, 2009,

[169] Personal Communication: Naval Air Station Patuxent River, and Micro Materials Characterization Lab, 2016, 21967 Cuddihy Rd, Patuxent River, MD 20670

APPENDIX A: Microstructures

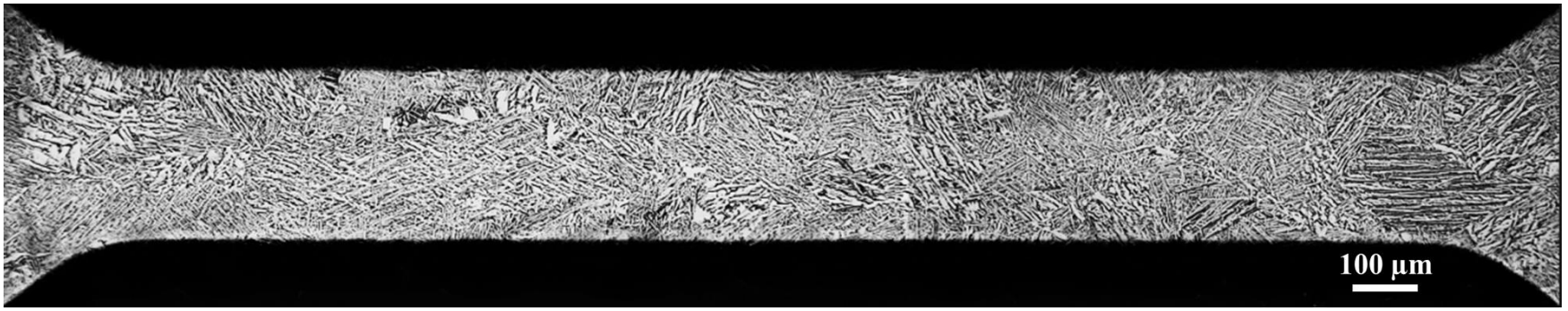

Microsample #4 direction d1 (E = 113.23 GPa | $\sigma_{0.2}$ = 881.25 MPa | UTS = 959.79 MPa | ε_F = 13.56%)

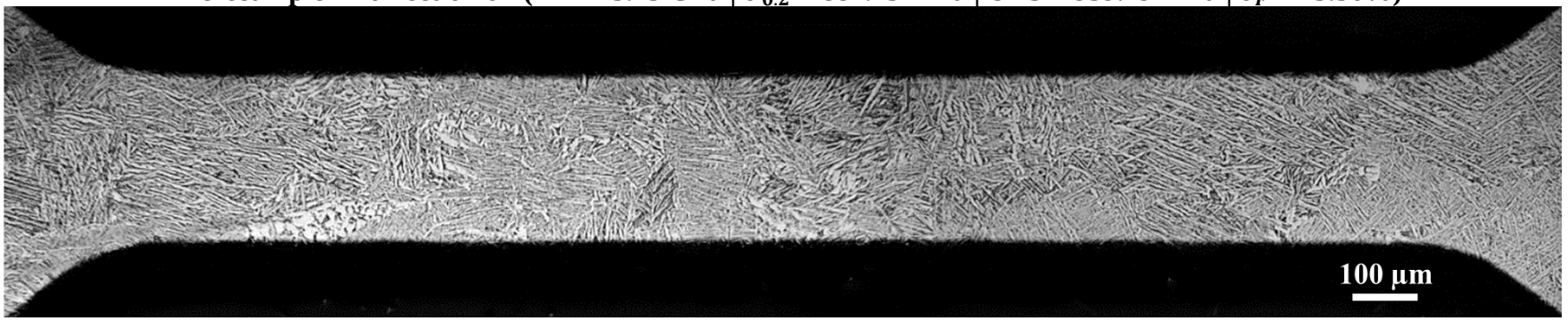

Microsample #5 direction d1 (E = 122.68 GPa | $\sigma_{0.2}$ = 960.00 MPa | UTS = 1084.17 MPa | ε_F = 12.64%)

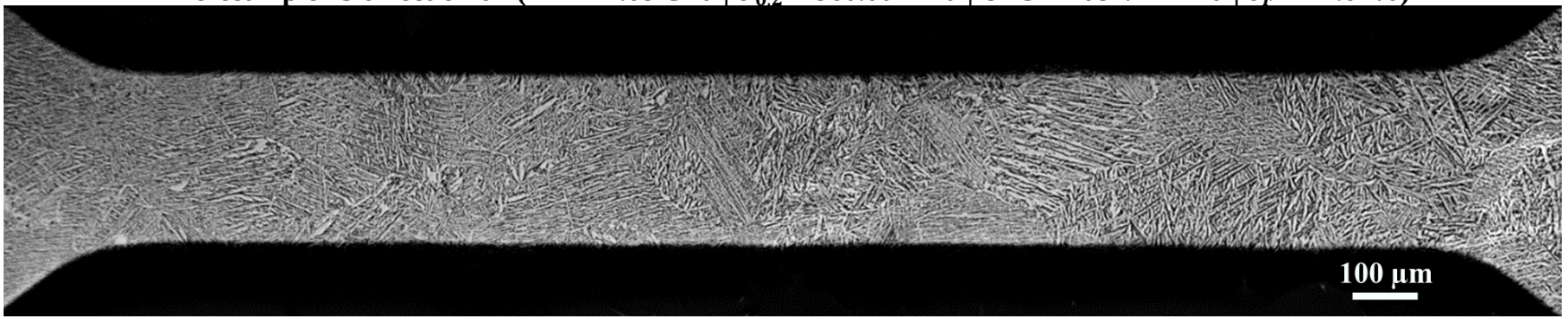

Microsample #6 direction d1 (E = 115.55 GPa | $\sigma_{0.2}$ = 975.00 MPa | UTS = 1067.31 MPa | ε_F = 12.83%)

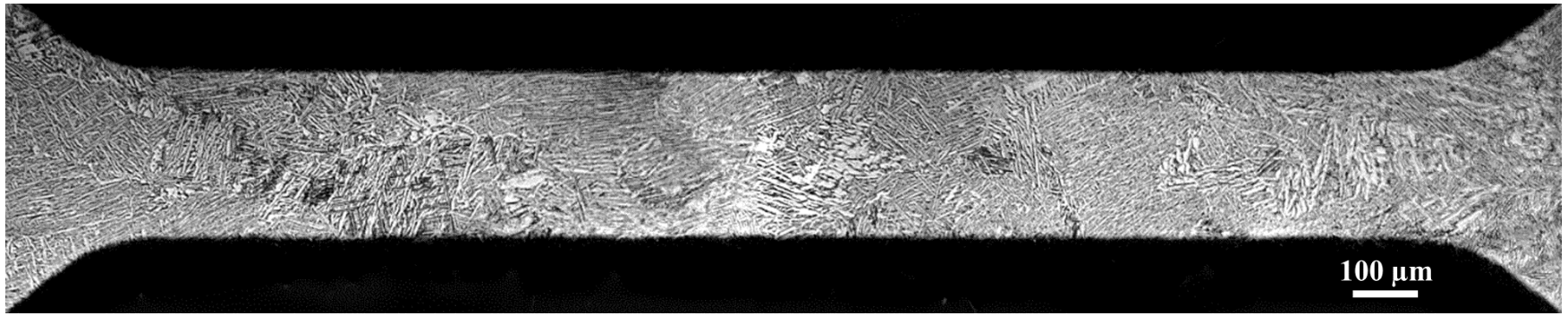

Microsample #7 direction d1 (E = 118.55 GPa | $\sigma_{0.2}$ = 962.50 MPa | UTS = 1048.68 MPa | ε_F = 13.01%)

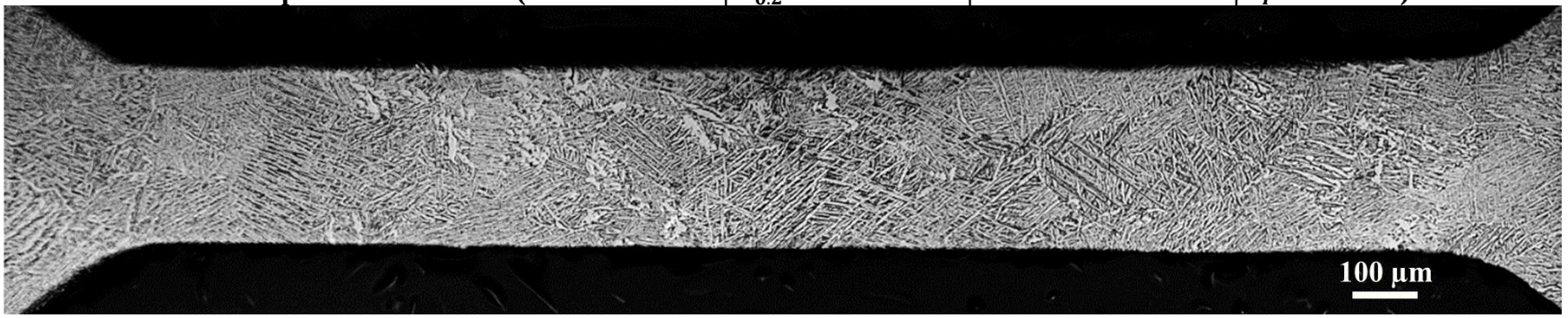

Microsample #8 direction d1 (E = 111.94 GPa | $\sigma_{0.2}$ = 975.50 MPa | UTS = 1023.04 MPa | ε_F = 15.31%)

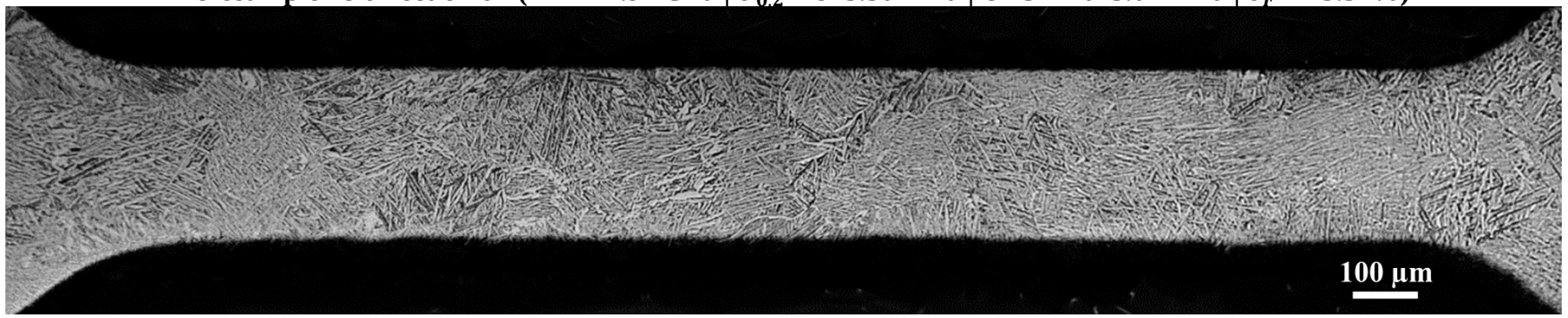

Microsample #9 direction d1 (E = 109.59 GPa | $\sigma_{0.2}$ = 927.50 MPa | UTS = 1011.77 MPa | ε_F = 12.17%)

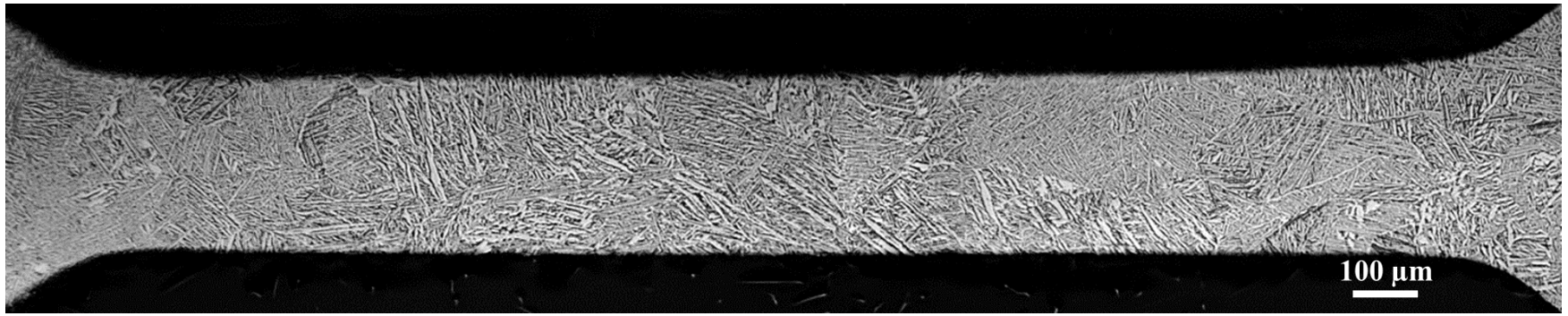

Microsample #10 direction d1 (E = 118.35 GPa | $\sigma_{0.2}$ = 965.00 MPa | UTS = 1041.07 MPa | ε_F = 16.00%)

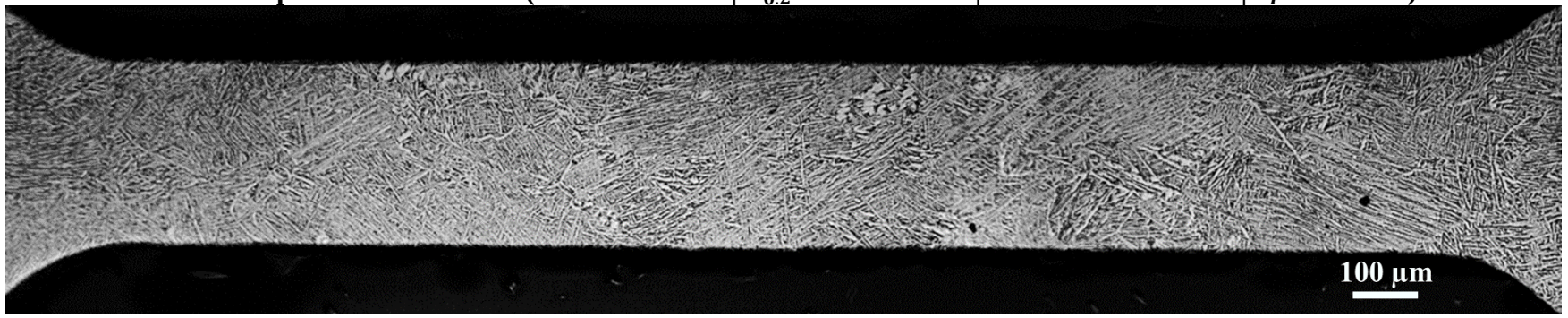

Microsample #11 direction d1 (E = 100.43 GPa | $\sigma_{0.2}$ = 975.00 MPa | UTS = 1021.17 MPa | ε_F = 14.61%)

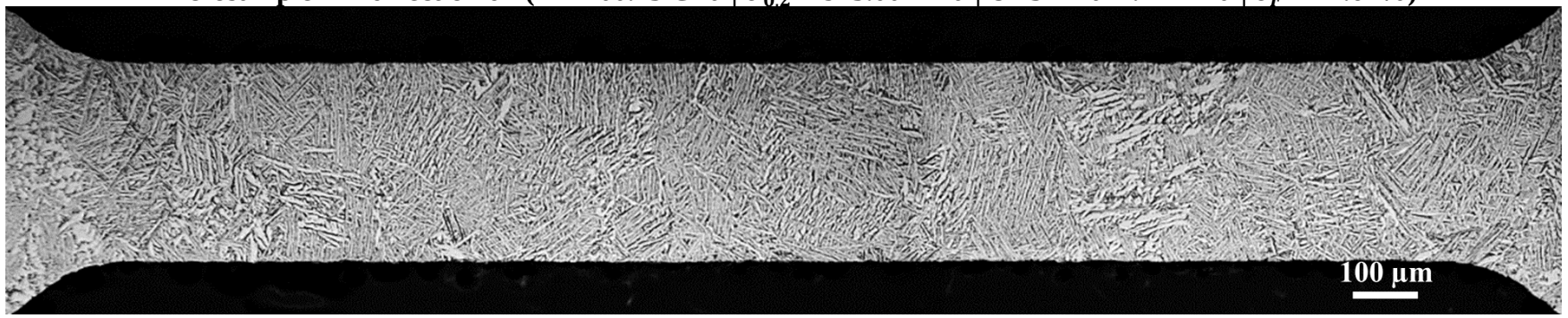

Microsample #4 direction d2 (E = 115.26 GPa | $\sigma_{0.2}$ = 890.00 MPa | UTS = 1013.44 MPa | ε_F = 8.41%)

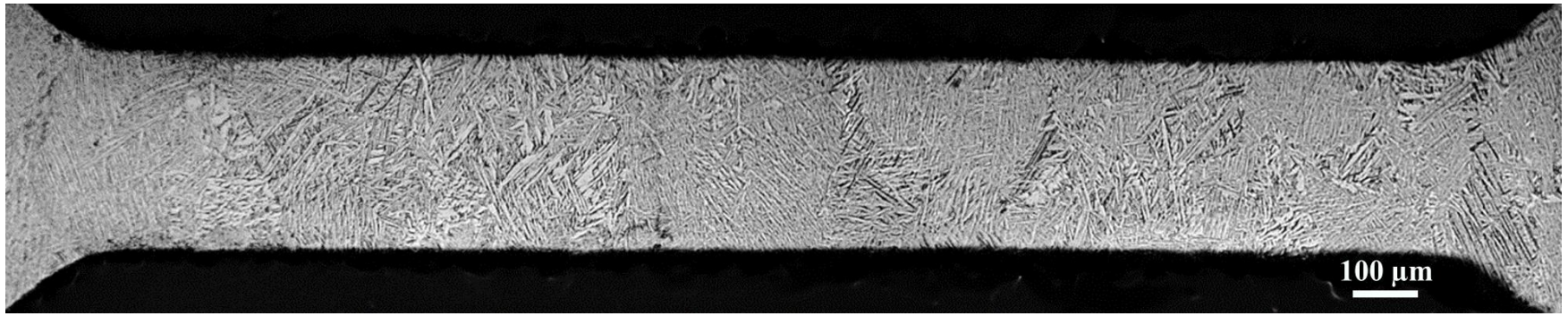

Microsample #5 direction d2 (E = 117.83 GPa | $\sigma_{0.2}$ = 875.00 MPa | UTS = 962.43 MPa | ε_F = 12.37%)

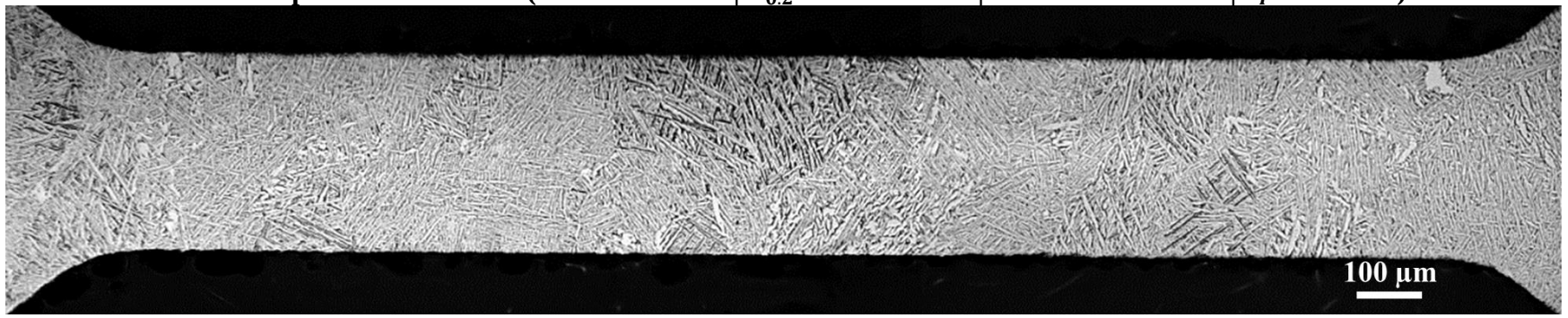

Microsample #6 direction d2 (E = 100.07 GPa | $\sigma_{0.2}$ = 874.50 MPa | UTS = 941.19 MPa | ε_F = 11.51%)

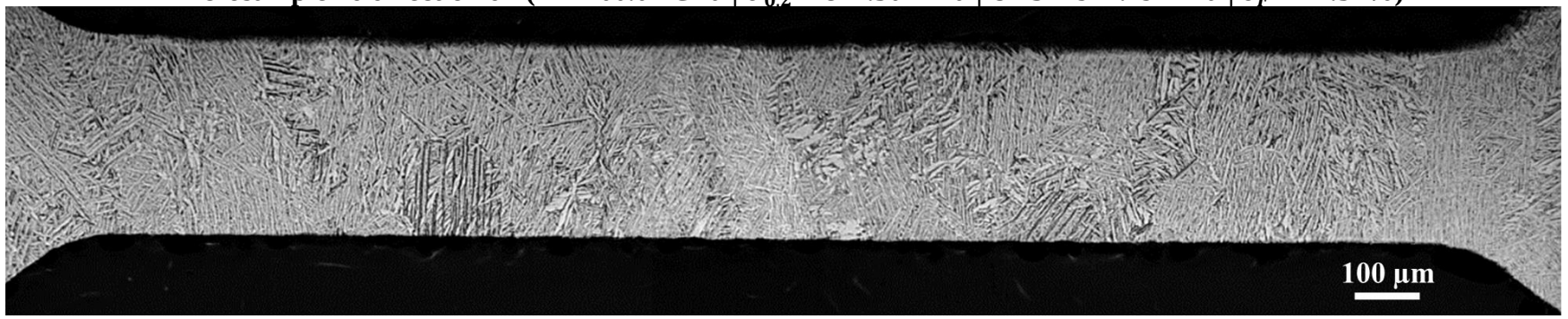

Microsample #7 direction d2 (E = 111.48 GPa | $\sigma_{0.2}$ = 862.50 MPa | UTS = 969.84 MPa | ε_F = 10.40%)

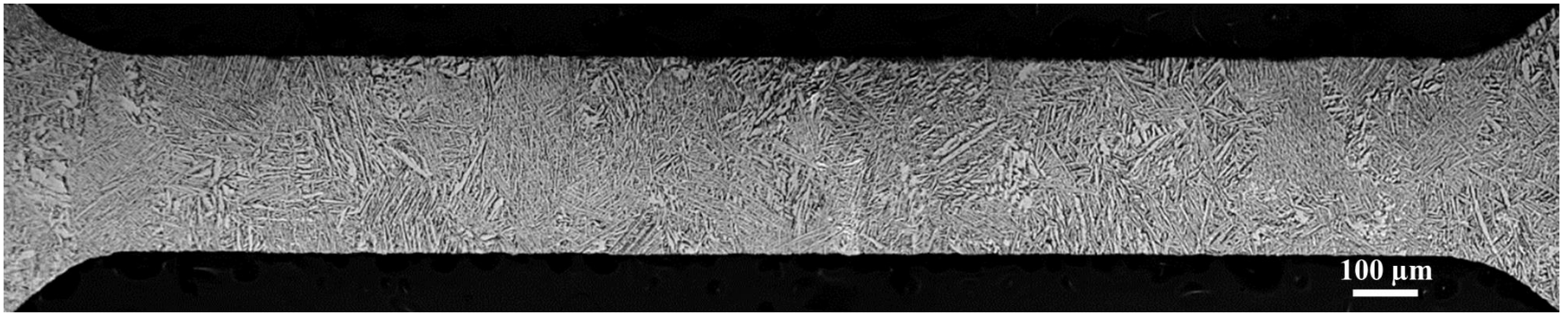

Microsample #8 direction d2 (E = 124.98 GPa | $\sigma_{0.2}$ = 865.00 MPa | UTS = 980.52 MPa | ε_F = 12.64%)

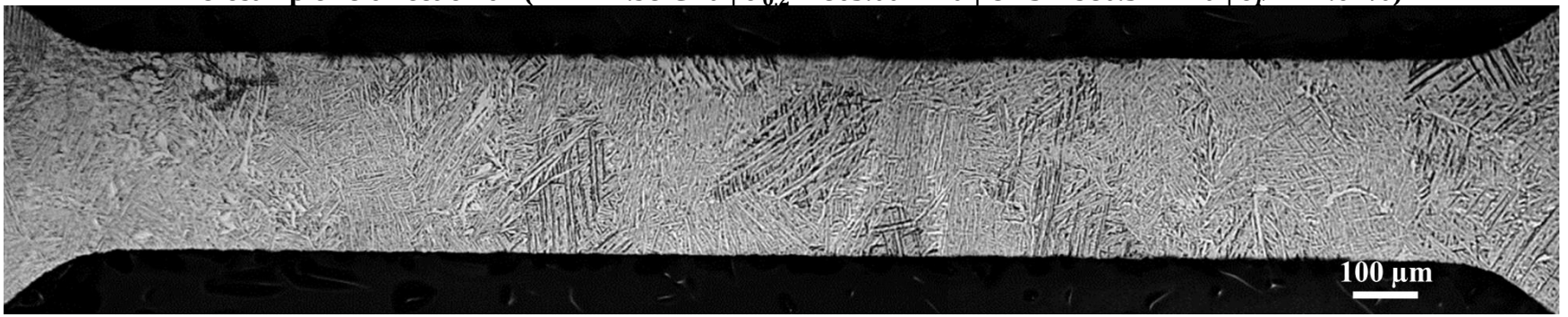

Microsample #9 direction d2 (E = 121.16 GPa | $\sigma_{0.2}$ = 877.50 MPa | UTS = 980.02 MPa | ε_F = 12.59%)

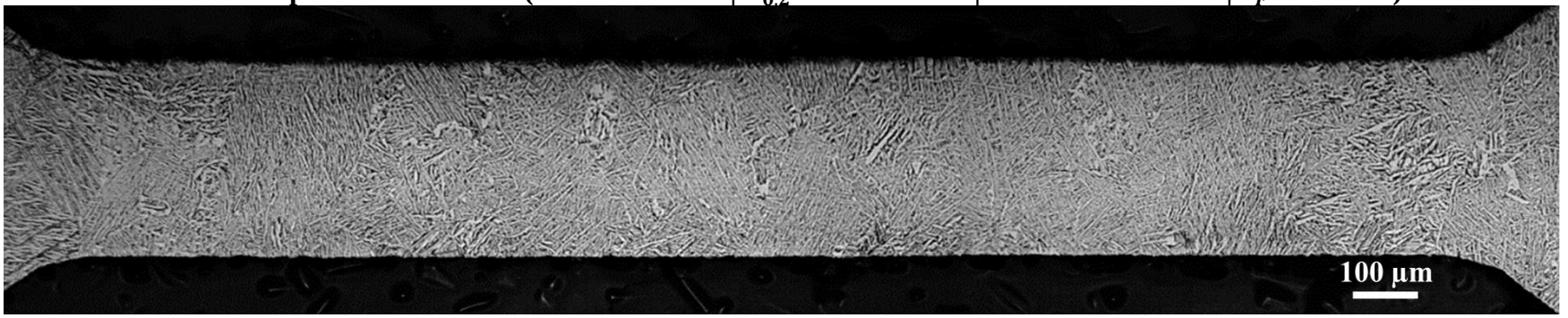

Microsample #10 direction d2 (E = 117.30 GPa | $\sigma_{0.2}$ = 750.00 MPa | UTS = 858.41 MPa | ε_F = 12.26%)

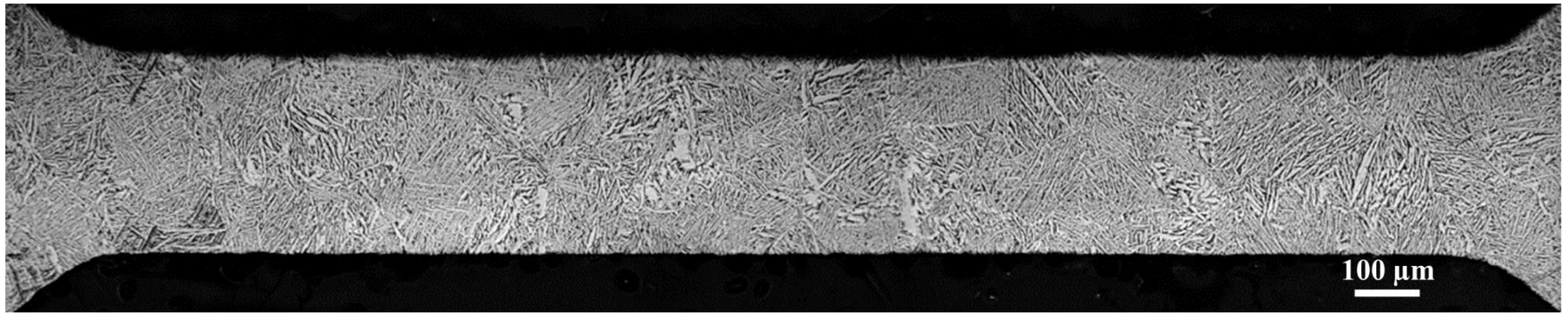

Microsample #11 direction d2 (E = 115.33 GPa | $\sigma_{0.2}$ = 825.00 MPa | UTS = 943.93 MPa | ε_F = 10.9)

APPENDIX B: Fracture Surfaces

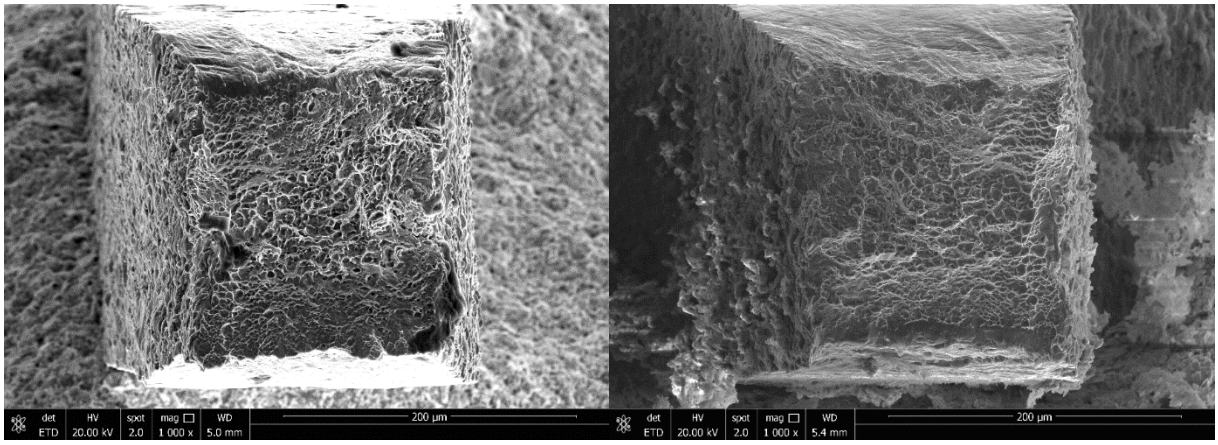

Microsample #1 direction d1 (E = 115.41 GPa | $\sigma_{0.2}$ = 900.00 MPa | UTS = 1006.76 MPa | ε_F = 15.51%)

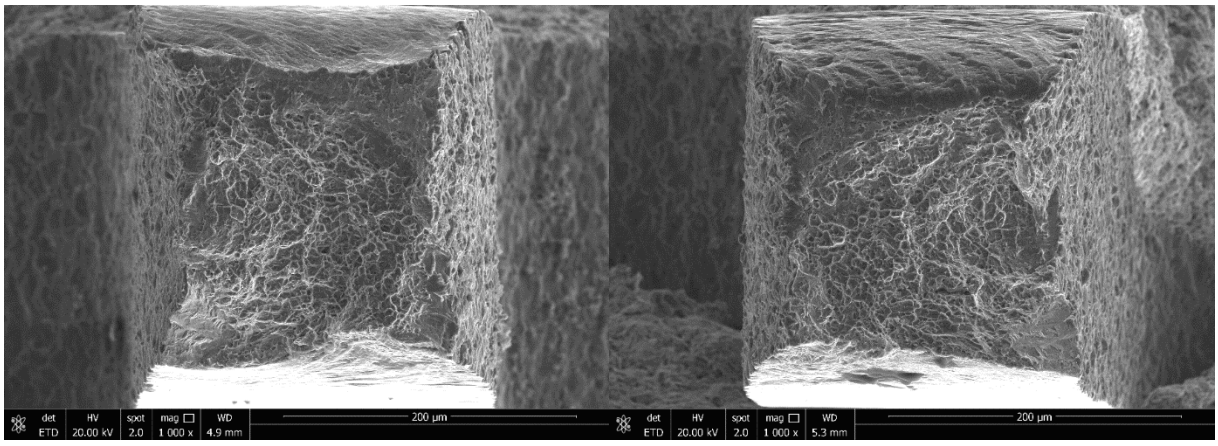

Microsample #2 direction d1 (E = 116.37 GPa | $\sigma_{0.2}$ = 930.00 MPa | UTS = 1021.96 MPa | ε_F = 11.46%)

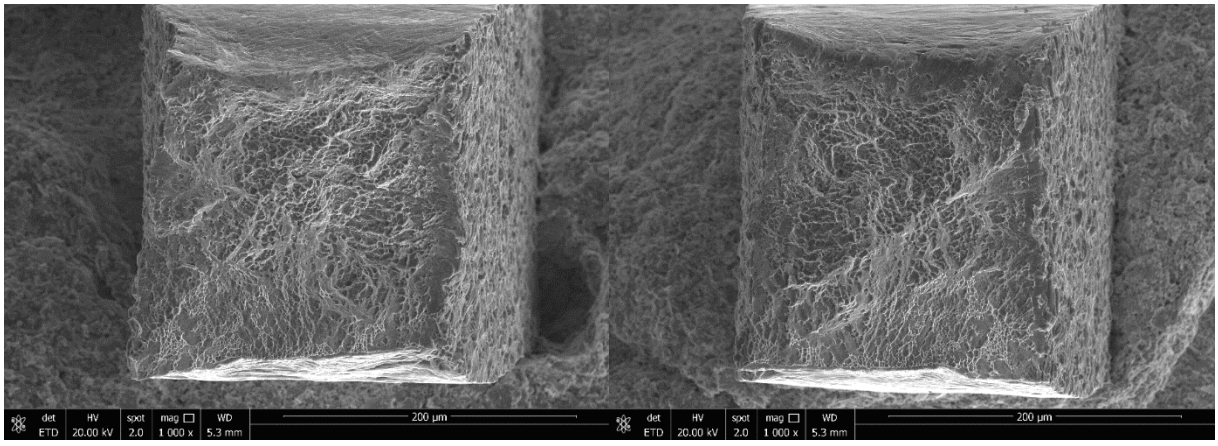

Microsample #3 direction d1 (E = 119.50 GPa | $\sigma_{0.2}$ = 925.00 MPa | UTS = 1020.67 MPa | ε_F = 13.03%)

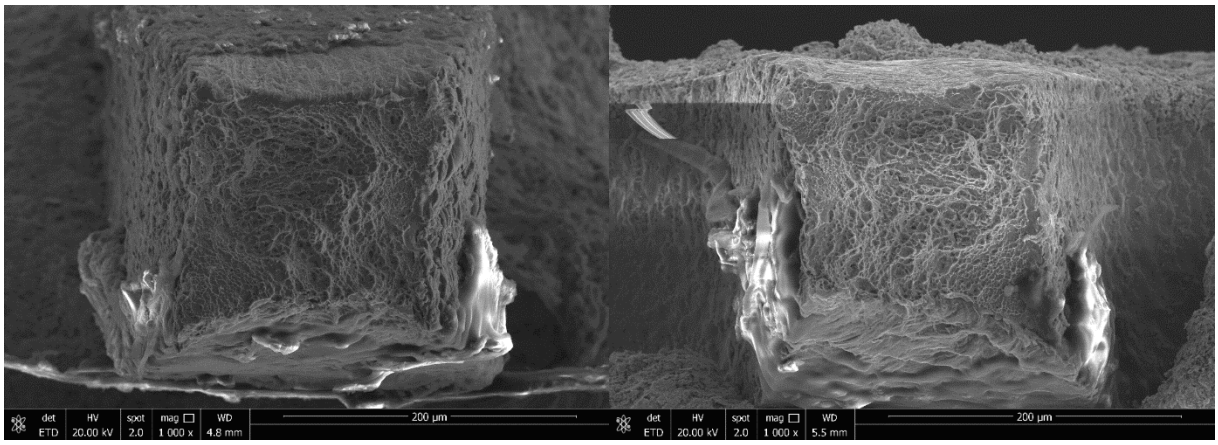

Microsample #4 direction d1 (E = 113.23 GPa | $\sigma_{0.2}$ = 881.25 MPa | UTS = 959.79 MPa | ε_F = 13.56%)

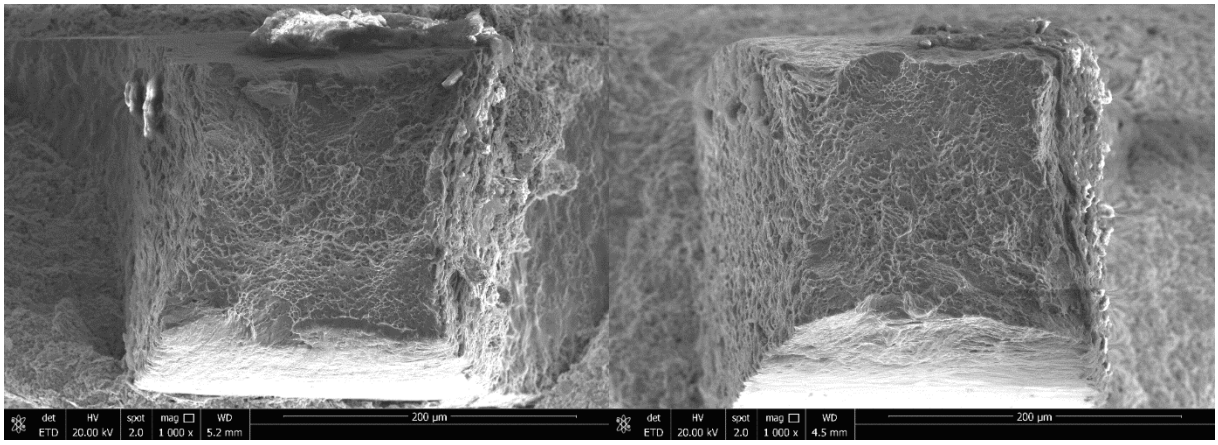

Microsample #5 direction d1 (E = 122.68 GPa | $\sigma_{0.2}$ = 960.00 MPa | UTS = 1084.17 MPa | ε_F = 12.64%)

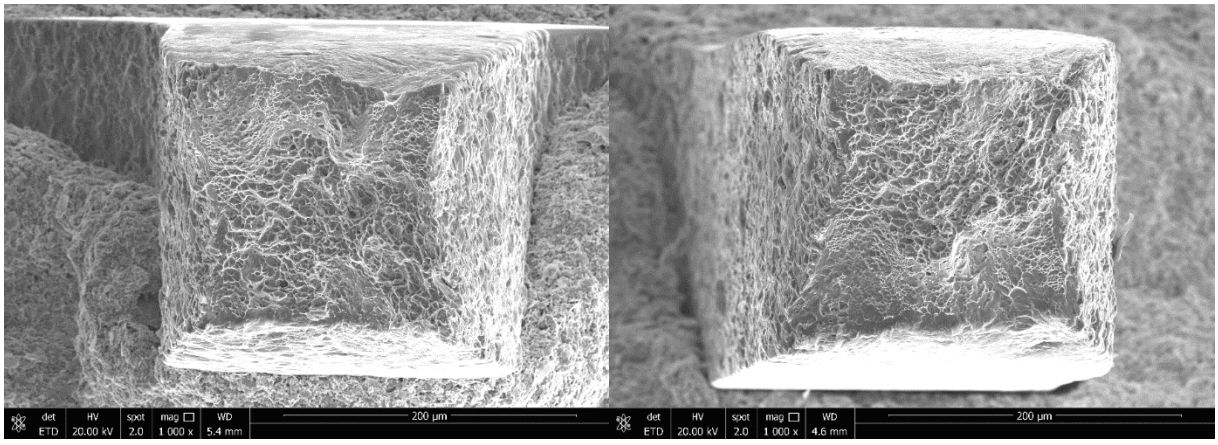

Microsample #6 direction d1 (E = 115.55 GPa | $\sigma_{0.2}$ = 975.00 MPa | UTS = 1067.31 MPa | ε_F = 12.83%)

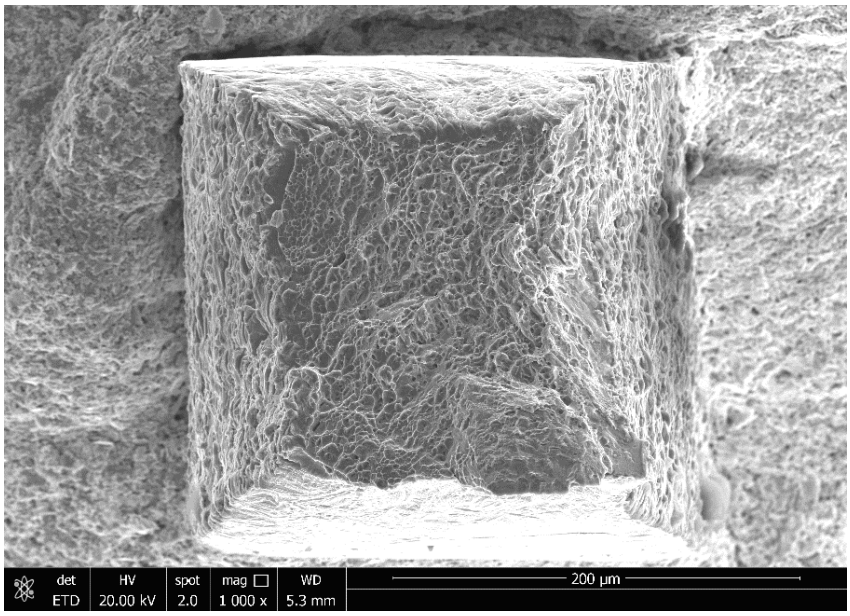

Microsample #7 direction d1 (E = 118.55 GPa | $\sigma_{0.2}$ = 962.50 MPa | UTS = 1048.68 MPa | ε_F = 13.01%)

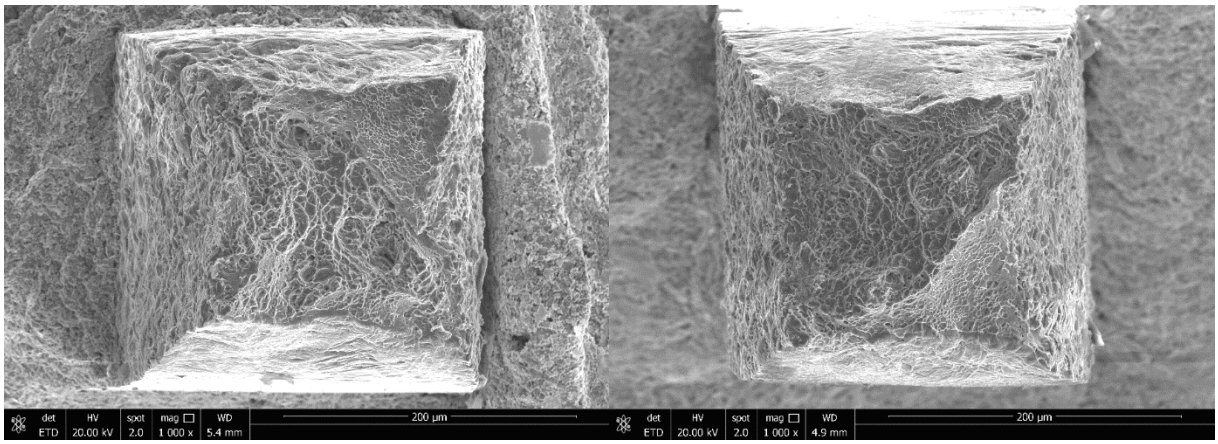

Microsample #8 direction d1 (E = 111.94 GPa | $\sigma_{0.2}$ = 975.50 MPa | UTS = 1023.04 MPa | ε_F = 15.31%)

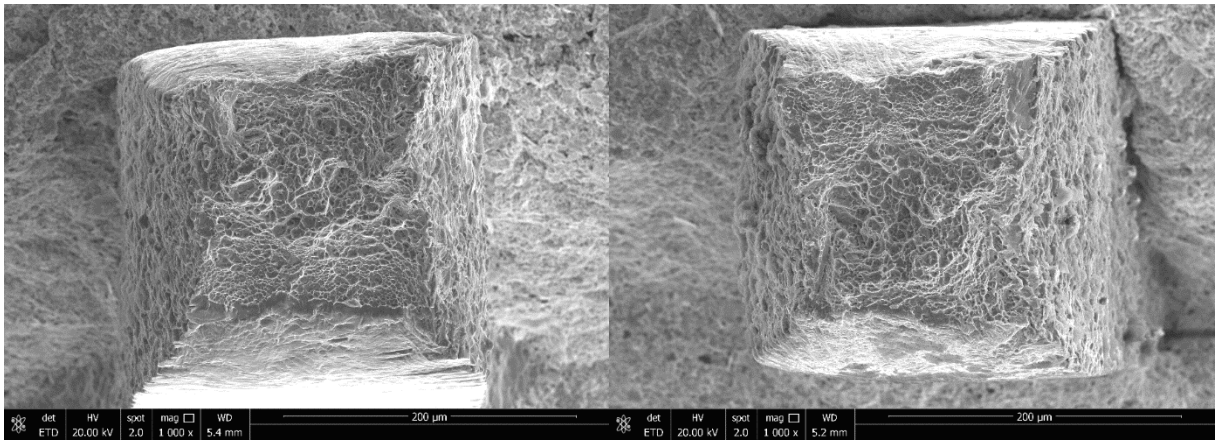

Microsample #9 direction d1 (E = 109.59 GPa | $\sigma_{0.2}$ = 927.50 MPa | UTS = 1011.77 MPa | ε_F = 12.17%)

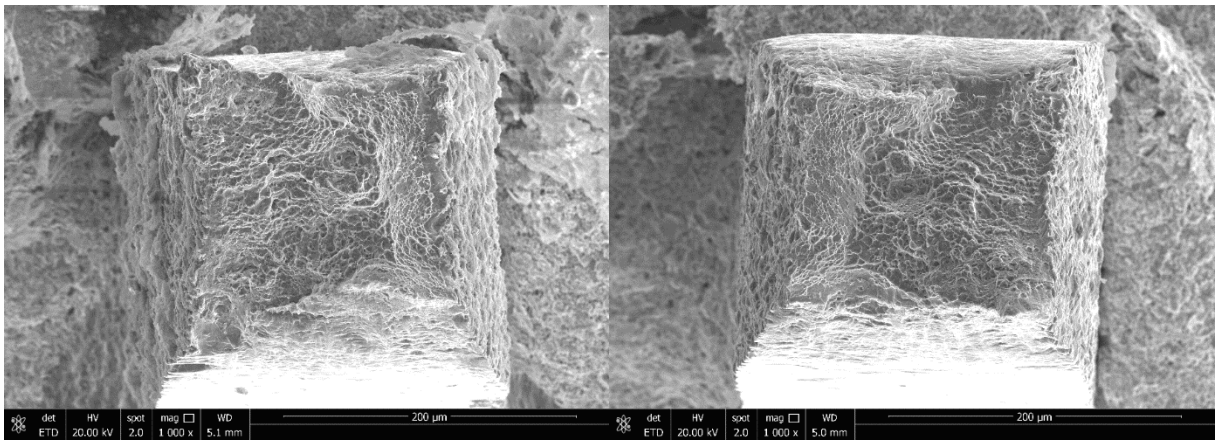

Microsample #10 direction d1 (E = 118.35 GPa | $\sigma_{0.2}$ = 965.00 MPa | UTS = 1041.07 MPa | ε_F = 16.00%)

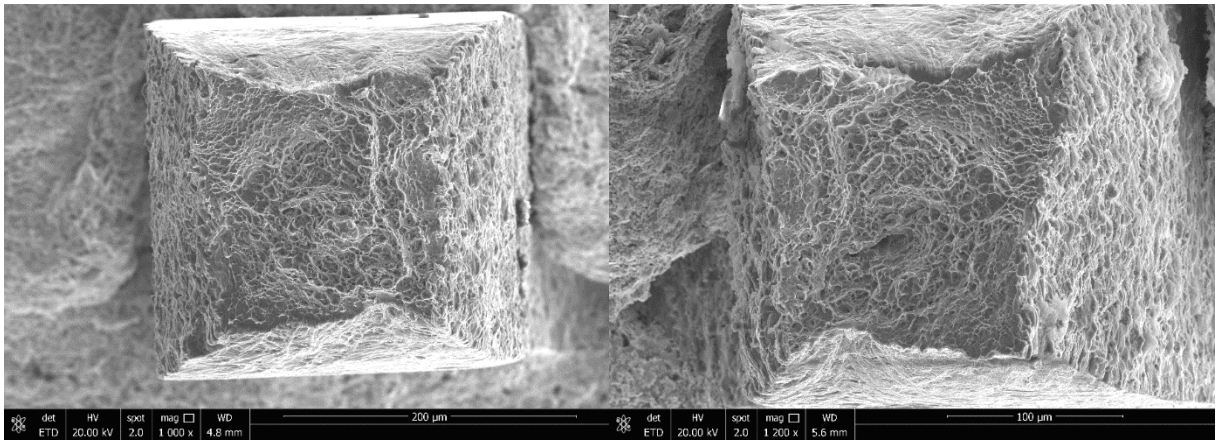

Microsample #11 direction d1 (E = 100.43 GPa | $\sigma_{0.2}$ = 975.00 MPa | UTS = 1021.17 MPa | ε_F = 14.61%)

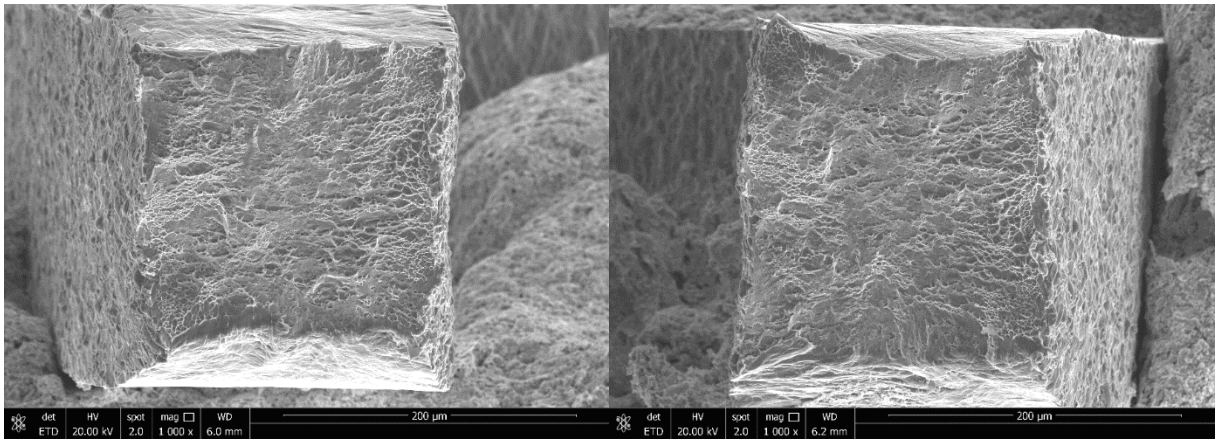

Microsample #1 direction d2 (E = 111.10 GPa | $\sigma_{0.2}$ = 922.50 MPa | UTS = 1049.18.17 MPa | ε_F = 13.18%)

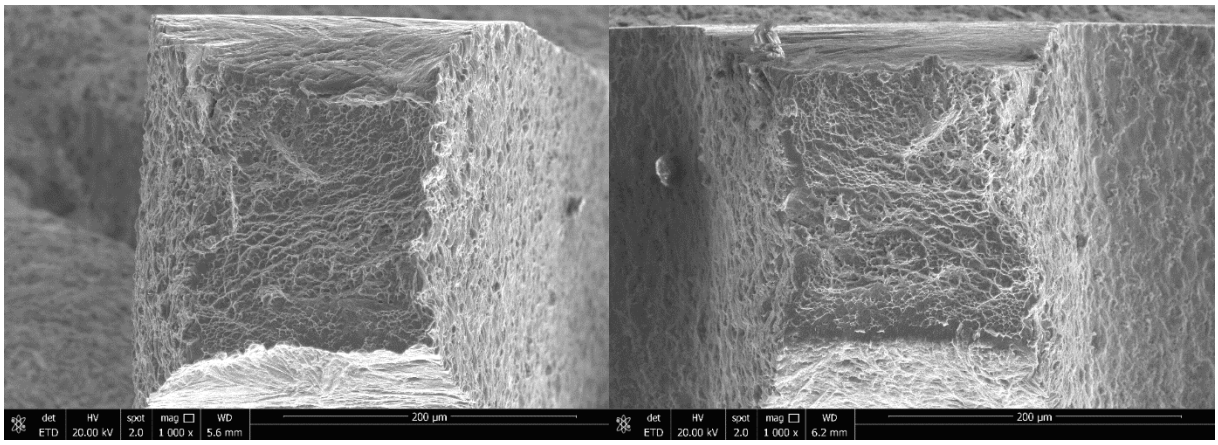

Microsample #2 direction d2 (E = 114.31 GPa | $\sigma_{0.2}$ = 885.00 MPa | UTS = 981.51 MPa | ε_F = 11.63%)

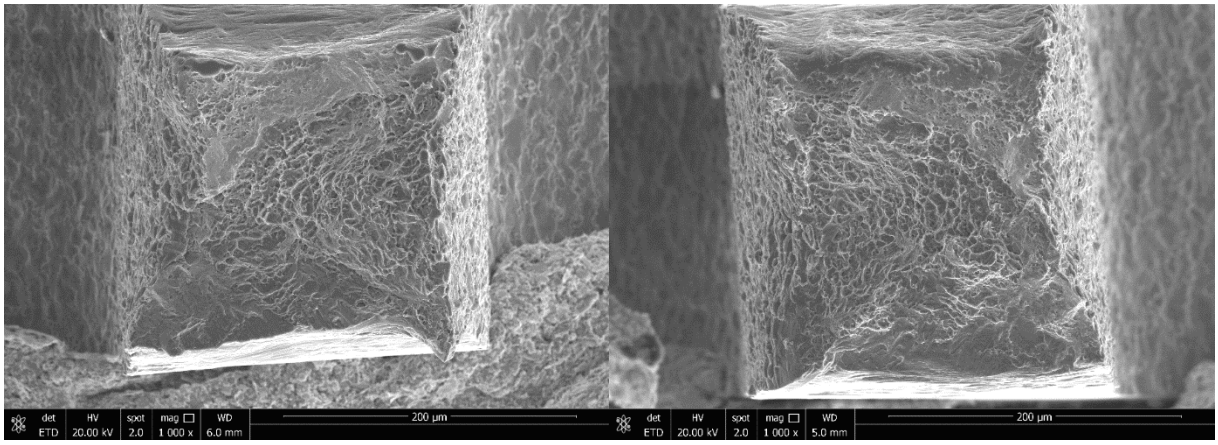

Microsample #3 direction d2 (E = 109.68 GPa | $\sigma_{0.2}$ = 870.00 MPa | UTS = 966.96 MPa | ε_F = 11.44%)

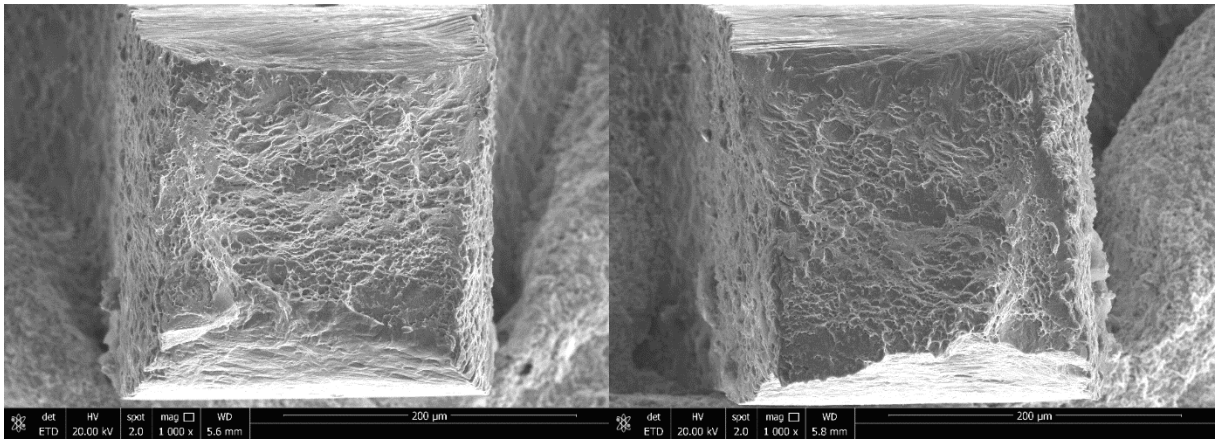

Microsample #4 direction d2 (E = 115.26 GPa | $\sigma_{0.2}$ = 890.00 MPa | UTS = 1013.44 MPa | ε_F = 8.41%)

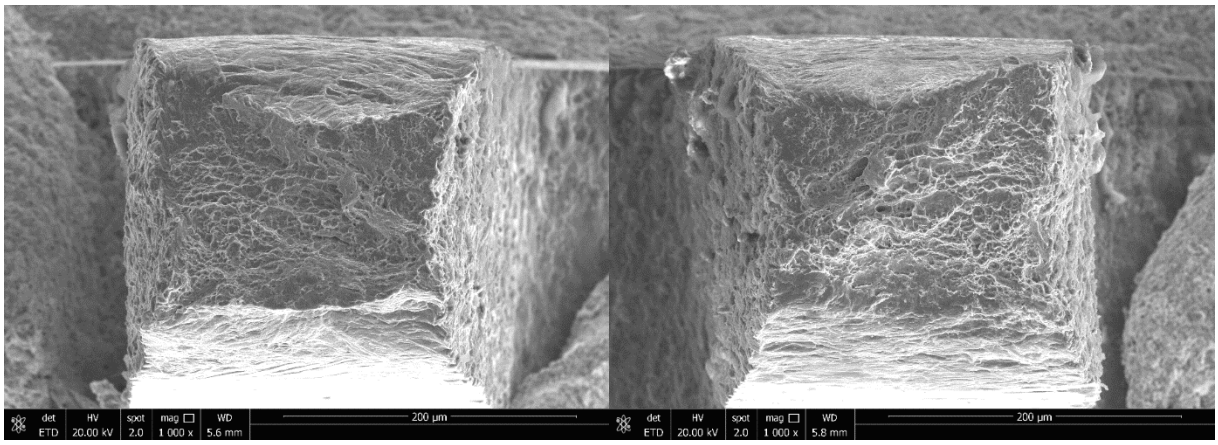

Microsample #5 direction d2 (E = 117.83 GPa | $\sigma_{0.2}$ = 875.00 MPa | UTS = 962.43 MPa | ε_F = 12.37%)

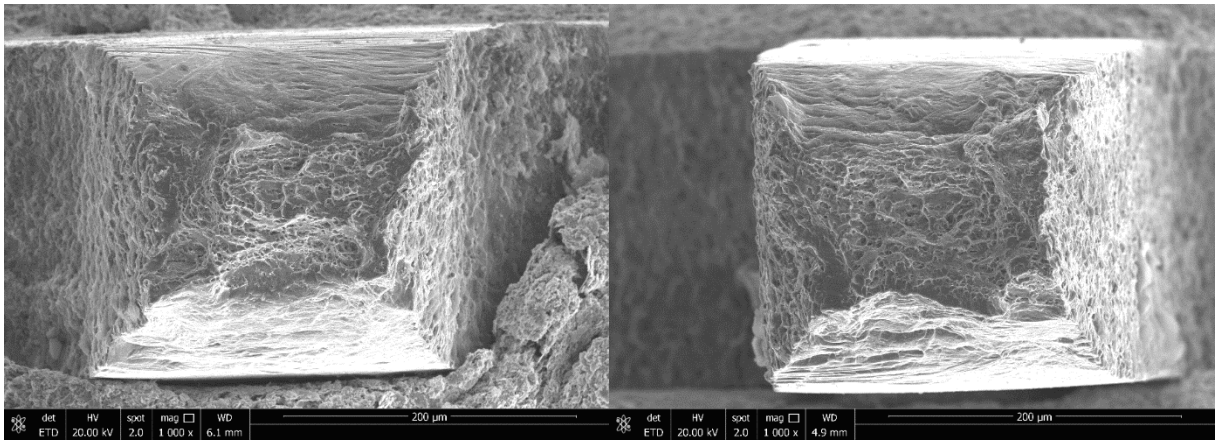

Microsample #6 direction d2 (E = 100.07 GPa | $\sigma_{0.2}$ = 874.50 MPa | UTS = 941.19 MPa | ε_F = 11.51%)

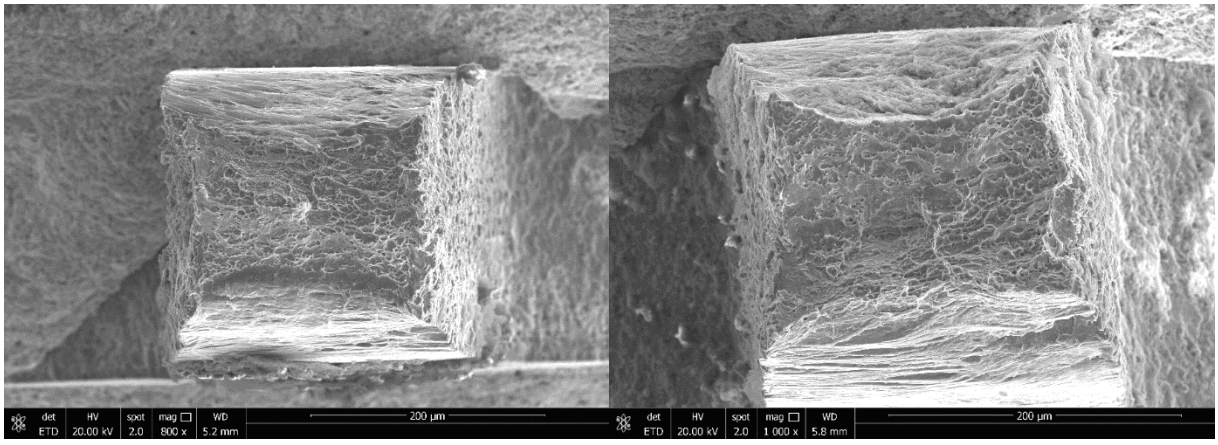

Microsample #7 direction d2 (E = 111.48 GPa | $\sigma_{0.2}$ = 862.50 MPa | UTS = 969.84 MPa | ε_F = 10.40%)

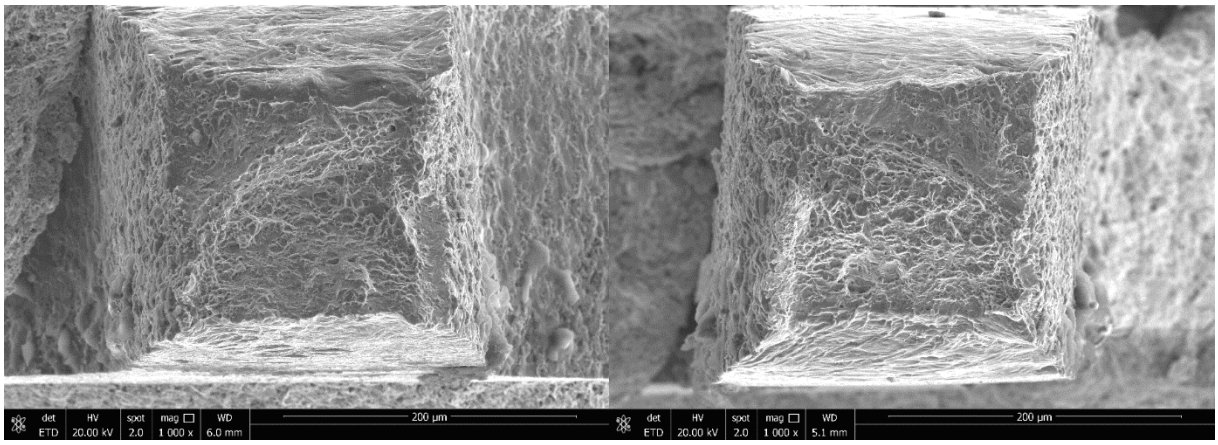

Microsample #8 direction d2 (E = 124.98 GPa | $\sigma_{0.2}$ = 865.00 MPa | UTS = 980.52 MPa | ε_F = 12.64%)

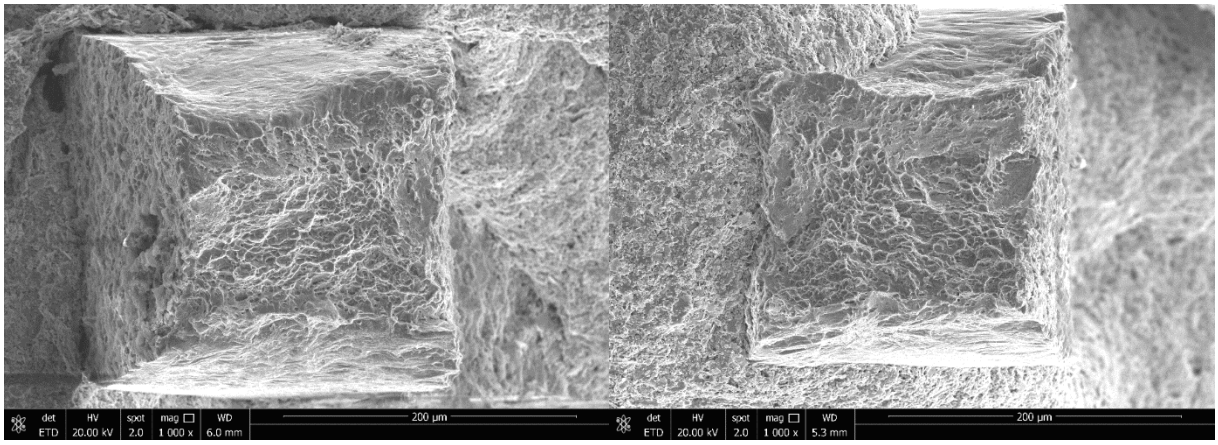

Microsample #9 direction d2 (E = 121.16 GPa | $\sigma_{0.2}$ = 877.50 MPa | UTS = 980.02 MPa | ε_F = 12.59%)

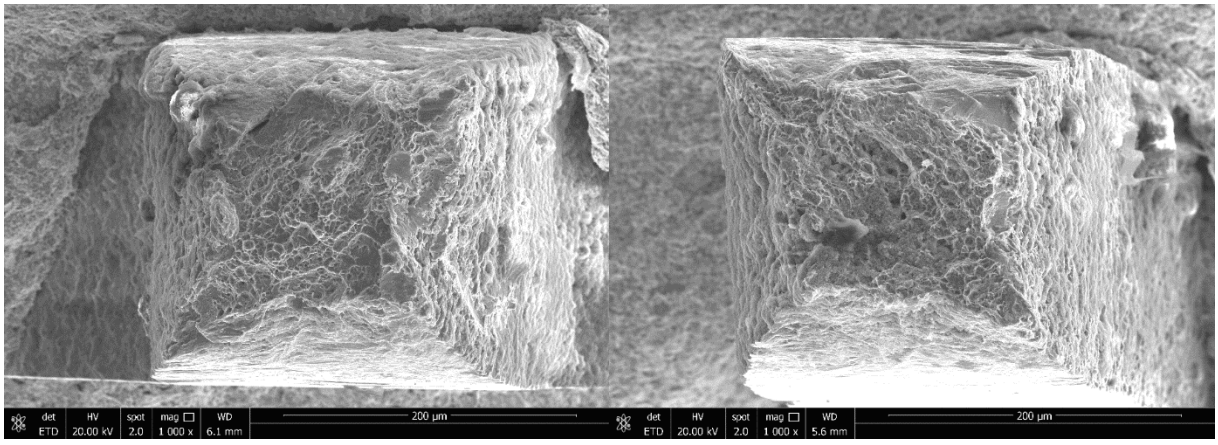

Microsample #10 direction d2 (E = 117.30 GPa | $\sigma_{0.2}$ = 750.00 MPa | UTS = 858.41 MPa | ε_F = 12.26%)

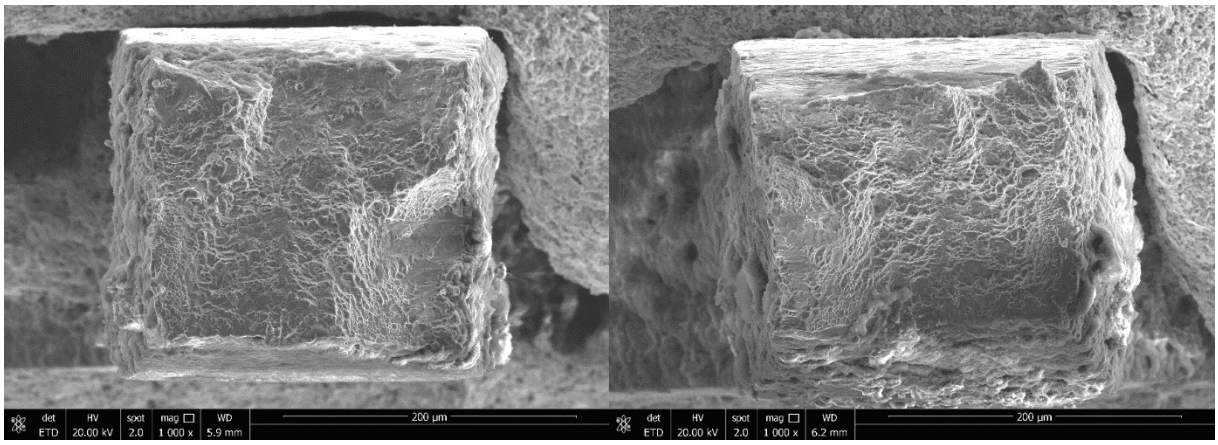

Microsample #11 direction d2 (E = 115.33 GPa | $\sigma_{0.2}$ = 825.00 MPa | UTS = 943.93 MPa | ε_F = 10.93%)

APPENDIX C: Microsample Stress Strain Responses

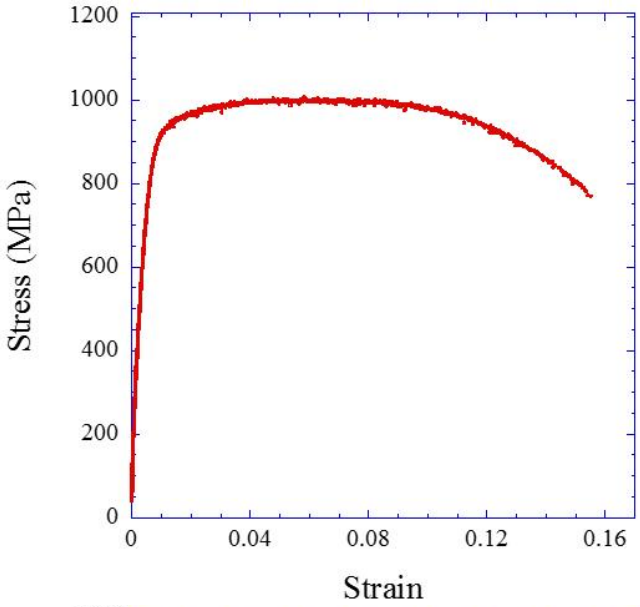

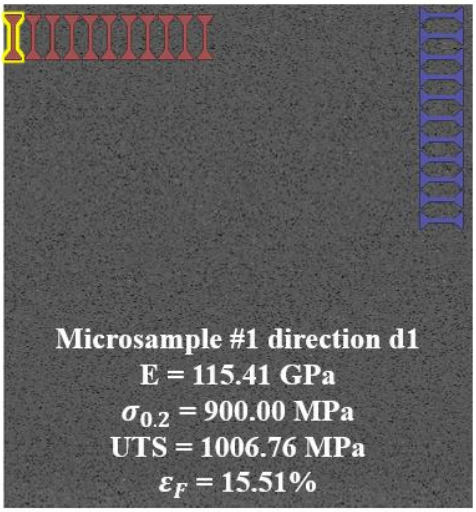

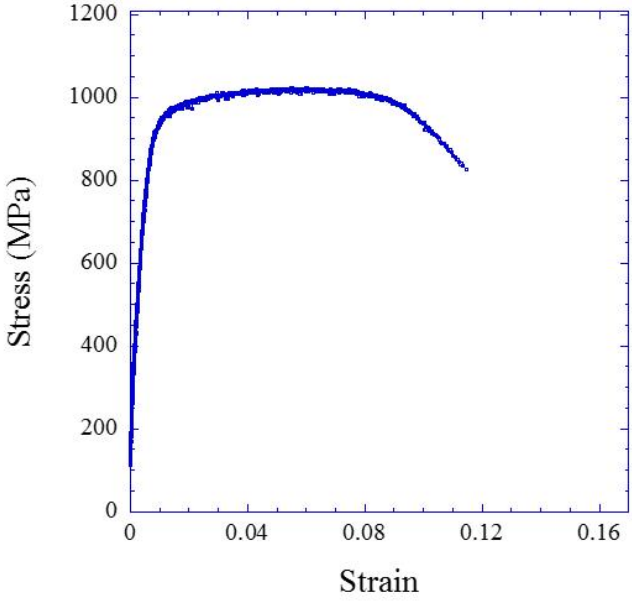

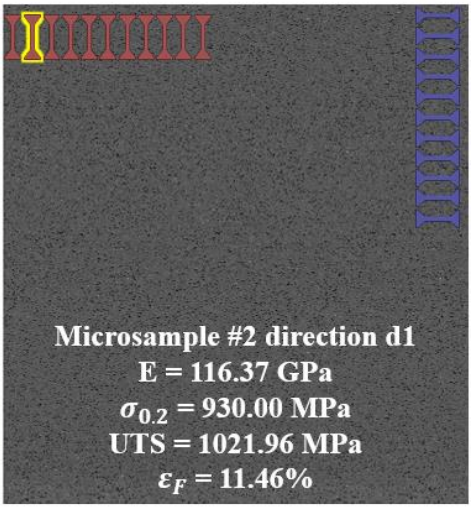

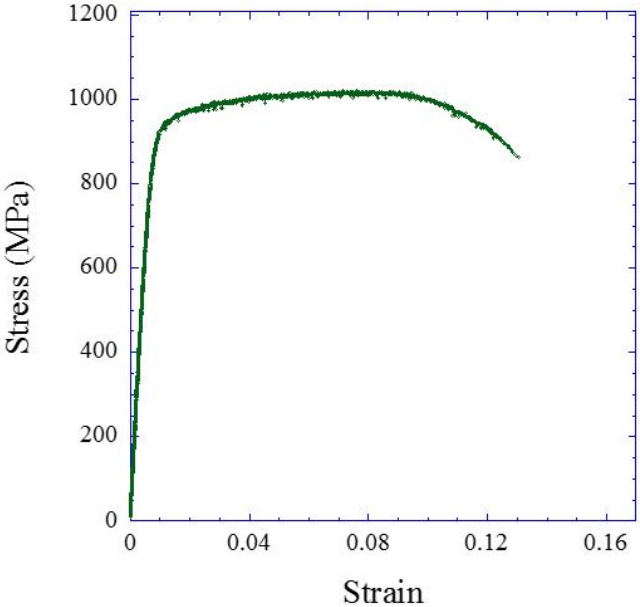

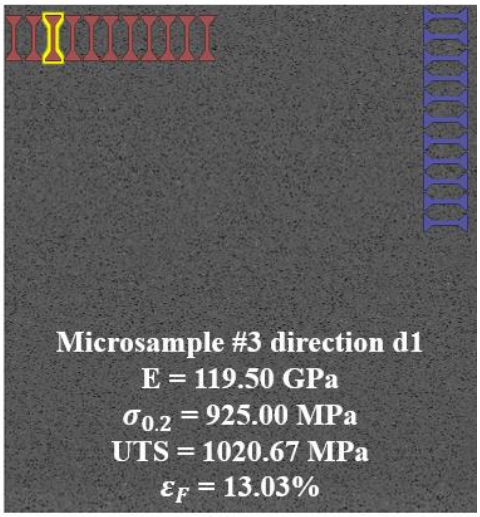

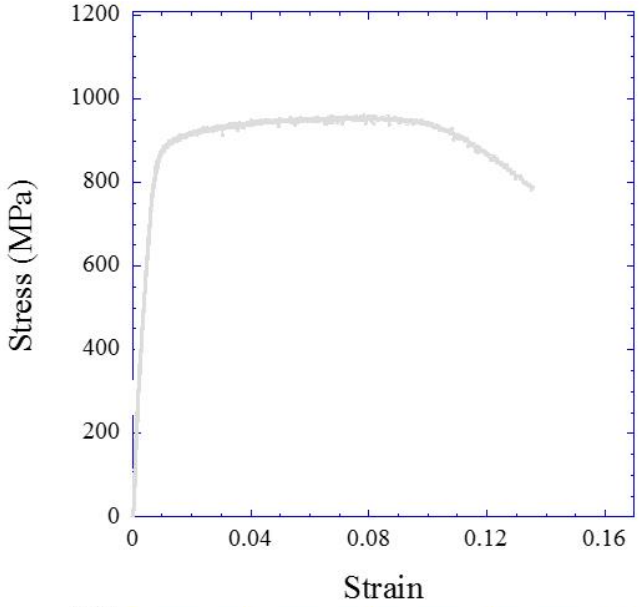
Stress (MPa)
Strain
1200
1000
800
600
400
200
0
0
0.04
0.08
0.12
0.16

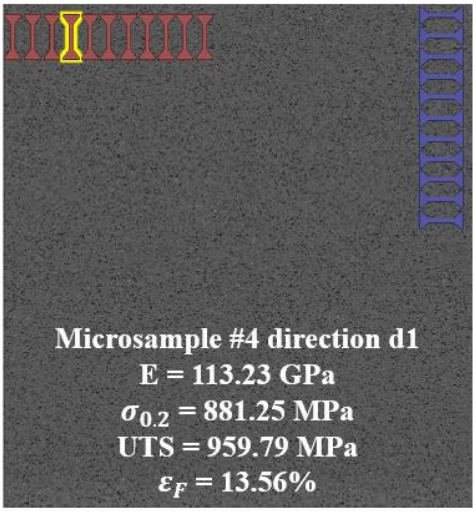
Microsample #4 direction d1
E = 113.23 GPa
$\sigma_{0.2}$ = 881.25 MPa
UTS = 959.79 MPa
ε_F = 13.56%

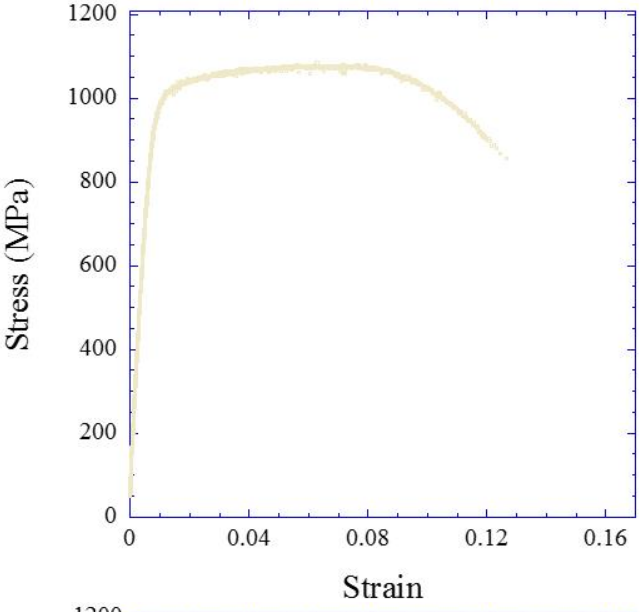
Stress (MPa)
Strain
1200
1000
800
600
400
200
0
0
0.04
0.08
0.12
0.16

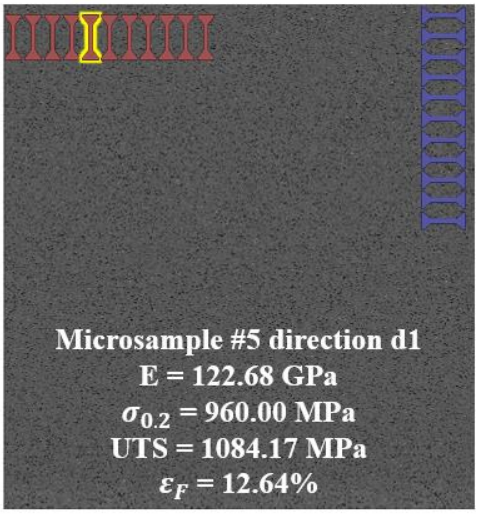
Microsample #5 direction d1
E = 122.68 GPa
$\sigma_{0.2}$ = 960.00 MPa
UTS = 1084.17 MPa
ε_F = 12.64%

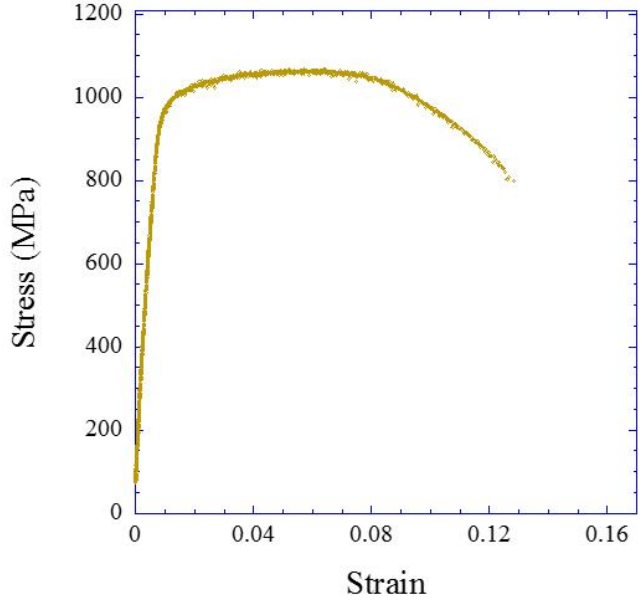
Stress (MPa)
Strain
1200
1000
800
600
400
200
0
0
0.04
0.08
0.12
0.16

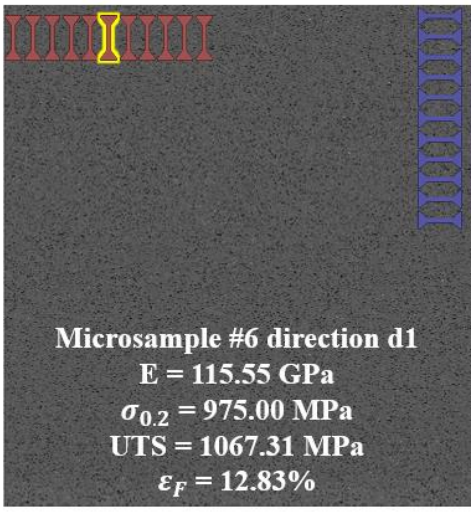
Microsample #6 direction d1
E = 115.55 GPa
$\sigma_{0.2}$ = 975.00 MPa
UTS = 1067.31 MPa
ε_F = 12.83%

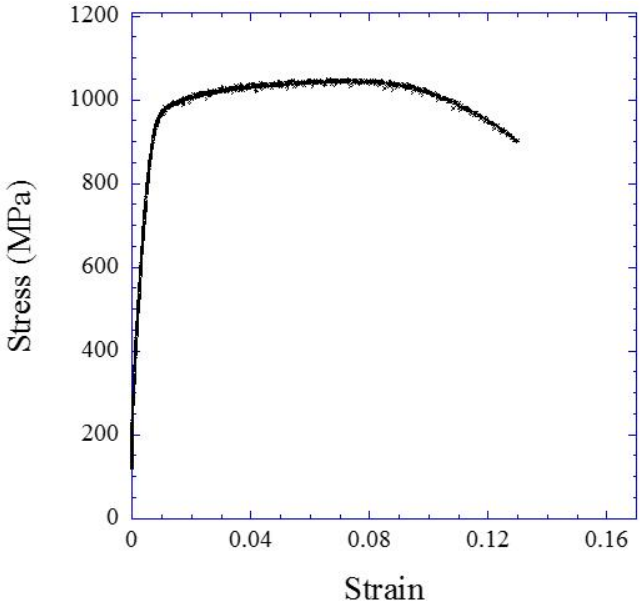
Stress (MPa)
Strain
0
200
400
600
800
1000
1200
0
0.04
0.08
0.12
0.16

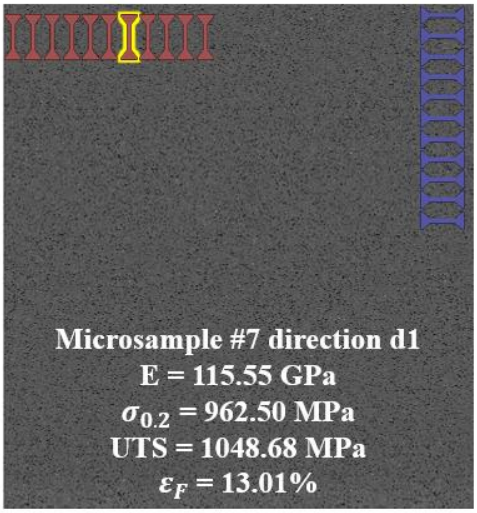
Microsample #7 direction d1
E = 115.55 GPa
$\sigma_{0.2}$ = 962.50 MPa
UTS = 1048.68 MPa
ε_F = 13.01%

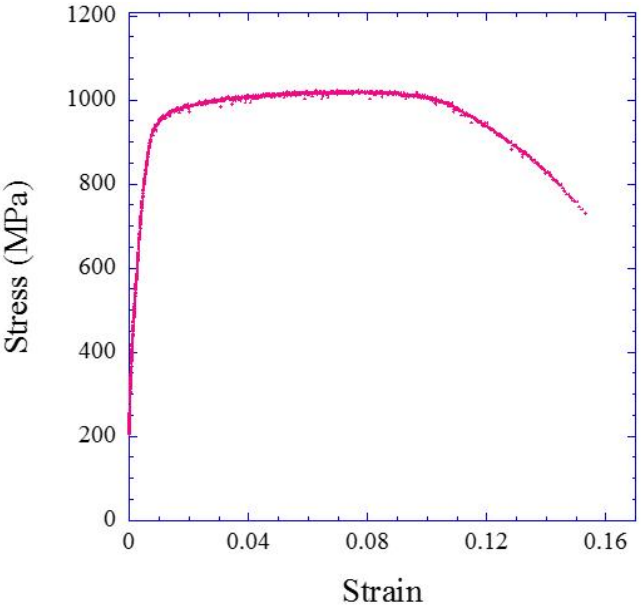
Stress (MPa)
Strain
0
200
400
600
800
1000
1200
0
0.04
0.08
0.12
0.16

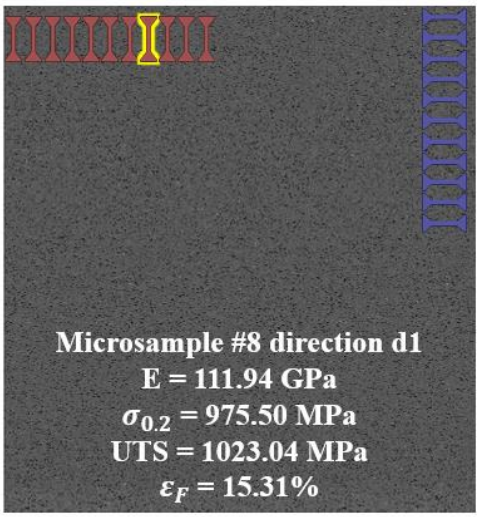
Microsample #8 direction d1
E = 111.94 GPa
$\sigma_{0.2}$ = 975.50 MPa
UTS = 1023.04 MPa
ε_F = 15.31%

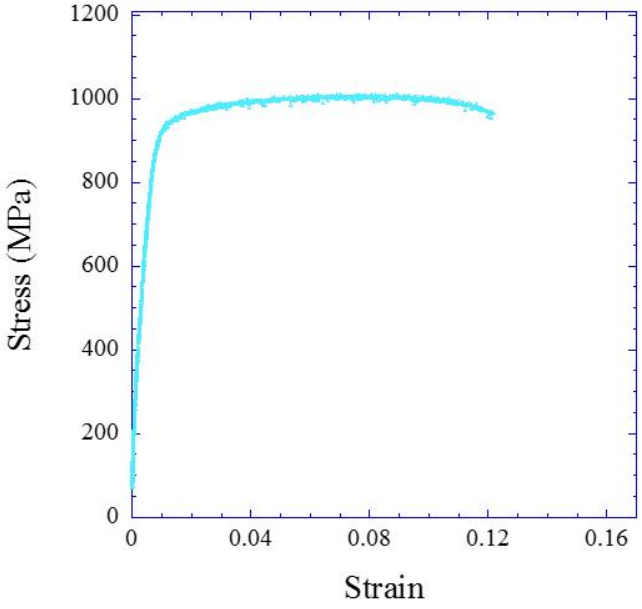
Stress (MPa)
Strain
0
200
400
600
800
1000
1200
0
0.04
0.08
0.12
0.16

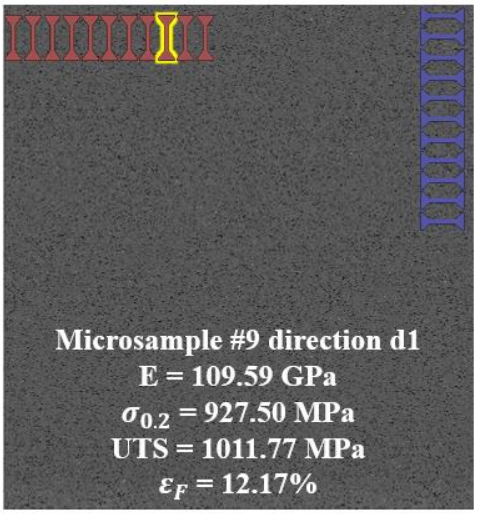
Microsample #9 direction d1
E = 109.59 GPa
$\sigma_{0.2}$ = 927.50 MPa
UTS = 1011.77 MPa
ε_F = 12.17%

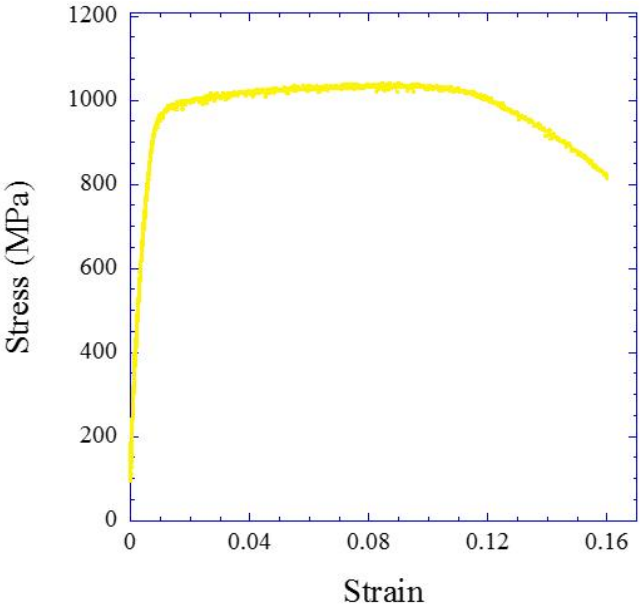
Stress (MPa)
Strain
0
200
400
600
800
1000
1200
0
0.04
0.08
0.12
0.16

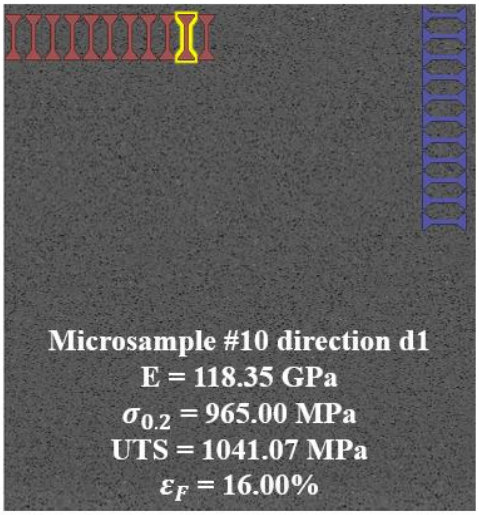
Microsample #10 direction d1
E = 118.35 GPa
$\sigma_{0.2}$ = 965.00 MPa
UTS = 1041.07 MPa
ε_F = 16.00%

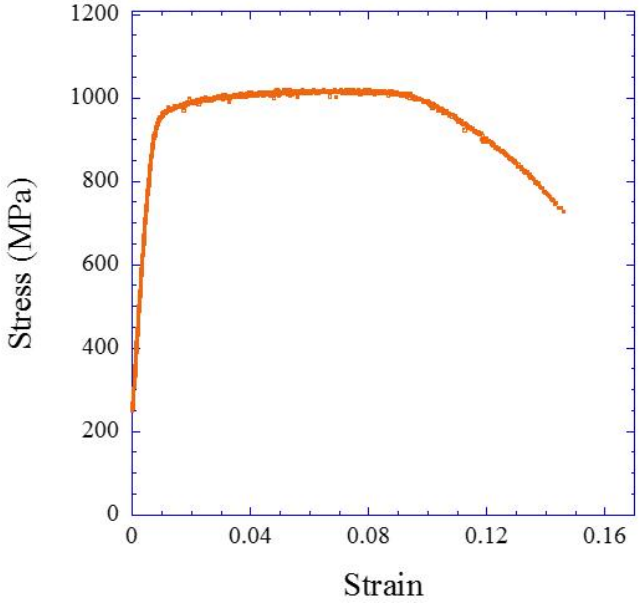
Stress (MPa)
Strain
0
200
400
600
800
1000
1200
0
0.04
0.08
0.12
0.16

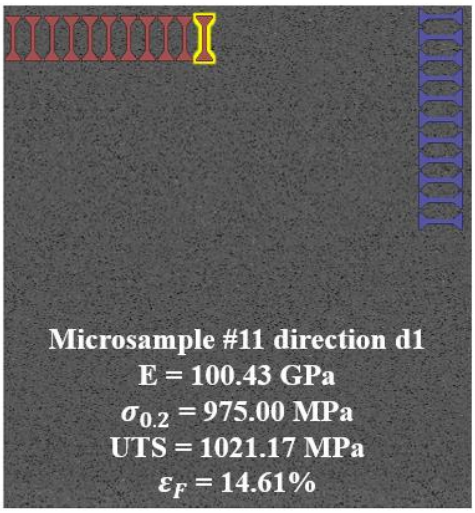
Microsample #11 direction d1
E = 100.43 GPa
$\sigma_{0.2}$ = 975.00 MPa
UTS = 1021.17 MPa
ε_F = 14.61%

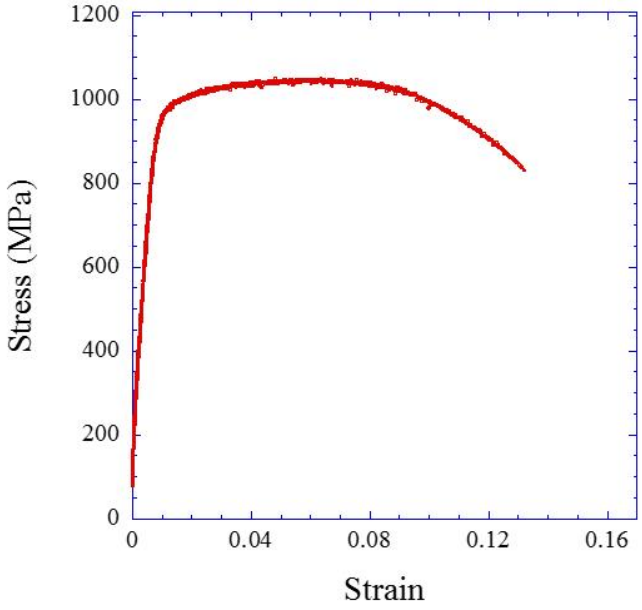
Stress (MPa)
Strain
0
200
400
600
800
1000
1200
0
0.04
0.08
0.12
0.16

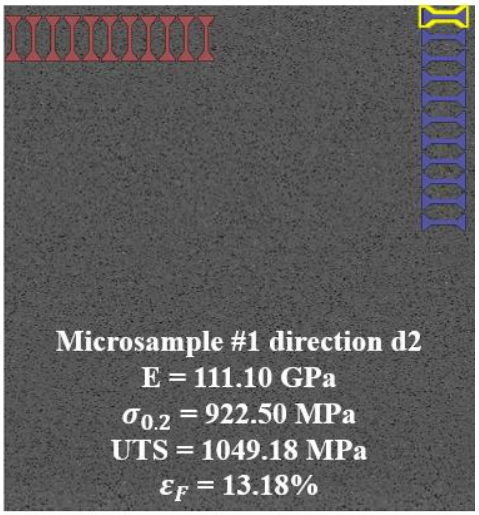
Microsample #1 direction d2
E = 111.10 GPa
$\sigma_{0.2}$ = 922.50 MPa
UTS = 1049.18 MPa
ε_F = 13.18%

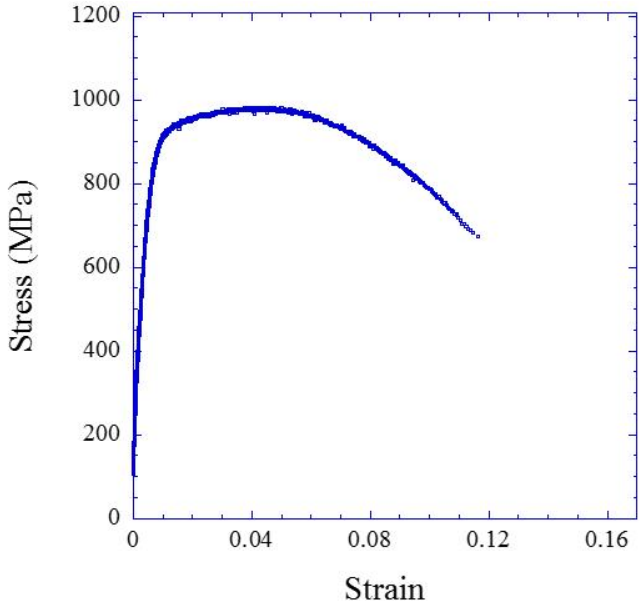
Stress (MPa)
Strain
0
200
400
600
800
1000
1200
0
0.04
0.08
0.12
0.16

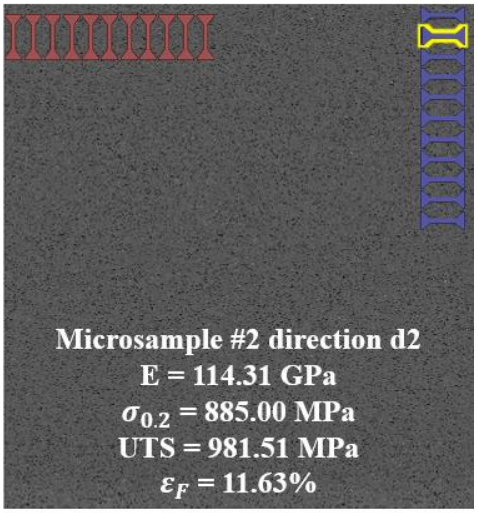
Microsample #2 direction d2
E = 114.31 GPa
$\sigma_{0.2}$ = 885.00 MPa
UTS = 981.51 MPa
ε_F = 11.63%

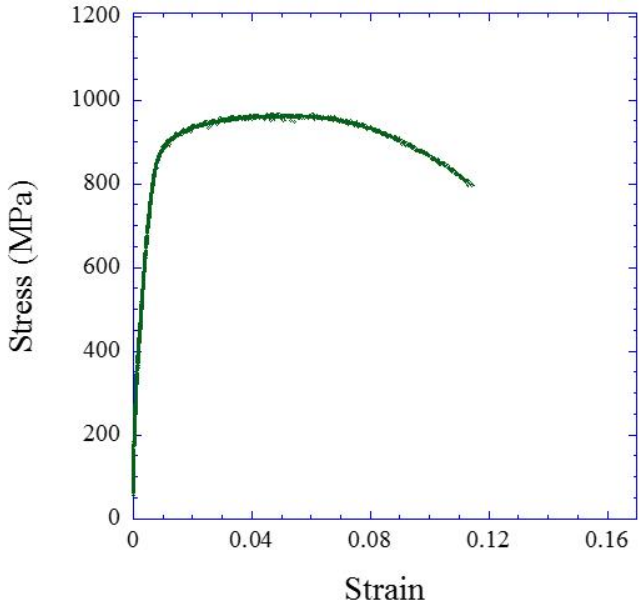
Stress (MPa)
Strain
0
200
400
600
800
1000
1200
0
0.04
0.08
0.12
0.16

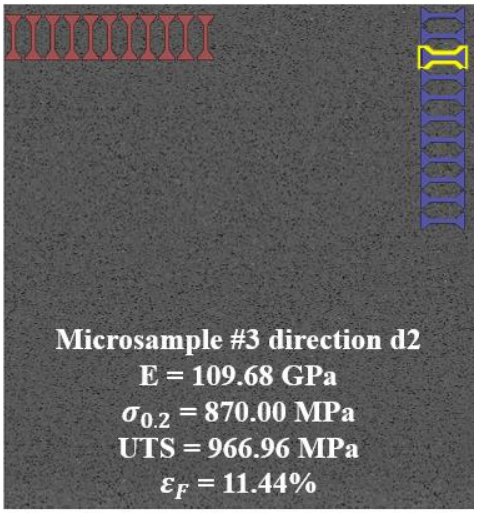
Microsample #3 direction d2
E = 109.68 GPa
$\sigma_{0.2}$ = 870.00 MPa
UTS = 966.96 MPa
ε_F = 11.44%

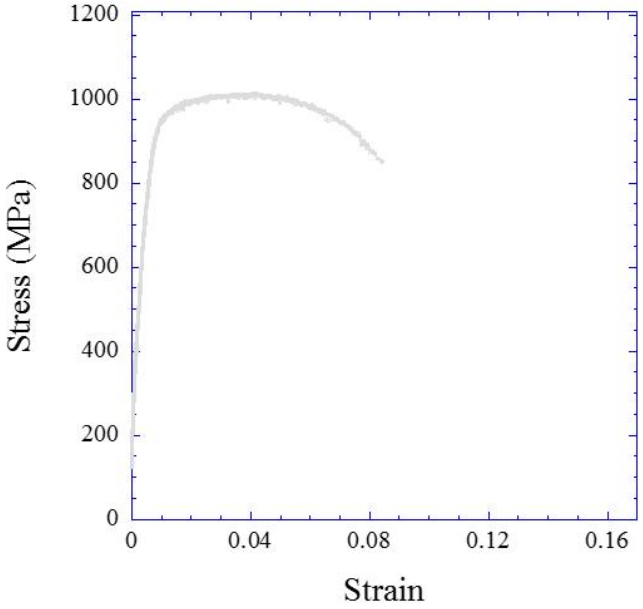
Stress (MPa)
Strain
0
200
400
600
800
1000
1200
0
0.04
0.08
0.12
0.16

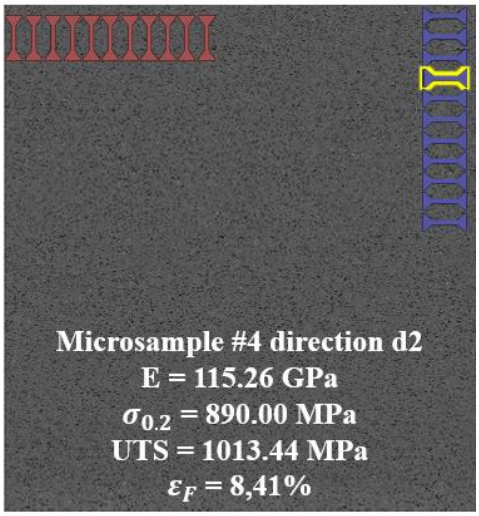
Microsample #4 direction d2
E = 115.26 GPa
$\sigma_{0.2}$ = 890.00 MPa
UTS = 1013.44 MPa
ε_F = 8,41%

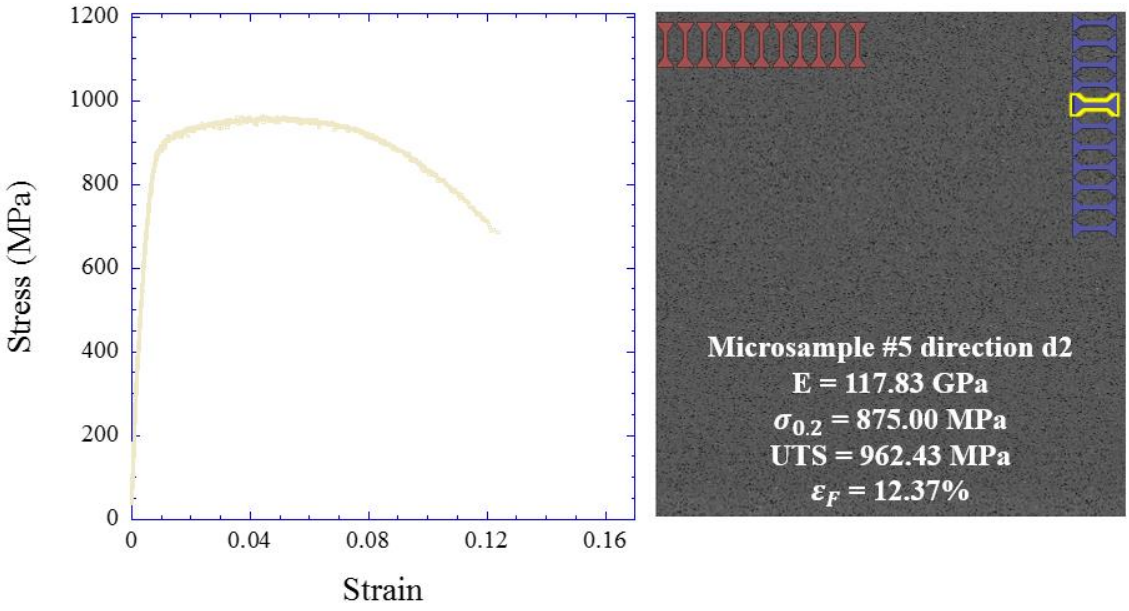
Stress (MPa)
Strain
Microsample #5 direction d2
E = 117.83 GPa
$\sigma_{0.2}$ = 875.00 MPa
UTS = 962.43 MPa
ε_F = 12.37%

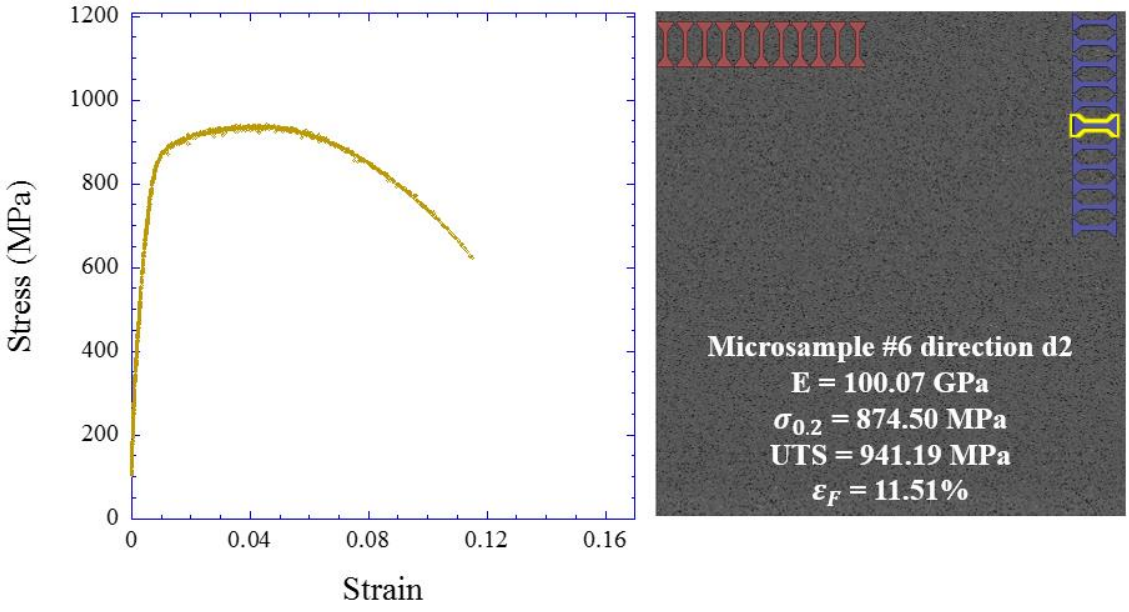
Stress (MPa)
Strain
Microsample #6 direction d2
E = 100.07 GPa
$\sigma_{0.2}$ = 874.50 MPa
UTS = 941.19 MPa
ε_F = 11.51%

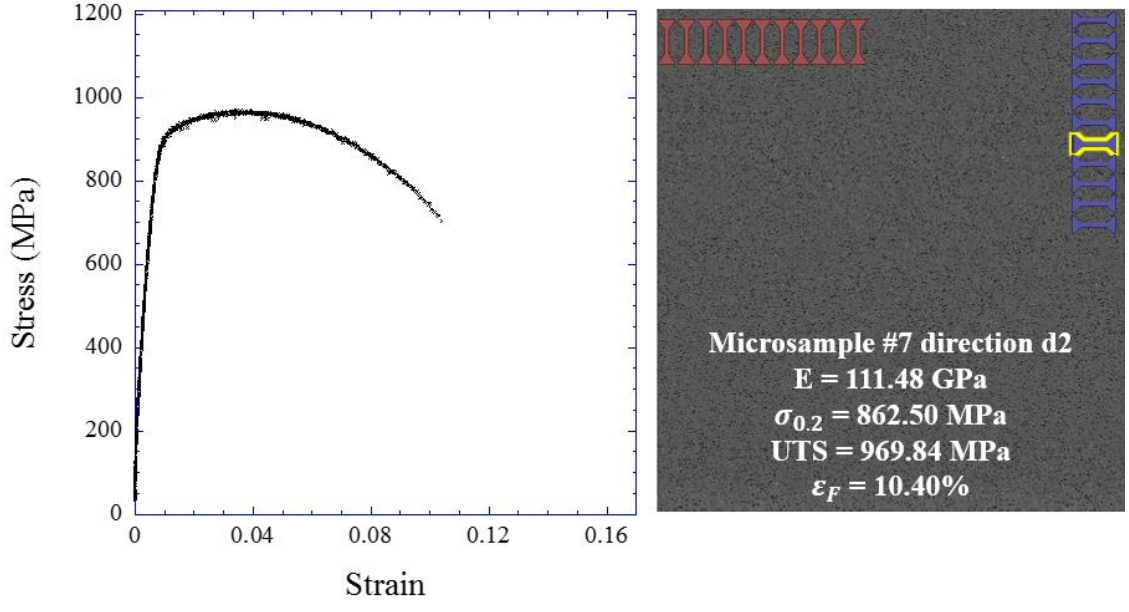
Stress (MPa)
Strain
Microsample #7 direction d2
E = 111.48 GPa
$\sigma_{0.2}$ = 862.50 MPa
UTS = 969.84 MPa
ε_F = 10.40%

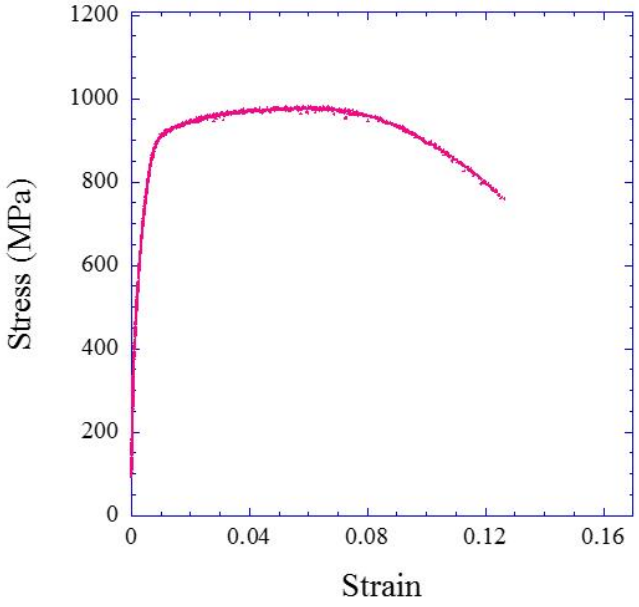
Stress (MPa)
Strain
0
200
400
600
800
1000
1200
0
0.04
0.08
0.12
0.16

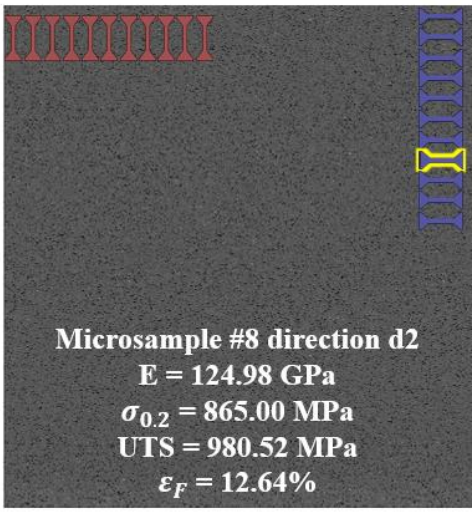
Microsample #8 direction d2
E = 124.98 GPa
$\sigma_{0.2}$ = 865.00 MPa
UTS = 980.52 MPa
ε_F = 12.64%

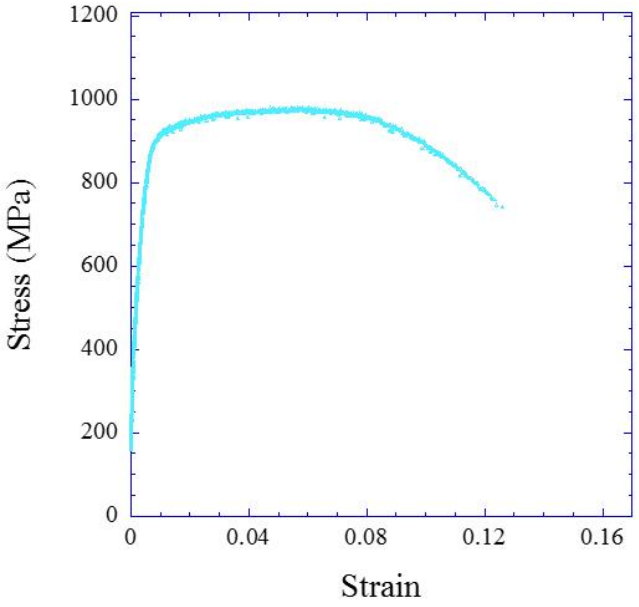
Stress (MPa)
Strain
0
200
400
600
800
1000
1200
0
0.04
0.08
0.12
0.16

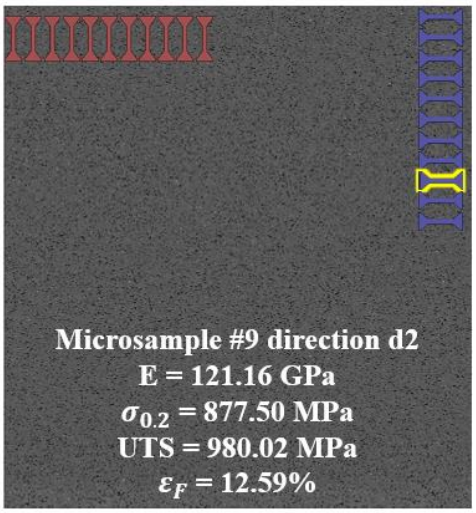
Microsample #9 direction d2
E = 121.16 GPa
$\sigma_{0.2}$ = 877.50 MPa
UTS = 980.02 MPa
ε_F = 12.59%

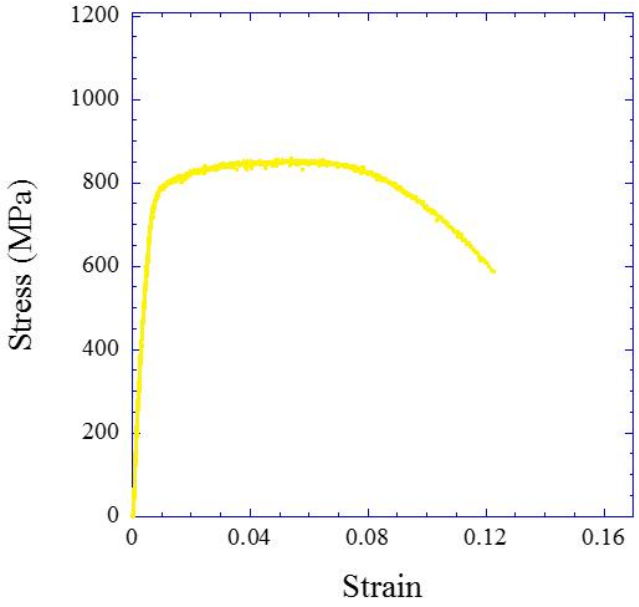
Stress (MPa)
Strain
0
200
400
600
800
1000
1200
0
0.04
0.08
0.12
0.16

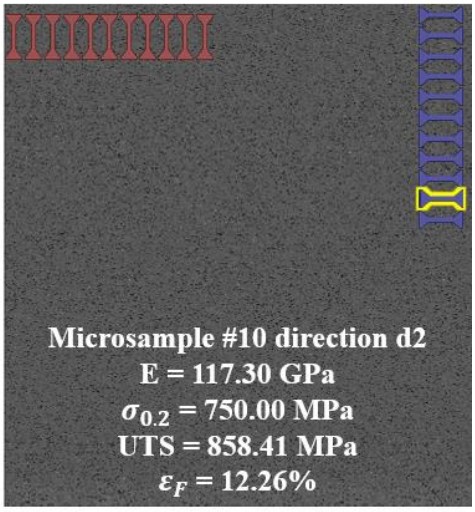
Microsample #10 direction d2
E = 117.30 GPa
$\sigma_{0.2}$ = 750.00 MPa
UTS = 858.41 MPa
ε_F = 12.26%

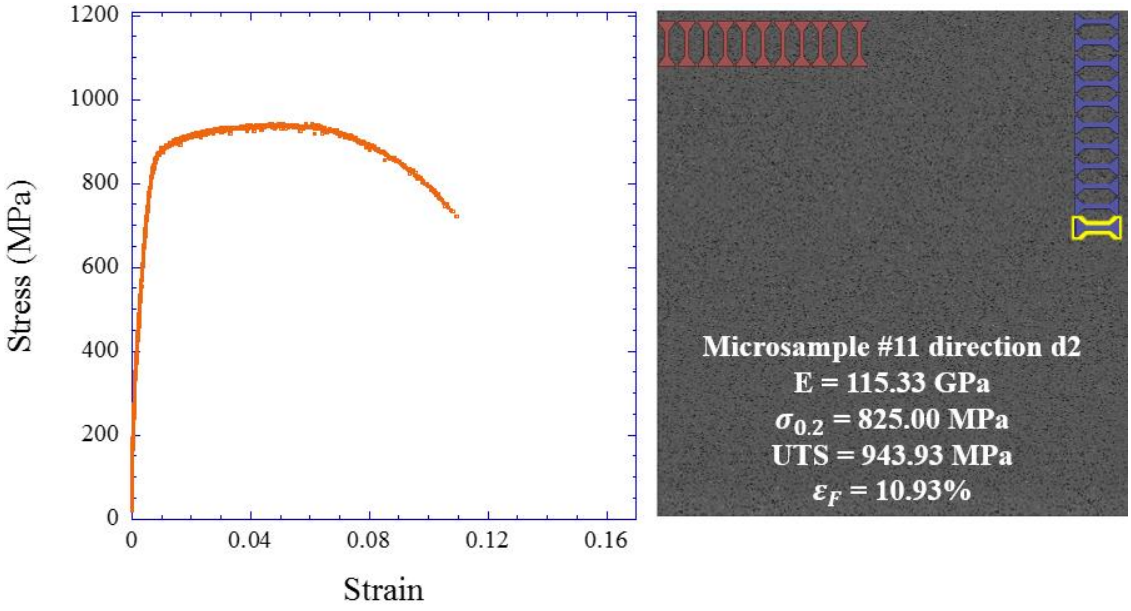
1200
1000
800
600
400
200
0
Stress (MPa)
0
0.04
0.08
0.12
0.16
Strain
Microsample #11 direction d2
E = 115.33 GPa
$\sigma_{0.2}$ = 825.00 MPa
UTS = 943.93 MPa
ε_F = 10.93%